

Resistive Interchange Mode destabilized by Helically Trapped Energetic Ions in Helical Plasma



National University
SOKENDAI
The Graduate University for Advanced Studies



Xiaodi Du

Department of Fusion Science
The Graduate University for Advanced Studies

This dissertation is submitted for the degree of
Doctor of Philosophy

December 2015

I would like to dedicate this thesis to my loving parents, my little daughter Yiling Du and my wife Nan Shi ...

Declaration

I hereby declare that except where specific reference is made to the work of others, the contents of this dissertation are original and have not been submitted in whole or in part for consideration for any other degree or qualification in this, or any other university. This dissertation is my own work and contains nothing which is the outcome of work done in collaboration with others, except as specified in the text and Acknowledgments. This dissertation contains fewer than 65,000 words including appendices, bibliography, footnotes, tables and equations and has fewer than 150 figures.

Xiaodi Du
December 2015

Acknowledgements

I'm indebted to a great number of people for the help, advice and support in these five years. First of all, I thank my supervisor Dr. S. Ohdachi for teaching me how to build the Soft X-ray system and how to analyse the MHD fluctuation data, filling numerous gaps in my knowledge, encouraging me continuously and warmly, tolerating my various shortcomings and providing strong support throughout my five year Ph.D course.

I also thank Dr. Y. Suzuki, who is my vice supervisor. He always give me very valuable suggestions and comments on my research work and always stands beside me to support. My appreciation also extends to Dr. M. Osakabe for the very valuable suggestions on the measurement of the plasma potential by using heavy ion beam probe in the EIC experiment. He also generously provides the NPA data to me, which is critical to understand the resonance condition of the mode. The comments from him to my publications and thesis are also quite helpful.

I also would like to thank Dr. K.Y. Watanabe to teach me a lot in the MHD seminar every week and also for his support on the numerical simulation on the eigenfunction of resistive interchange mode, which is critical to overcome the comments from the PRL referees. He also carefully read my manuscript before the submission and help us improve it through many detail discussions.

Dr. T. Ido is thanked for his strong support for the plasma potential measurement during my experiment. He also kindly provides the old data beyond my experiment and these data significantly improve our understandings on the impacts of the instability.

I also thank Dr. M. Yokoyama for teaching me the neoclassical theory to discuss plasma rotation in non-antisymmetry toroidal plasma and also for the valuable discussions on the plasma rotation induced by EIC generated radial electric field.

I would like to express my gratitude to Dr. K. Tanaka for the fruitful discussions on the turbulence behavior during the EIC burst based on delicate density fluctuation measured by his 2D-PCI system.

I also thank the Dr. M. Yoshinuma for providing the data measured by charge-exchanged recombination spectroscopy and also Dr. K. Ida for the stimulating discussion for physics explanation.

Thanks goes to Prof. Morita to provide the financial support from A3 project. He also kindly invites me to his house every year for the spring party and make my life in Japan so enjoyable.

I express my gratitude to Dr. K. Ogawa for acting beyond the call of duty to answer my questions with clarity and to help me in daily life and for the great friendship founded in these five years. As well as M. Nakamura, Bando, Ono, Asai, Erhui Wang, Tingfeng Ming, Haishan Zhou, Hao Wang, Chunfeng Dong, Hongming Zhang, Xiang Ji, Yue Xu, Hailin Bi, Haiying Fu, Shaofei Geng and Shuyu Dai in NIFS, for various help in my research life.

I express my great gratitude to my parents. Without the support and education from them, none of the achievements can be made. I am deeply indebted to my wife Nan Shi and my daughter Yiling Du. That is the sacrifice that you made to help fulfill my wishes for my doctor degree.

My most sincere gratitude and appreciation is to Prof. Kazuo TOI, who is the reason why I stay in Japan for five years. He brings me to Japan, imparts rudimentary plasma knowledge to me and initiates my research life in the fusion science community. He always acts like my farther and takes care of me very carefully. He does not only guide my research from a global insight, but also answers my every stupid question patiently. He does not only teach me the plasma knowledge, but also teaches me how to be a really excellent experimental scientist and moreover how to be a good man. The life together with Toi-sensei is the most invaluable experience in my life and it will be the most cherished memory in the future.

Abstract

The resistive interchange mode (RIC) is destabilized by finite pressure gradient in magnetic hill and it can be excited even below the beta limit predicted by the Mercier criterion when the magnetic shear stabilization effect disappears due to the effect of resistivity. In recent year, the RIC has been studied experimentally for H-mode plasmas with steep pressure gradient near the edge in the Large Helical Device (LHD), as the magnetic hill exists in the peripheral region. It is found that the RIC localizes at the mode rational surface, having an even function (Gaussian type) with fairly narrow width, consistent with the prediction from a linear resistive MHD theory. Furthermore, a recent numerical study on solving an eigenvalue problem of the RIC has unveiled the existence of an island type eigenmode having a comparable linear growth rate with that of the largest-growth-rate eigenmode (i.e., the usual Gaussian-type interchange eigenmode). The nonlinear saturation level of the RIC may increase with the plasma beta value (=plasma pressure/toroidal magnetic pressure) and decrease with the magnetic Reynolds number, as similar to the tendency of the linear growth rate. Actually, experimental results in LHD support the above predictions.

In this thesis, we report the first observation of a bursting RIC destabilized by resonant interaction with helically trapped energetic ions (EPs) in LHD. Recently, a bursting mode has been observed in the low frequency range with rapid frequency chirping-down where hydrogen neutral beam injection nearly perpendicular to magnetic field line (PERP-NBI) is applied. Although the mode has $m = 1/n = 1$, where m and n are poloidal and toroidal mode numbers respectively, the mode localizes at the mode rational surface in the peripheral region of current-free plasma. In the peripheral region of the LHD plasma, the helical field ripple is large. Consequently, energetic ions generated by PERP-NBI are deeply trapped in the helical ripple, called 'helically trapped energetic ions'. The resistive interchange modes are destabilized through resonant interaction with a characteristic motion of helically trapped energetic ions. The initial frequency of the mode is consistently explained by the mode-particle resonance condition in a non-axisymmetric LHD plasma. This resonant interaction is clearly found in the rapid changes in the energy spectra of charge exchanged neutral flux below the injected beam energy $\sim 34\text{keV}$ measured by the CNPA. The mode structures derived from the ECE data show that the EIC has a quite similar eigenfunction of the radial

displacement of the RIC. That is, the EIC is well localized at the mode rational surface in the latter half of the frequency chirping phase of the EIC burst. Moreover, the eigenfunction of the EIC is an odd function around the rational surface, which indicates an island-type shape, evolving from the Gaussian-shape of the usual RIC and having a localized character of the interchange mode. The EIC affects the electron temperature gradient of the background plasma noticeably. The eigenfunction is clearly distinguished from the EP-driven internal kink mode in tokamak well known as ‘fishbone’ or EP-driven external kink mode, so called EP-driven wall mode in JT-60U or off-axis fishbone in DIII-D. The threshold of the beta value of helically trapped energetic ions is estimated from the parameter scans of the electron density and of the temperature of bulk plasma, respectively. In a specified shot where the beam beta is increased gradually with slowly decreasing line averaged electron density on a fixed NBI power, the threshold is also investigated. Both studies show the existence of the threshold of helically trapped energetic ions pressure, i.e., the volume-averaged beta $\sim 0.3\%$ and that of local beta of $\sim 0.2\%$ at mode rational surface surface.

The non-ambipolar radial transport of the helically trapped energetic ions is consistently inferred from the large and sudden drop of plasma potential measured by the heavy ion beam probe. Consistently, thus generated radial electric field strongly affects the plasma edge and even more interior region. The large edge radial electric field shear induces a significant sheared flow, which brings about clear suppression of micro-turbulence and transient improvement of bulk plasma confinement. The loss rate of helically trapped EPs induced by the EIC averaged over a whole plasma volume reaches $\sim 30\%$. The strong E_r generation by the EIC is dominantly caused by the losses and the effect of redistribution of the EPs is small. The large losses of the helically trapped EPs by the EIC may also be linked to the existence of wide loss cone region slightly away from the 90 degree pitch angle in the outboard side (larger major radius side) of the LHD plasma.

Table of contents

List of figures	xv
List of tables	xxi
1 General Introduction	1
1.1 Power of Nuclear Fusion	1
1.2 Tokamak	3
1.3 Stellarator and Helical Devices	6
1.4 MHD instabilities driven by trapped Energetic Particles	7
1.4.1 'Fishbone' instability	8
1.4.2 Off-axis 'Fishbone' mode	9
1.4.3 Energy principle including hot component	10
1.5 Resonance Conditions	13
1.5.1 Resonance condition in tokamak	13
1.5.2 Resonance condition in Stellarator and Helical Plasmas	14
2 Experimental Setup	19
2.1 Soft X-ray systems	19
2.1.1 Principle of soft X-ray diagnostic system	19
2.1.2 Development of an array system of soft X-ray detectors with large sensitive area	21
2.1.3 A model to derive mode eigenfunction from soft X-ray system . . .	25
2.2 Short reviews for other main diagnostics employed in the EIC study	28
2.2.1 Neutral particle analyzer (NPA)	28
2.2.2 Charge exchange recombination spectroscopy	30
2.2.3 Heavy ion beam probe	32
2.3 Numerical Analysis methods for analysis of fluctuation signals	34
2.3.1 Fast Fourier Transform	34

2.3.2	Empirical mode decomposition method	36
3	Identification of the EIC in LHD	43
3.1	Destabilization of EIC in LHD experiment	43
3.1.1	The EIC in so-called high T_i discharge	44
3.1.2	Destabilization of the EIC only by PERP-NBI	48
3.2	Trajectories of helically trapped energetic ions in LHD	50
3.3	Resonance Condition	50
3.4	Mode eigenfunctions	52
3.4.1	Simulated mode eigenfunction during the RIC linear growth	52
3.4.2	Mode eigenfunctions of the RIC and EIC in LHD experiment	52
3.5	Threshold of the EIC excitation	58
4	Experimental observations of the EIC impacts	61
4.1	Rapid change of perpendicular energetic neutral flux	61
4.2	Generation of negative radial electric field	63
4.3	Change of plasma flow by the EIC	65
4.4	Suppression of micro-turbulence during the EIC	67
5	Models to explain the EIC impacts	69
5.1	Estimation of helically trapped ion loss induced by the EIC	69
5.1.1	Loss/redistribution estimation from the potential reduction	69
5.1.2	Estimation from the diamagnetic loop	71
5.2	A model to explain toroidal rotation change	72
5.2.1	Calculated ΔV_ζ based on the neoclassical theory	72
5.2.2	Calculated ΔV_ζ by taking account of a hyper- μ_\perp profile	74
5.3	Transient improvement of bulk plasma confinement	76
6	Summary and Conclusions	79
	References	81
	My Publications	87
	Appendix A Internal kink mode driven by Trapped Energetic Particles in toka-	
	mak	91
A.1	Energy principle including hot component	92
A.2	Kinetic integral of hot component	93

A.2.1	Drift-kinetic equation	93
A.2.2	Linearizion of drift-kinetic equaiton	95
A.2.3	The approximate solution for the drift-kinetic equation	97
A.2.4	Pressure Perturbation by the trapped fast ions	99
A.2.5	Formulation of energy perturbation by the trapped EPs	103
Appendix B Growth Rate of the fishbone instability in tokamak		107
Appendix C Growth rate of EIC in Large Helical Device		113

List of figures

1.1	Average binding energy per nucleon in unit of MeV against the number of nucleons in nucleus.	1
1.2	The cross section for fusion reactions $D - T$, $D - D$, $D - {}^3H_e$ and so on . . .	2
1.3	Schematic drawing of a tokamak (https://www.euro-fusion.org).	4
1.4	Schematic plot of the particle orbit in tokamak.	5
1.5	Schematic drawing of a helical device (URL: www.nifs.ac.jp).	6
1.6	The time evolution of the soft-x-ray emission along a central chord, the \tilde{B}_θ signal from a coil near the outer wall of the vacuum vessel, and the fast neutron flux. Expansion of the data near two "fishbones" is also shown (McGuire et al., 1983).	8
1.7	Waveforms of (a) EWM and D_α emission, (b) mode frequency with the plasma rotation frequency at $q \approx 2$. (c) Comparison of plasma rotation profiles measured by CXRS with EWM initial frequency. (Matsunaga et al., 2009)	10
1.8	Loss-detector data during a fishbone burst from (a) the BILD foil, (b) the Langmuir probe I_{sat} tip, (c) the FILD scintillator and SSNPA detector, (d) a central BES channel on a discharge without any beam emission, (e) active and passive f-FIDA channels and (f) ICE passband signals that include the fundamental cyclotron resonance (lower band) or the first few harmonics (higher band). The diamonds represent peaks used to measure the phase relative to the Mirnov signal. (Heidbrink et al., 2011)	11
1.9	Radial profiles of the Fourier components of the magnetic field strength in a low β plasma of $R_{ax} = 3.6m$ configuration.	16
2.1	Soft X-ray emission as the function of the electron density and temperature.	21
2.2	Responsibility of AXUV photo-diodes with 100 microns effective S_i thickness (blue curve) and the transmittance coefficient for $15\mu m B_e$ foil filter (red curve).	22

2.3	The circuit of the pre-amplifier of soft X-ray system.	22
2.4	The schematic plot of the layout of soft X-ray system and arrangement of the sightlines.	24
2.5	Layouts of the installed soft X-ray system.	25
2.6	The radial profiles of the measured soft X-ray fluctuation (solid dot) and the best-fitted one simulated from the modeled one (curve) shown in upper figure. The radial profiles of the measured phase differences among different channels of soft X-ray fluctuation (solid dot) and the simulated one from the best-fitting result in lower figure.	26
2.7	The scan of the mode width and mode location to obtain the best-fitted result for the measured soft X-ray emission.	26
2.8	The mode eigenfunction best fitted the measured soft X-ray fluctuation. . .	27
2.9	The schematic plot of the CNPA system in LHD. (Goncharov et al., 2006) .	29
2.10	The arrangements of the SSNPA system in LHD (Isobe et al., 2010).	30
2.11	Schematic views of CXS systems on LHD. (a) Top view of LHD and the toroidal lines of sight. (b) Projected position of the fibers on focal plane for toroidal lines of sight. (Yoshinuma et al., 2010)	31
2.12	The measured charge exchanged spectra at two time slices by the CXS system in LHD.	32
2.13	Beam line of HIBP in LHD. (Ido et al., 2006)	33
2.14	The phase difference between the magnetic probes indicates the $n = 1$ mode is destabilized and the layout of the magnetic probes in LHD is also shown.	37
2.15	Cross Coherence frequency spectrum between the toroidal Mirnov probes is shown. The $m=2/n=1$, $m=1/n=1$, $m=2/n=3$ and $m=2$ or $3/n=4$ are destabilized.	38
2.16	The process of the sifting. (Huang and Wu, 2008)	39
2.17	The flow chart of the sifting process.	39
2.18	One example for the EMD method on the electron temperature fluctuation \tilde{T}_e induced by resistive interchange mode by ECE.	41
2.19	Upper: the radial profile of electron temperature fluctuation \tilde{T}_e derived by the EMD method. Lower: the radial profile of electron temperature fluctuation \tilde{T}_e calculated by the conditioning average.	42
2.20	Left: the radial profile of electron temperature fluctuation \tilde{T}_e derived by FFT method. Right: the radial profile of phase difference of \tilde{T}_e between each ECE channel derived by FFT method.	42
3.1	Arrangements of tangential and perpendicular NBI beamlines and main plasma diagnostics employed in EIC studies.	45

- 3.2 (a) Temporal evolutions of magnetic fluctuations measured by a magnetic probe signal (\dot{b}_θ) and absorbed powers of TANG-NBI ($P_{NBI,\parallel}$) and PERP-NBI ($P_{NBI,\perp}$). (b) Temporal evolutions of the central electron temperature (T_{e0}), central ion temperature (T_{C6+0}), line-averaged electron density ($\langle n_e \rangle$) and volume-averaged bulk plasma beta (β_{dia}) derived from Thomson scattering diagnostics (β_{bulk}) and volume-averaged beam beta perpendicular to magnetic field line ($\beta_{h\perp}$) derived from a diamagnetic loop as $\beta_{h\perp} = \beta_{dia} - \beta_{bulk}$ 46
- 3.3 (a) Time evolution of the magnetic probe signal (\dot{b}_θ) and the temporal frequency (f) calculated by each half period of EIC (solid circle) and full period (line) for a typical EIC. (b) Magnetic probe signal (\dot{b}_θ) with three EICs and the Doppler frequencies evaluated from poloidal (squares) and toroidal (circles) rotation velocities measured by CXRS at $\iota = 1$ location. 47
- 3.4 (a) An expanded view of magnetic probe signal (\dot{b}_θ) and its frequency . (b) Time evolutions of \dot{b}_θ and volume-averaged bulk plasma beta (β_{bulk}) derived from Thomson scattering diagnostics and volume-averaged beam beta perpendicular to magnetic field line ($\beta_{h\perp}$) derived from a diamagnetic loop as β_{dia} , (c) electron temperature at the plasma center (T_{e0}) and that at $\iota = 1$ surface ($T_{e,rs}$) measured by Thomson scattering diagnostics together with the line-averaged electron density $\langle n_e \rangle$, and (d) absorbed power of ECH (P_{ECH}) and that of PERP-NBI ($P_{NBI,\perp}$). 49
- 3.5 (a) A bird's-eye view of the LHD plasma with the contour plot of the field strength and the orbit of a helically trapped energetic ion with the energy $E_b \sim 34keV$ and pitch angle $\chi \sim 85^\circ$. (b) Contour of the field strength expanded onto the 2D plane of poloidal and toroidal angle at $\iota = 1$ surface, indicating the EP orbit. The directions of the magnetic field, the EP orbit and EIC propagation are also indicated with the arrows. (c) The poloidal (f_{pol}^{prec}) and toroidal (f_{tor}^{prec}) precession frequencies calculated from the orbit simulations shown in (a) and (b). 51
- 3.6 (a) The radial profile of electron pressure in a typical shot with the EIC in LHD. (b) Mercier index for stability of ideal interchange mode. (c) The eigenfunctions of resistive interchange mode calculated by a linear resistive MHD code for $S = 10^4$, $S = 10^5$, and $S = 10^6$, respectively. The vertical dotted line indicates the $\iota = 1$ surface. 53

3.7	(a) The linear growth rate of the RIC as the function of the plasma β for $S = 10^6$. (b) The linear growth rate of the RIC as the function of magnetic Reynolds number S for $\beta = 1.5\%$	53
3.8	Time evolutions of electron temperature T_e , measured by ECE (solid line) and the slowly evolving equilibrium component $T_{e,eq}$ derived from the EMD method (dashed line). The derived fluctuations of electron temperature \tilde{T}_e , correlated with the magnetic probe signal \dot{b}_θ by the EMD method.	54
3.9	Time evolutions of the magnetic probe signal with one typical EIC \dot{b}_θ (a) and the radial structure of the electron temperature fluctuations \tilde{T}_e in (b). Radial displacements functions derived from conditionally averaged \tilde{T}_e data for each crest (black) and trough (red) of \tilde{T}_e in the phases I (c), II (d) and IV (e), and the error bars are estimated from the standard deviation of \tilde{T}_e . The eigenfunction of RIC calculated by a linear resistive MHD code is overplotted in (c) with solid curves.	56
3.10	Time evolutions of the magnetic probe signal with one typical EIC \dot{b}_θ (a) and the radial structure of the electron temperature fluctuations \tilde{T}_e in (b). Radial displacements functions derived from conditionally averaged \tilde{T}_e data for each crest (black) and trough (red) of \tilde{T}_e in the phases I (c), II (d) and IV (e), and the error bars are estimated from the standard deviation of \tilde{T}_e . The eigenfunction of RIC calculated by a linear resistive MHD code is overplotted in (c) with solid curves.	57
3.11	Time evolutions of the magnetic probe signal with one typical EIC \dot{b}_θ (a) and the radial structure of the electron temperature fluctuations \tilde{T}_e in (b). Radial displacements functions derived from conditionally averaged \tilde{T}_e data for each crest (black) and trough (red) of \tilde{T}_e in the phases I (c), II (d) and IV (e), and the error bars are estimated from the standard deviation of \tilde{T}_e . The eigenfunction of RIC calculated by a linear resistive MHD code is overplotted in (c) with solid curves.	59
3.12	(a) An expanded view of a magnetic probe signal (\dot{b}_θ) is shown. (b) Time evolutions of non-thermal component of volume-averaged plasma beta perpendicular to magnetic field line ($\beta_{h\perp}$) derived by subtracting volume-averaged bulk plasma beta (β_{bulk}) from diamagnetic plasma beta measured by a diamagnetic loop ($\beta_{dia.}$), (c) central electron temperature (T_{e0}), electron density (n_{e0}), line-averaged electron density ($\langle n_e \rangle$) and slowing down time (τ_s) of energetic ions. (d) The deposited density profile from PERP-NBI at $t = 4.04s$ and $t = 4.16s$ by MORH code, respectively.	60

4.1	Temporal evolutions of a magnetic probe signal with two EICs (a) and the charge-exchanged neutral flux at the energy of $20keV$ (b). Time evolution of the energy spectra obtained by the CNPA viewing perpendicular to the plasma (c).	62
4.2	Time evolutions of a magnetic probe signal (\dot{b}_θ) and the absorbed power of PERP-NBI ($P_{NBI\perp}$) (a) and the plasma potential near plasma center of by HIBP (ϕ) and the charge exchanged neutral flux (Γ_0) in the range of $E > 10keV$ measured by a Si-FNPA detector (b). An expanded view of \dot{b}_θ , ϕ and time derivative of ϕ ($d\phi/dt$) for one EIC (c). In (d), the data of potential drop at $r/a \sim 0$ by the EICs is shown as a function of Γ_0	64
4.3	Time evolutions of the magnetic probe signal (a) and the plasma potential obtained by a radial beam scan (r/a) of HIBP (b). Radial profile of the potential change during EIC burst in $R_{ax} = 3.75m$ (circles) in No.109190 and $3.6m$ (triangles) configurations in No.122476 and the fitted profile (black) (c). The radial electric field E_r derived from the fitted $\Delta\phi$ is also indicated with a broken curve.	65
4.4	Time evolution of a magnetic probe signal in the phase in which two EIC bursts appear (a), toroidal rotation velocities of C^{6+} ions at r/a 0.8 (circles), r/a 0.85 (squares) in (b) and those at r/a 0.92 (diamond) and r/a 0.98 (triangular) in (c), respectively. (d) The radial profiles of the measured toroidal rotation at $t = t_1$ (dashed line) and t_2 (solid line), marked in (c) and (d).	66
4.5	Time evolution of a magnetic probe signal in the phase in which two EIC bursts appear (a), toroidal rotation velocities of C^{6+} ions at r/a 0.8 (circles), r/a 0.85 (squares) in (b) and those at r/a 0.92 (diamond) and r/a 0.98 (triangular) in (c), respectively. (d) The radial profiles of the measured toroidal rotation at $t = t_1$ (dashed line) and t_2 (solid line), marked in (c) and (d).	68
5.1	Waveforms of the EIC burst (a) and the observed toroidal flow V_ζ and plasma potential ϕ (b), as a function of the relative time for the EIC onset.	70
5.2	Time evolutions of a magnetic probe signal (\dot{b}_θ) with two EIC bursts and the changes of time derivative of total stored energy measured by a diamagnetic loop (dW_{dia}/dt) corresponding to the two EICs, respectively. The relative time τ_{EIC} is defined at the onset of the EIC	72
5.3	A simulated toroidal rotation change based on neoclassical theory (curve) and the change of C^{6+} ions toroidal rotation velocity measured by CXRS (solid circles) are shown.	74

5.4	Radial profiles of the assumed perpendicular viscosity μ_{\perp} (dotted line), a simulated toroidal rotation change based on neoclassical theory without the radial diffusion term by perpendicular viscosity (dashed line) and a simulated toroidal rotation change with the assumed perpendicular viscosity (solid line). The change of C^{6+} ions toroidal rotation velocity measured by CXRS is shown with circles.	75
5.5	Time evolutions of three EICs in a magnetic probe signal (a), the line integrated electron density ($n_e l$) at plasma peripheral region and the emission of H_{α} light (b) C^{6+} ion temperature ($T_{C^{6+}}$) around mode rational surface and the root mean squared fluctuations of line integrated density fluctuation ($\delta n_{e,rms}$) measured by PCI (c).	76
5.6	The magnetic probe signal with one EIC (a) and the contour plots of the change in $T_{C^{6+}}$ (b) and T_e (c) as a function of the relative time for the onset of an EIC (τ_{EIC}). The uncertainty in the time caused by the time resolution of CXRS system is indicated by an error bar in (b).	77

List of tables

- 1.1 Potential resonance frequency for $m = 1/n = 1$ mode in an LHD plasma . . . 17
- 2.1 Comparison the arrangements of the old and the new soft X-ray detector system 23

Chapter 1

General Introduction

1.1 Power of Nuclear Fusion

The nuclear energy source can be understood from the famous Einstein relation $E = mc^2$. When the nucleus is split into several fragments, the mass of daughter nucleus and parent nucleus are imbalance. The missing mass is well known as mass-defect. According to the Einstein relation, the mass defect equivalent to the excess energy, which is emitted as photons or the kinetic energy of the daughter fragments. In exothermic reactions, the nuclear mass ultimately converts to the thermal energy and can be used to solve the energy crisis for human beings. According to the binding energy curve per nucleon shown in Fig. 1.1, two different patterns of nuclear energy can be categorized:

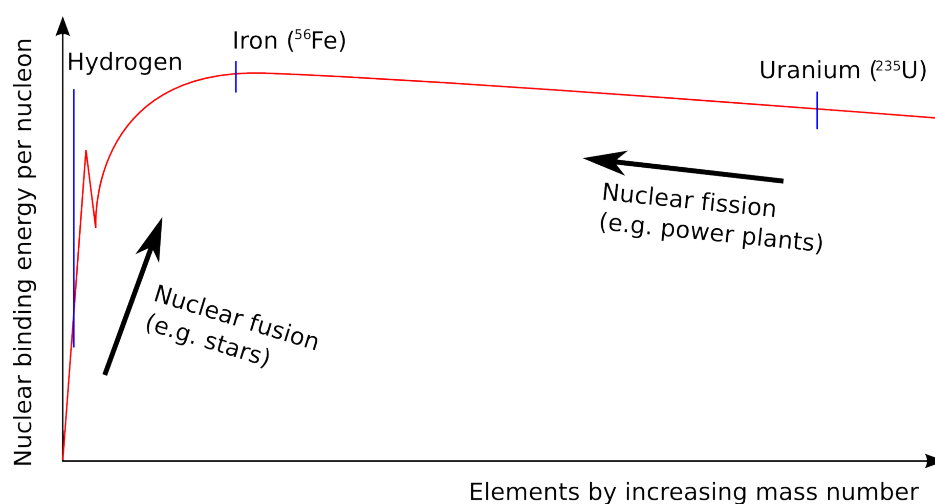


Fig. 1.1 Average binding energy per nucleon in unit of MeV against the number of nucleons in nucleus.

One is the nuclear fission on the right side of ${}^{56}\text{Fe}$, in Fig. 1.1. A nucleus of an atom splits into lighter nucleus and releases the energy. The other is the nuclear fusion on the left hand side of ${}^{56}\text{Fe}$. Several light nucleus can fuse into a single heavier atoms and combined more tightly to release the energy. The nuclear reaction is of greatest relevance to magnetic fusion are listed as follows (Sheffield, 1994),

$$D + T \rightarrow {}^4\text{He}(3.52\text{MeV}) + n(14.0\text{MeV}), \quad (1.1)$$

$$D + D \rightarrow {}^3\text{He}(0.82\text{MeV}) + n(2.45\text{MeV}), \quad (1.2)$$

$$D + D \rightarrow T(1.01\text{MeV}) + p(3.03\text{MeV}), \quad (1.3)$$

$$D + {}^3\text{He} \rightarrow {}^4\text{He}(3.67\text{MeV}) + p(14.67\text{MeV}), \quad (1.4)$$

where the quantities in parentheses are the kinetic energies in the reaction rest frame. These reactions involve the electro-weak interactions and the cross-section for the these fusion reactions are considerably small, shown in Fig 1.2. (Bosch and Hale, 1992). The deuterium-

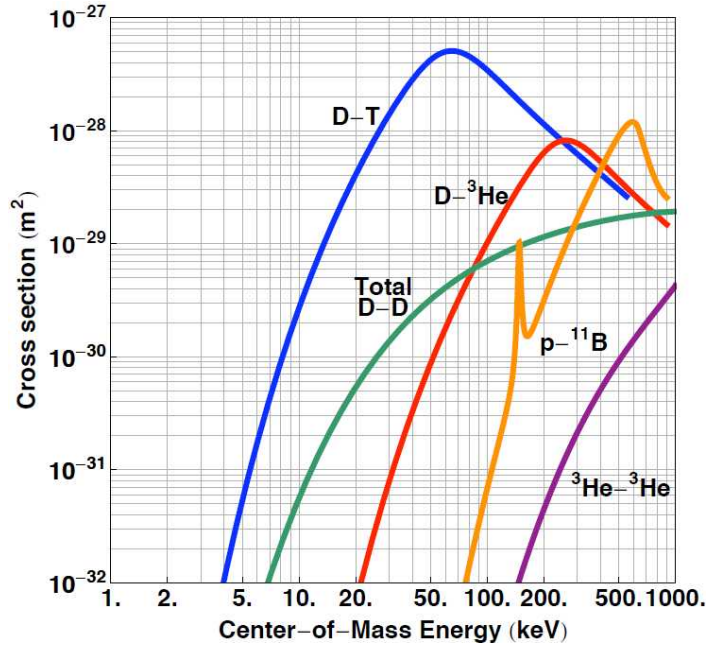
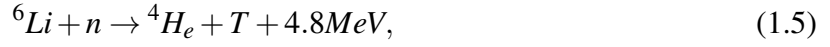


Fig. 1.2 The cross section for fusion reactions $D - T$, $D - D$, $D - {}^3\text{He}$ and so on .

tritium reaction is preferable among all the reactions, because the cross-section is ~ 100 times larger than the deuterium-deuterium and deuterium-helium³ reaction in the lower temperature region. Unfortunately, the tritium has a half life of 12.3 years and in other words, it does not occur in nature. Thus, it is necessary to breed tritium by bombarding lithium with

the fusion neutrons (Sheffield, 1994), as follow.



Lithium can be found in the abundance in the earth's crust. Therefore, it is very attractive to use the $D - T - Li$ fuel cycle for a self-sustaining plasma at the lowest plasma temperature, for example $T > 5\text{keV}$. Deuterium is abundant in nature as $1/6500$ in water. Synchrotron radiation will be more significant in the plasma with very high temperature. Thus to overcome the bremsstrahlung and synchrotron radiation, the temperature have to approach $T > 20\text{keV}$. The requirement of the temperature is derived from the competition between the α heating and losses. As the first step to use the fusion energy on earth, the coming reactor for nuclear fusion should be designed for $D - T$ reaction.

For a deuterium-tritium burning plasma, the charged-particle power per unit volume produced by fusion reaction is given by,

$$p_\alpha = n_D n_T \langle \sigma v \rangle_{DT} E_\alpha \quad (1.7)$$

For the optimum mixture of the deuterium and tritium $n_D = n_T = 1/2 n_i$ (n_i is the ion density), we have

$$p_\alpha = \frac{1}{4} n^2 \langle \sigma v \rangle_{DT} E_\alpha \quad (1.8)$$

1.2 Tokamak

The open magnetic field line device, i.e., magnetic mirror, is a configuration of magnetic field system in which the charged particle will be reflected from the high magnetic field strength to low low magnetic field strength region, depending on the pitch angle of the particle. However, the particle with a very small pitch angle are always not confined, which is said to be in the loss cone. Unfortunately, the particles always try to keep the Maxwellian distribution in velocity space through the collision. Therefore, the open magnetic field line system cannot contain the plasma well enough to realize the fusion reactor. Naturally, the closed field line systems are proposed to replace the magnetic mirror.

The simplest configuration is a torus like a tire, which can be produced by several toroidal coils. However, due to geometry of a simply toroidal magnetic field structure, a pure toroidal

magnetic field is not homogeneous, which can be given by,

$$B_\phi = \frac{B_0}{R}, \quad \nabla B_\phi = -\frac{B_0}{R^2} \vec{e}_R \quad (1.9)$$

where R is the major radius and B_ϕ is the toroidal magnetic field strength. The inhomogeneous magnetic field will produce the drift of the ions and electrons in different direction,

$$\mathbf{v}_{B \times \nabla B} = \frac{1}{\Omega} \frac{\mu}{m} \mathbf{b} \times \nabla B, \quad (1.10)$$

where Ω is the gyro frequency and μ is the magnetic momentum. This will produce the charge separation and develop a vertical electric field and thus $\mathbf{E} \times \mathbf{B}$ drift appears.

$$\mathbf{v}_{E \times B} = \frac{\mathbf{E} \times \mathbf{b}}{B_0} \quad (1.11)$$

For $\mathbf{v}_{E \times B}$ drift, the ion and electron will drift in the same direction, i.e., outward direction and this process is very fast. Therefore, the pure toroidal magnetic field can also not confine the plasma. To overcome such difficulty, the poloidal magnetic field is required to compensate the $\mathbf{v}_{B \times \nabla B}$ drift. The poloidal fields twist the toroidal field line into a helical structure.

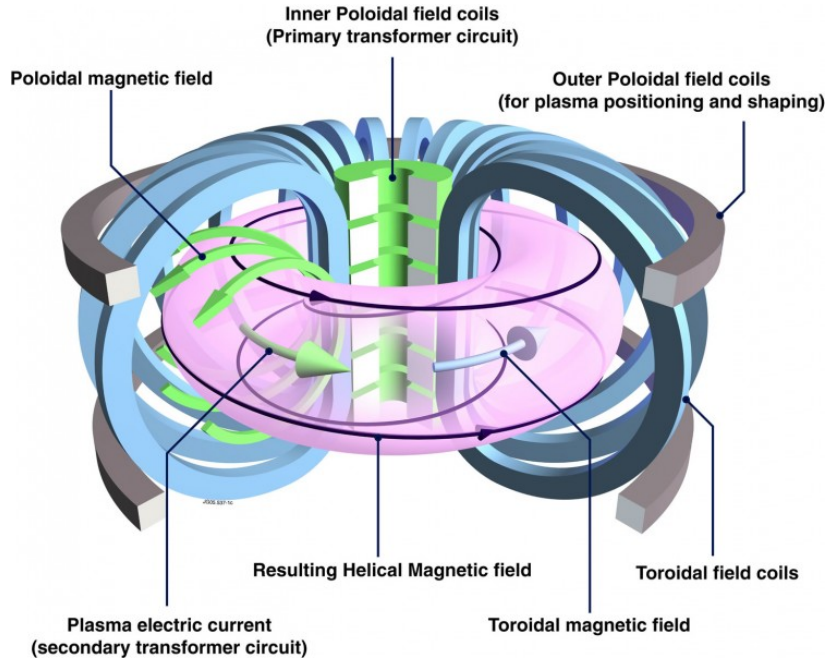


Fig. 1.3 Schematic drawing of a tokamak (<https://www.euro-fusion.org>).

The mechanism of the compensation of the net drift can be depicted in Fig. 1.4. The orbit of the charged particles (electrons and ions) primarily follow the magnetic field line.

After introducing the poloidal magnetic field, in the upper half of the poloidal cross section, the $\mathbf{v}_{\mathbf{B} \times \nabla \mathbf{B}}$ will drift vertically towards the plasma center. In the lower half of the poloidal cross section, the $\mathbf{v}_{\mathbf{B} \times \nabla \mathbf{B}}$ will drift vertically towards the plasma peripheral region. That is, the rotational transform of the magnetic field line can compensate the charge separation due to the inhomogeneity of the toroidal magnetic field. In tokamak, the poloidal magnetic field can be produced by the plasma current that is induced by the primary transformer circuit, i.e., solenoids.

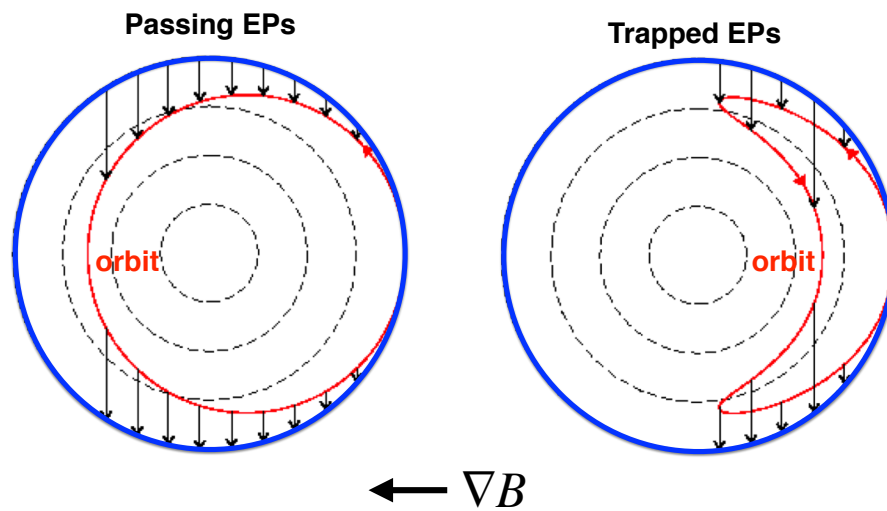


Fig. 1.4 Schematic plot of the particle orbit in tokamak.

Therefore, the tokamak has to be under the pulsed operation, since the current in the solenoids has to be continuously ramped up/down to induce the toroidal electric field to maintain the plasma current and thus the poloidal magnetic field. Alternatively, the complex current drive system from various waves, such as lower hybrid wave, electron cyclotron waves or neutral beam injection driven current, should be developed to sustain the toroidal current of the plasma for the future steady state operation of tokamak type fusion reactor.

Unfortunately, the large toroidal plasma current will induce the various magnetohydrodynamics (MHD) instabilities, such as kink/tearing mode. These instabilities sometimes induce the major disruption of the plasma and damage the plasma facing materials and device too, which should of course be avoided in the future fusion reactor.

1.3 Stellarator and Helical Devices

The concept of the stellarator or helical devices is similar with the basic idea of tokamak, but it does not require inducing net toroidal plasma current, since the poloidal magnetic field is generated by the external coil. Naturally, there is also no risk for the disruption induced by the large net toroidal current. As a cost, the design of the magnetic coil is much more complex. Here we introduce a helical device, i.e. Large Helical Device (LHD) as an example. The schematic drawing of LHD is shown in Fig. 1.5. The LHD has one pair of the continuous helical coils having $l = 2$ and $N = 10$, where l and N are the poloidal and toroidal pole number respectively. The major radius of the helical coil windings is $R = 3.9m$ and the minor radius of coil is $a = 0.975m$ (Watanabe et al., 2010). The toroidal and poloidal magnetic are produced by the helical coils.

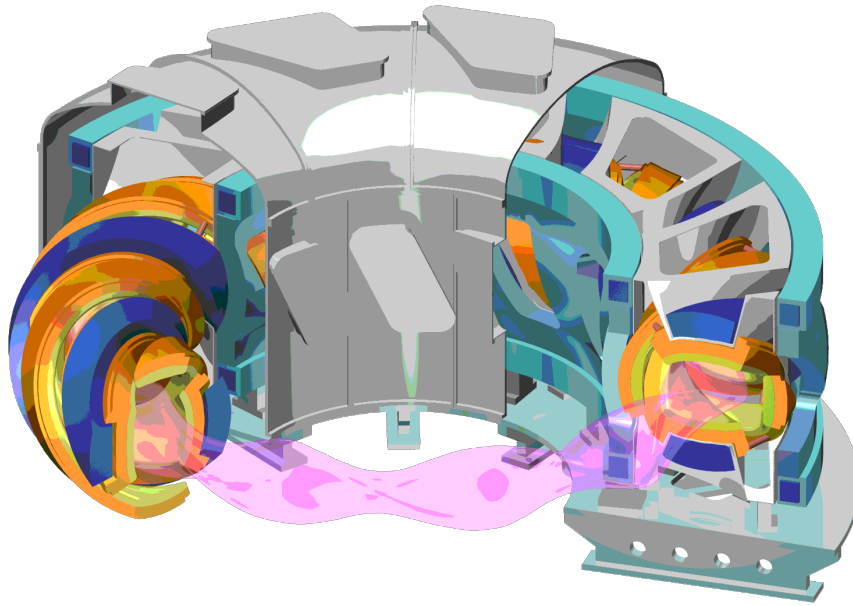


Fig. 1.5 Schematic drawing of a helical device (URL: www.nifs.ac.jp).

Similar with poloidal coils in tokamak, three pairs of the poloidal coils are designed to control the magnetic axis position and the ellipticity of the plasma cross-section (Watanabe et al., 2010). The closed magnetic surfaces including the last closed magnetic surface is similar with a rotating elliptic along the toroidal direction, surrounding by a ergodic layer. The rotational transform increases with the increase of the minor radius, opposite to the tendency in tokamak. In the plasma core, the magnetic shear is quite small and in the plasma

peripheral region, the magnetic shear is large. The magnetic hill(well) is defined with

$$\hat{W} = \frac{V}{\langle B^2 \rangle} \frac{d}{dV} \langle B^2 \rangle \quad (1.12)$$

as $d\hat{W}/dV > 0 (< 0)$. Here $\langle \dots \rangle$ is the average along the magnetic field line, $\langle \dots \rangle \equiv \int_0^L \frac{Q}{B} dl / \int_0^L \frac{dl}{B}$. In other words, the magnetic well is defined by the inequality,

$$\oint \kappa_\psi \frac{dl}{B} > 0, \quad (1.13)$$

where,

$$\kappa_\psi = \frac{1}{2} \frac{\partial B^2}{\partial \psi} \quad (1.14)$$

This means that the averaged magnetic curvature along the field line is positive.

In the plasma core of LHD, the height of magnetic hill is low and it becomes high in the plasma peripheral region. Due to the absence of the net toroidal plasma current, the plasma in LHD is free from the dangerous current-driven instabilities. However, pressure-driven instabilities might be destabilized. It should be noted that the destabilization of the ideal interchange mode is strongly related with the magnetic shear and magnetic hill. That is, the ideal interchange mode is easily destabilized where the magnetic shear is weak and the height of magnetic hill is high.

1.4 MHD instabilities driven by trapped Energetic Particles

Good confinement of energetic ions (EPs) such as alpha particles is crucial for sustaining deuterium-tritium burning plasma. This may be threatened by magnetohydrodynamics (MHD) instabilities destabilized by resonant interactions between EPs and marginally stable or weakly unstable eigenmodes (Gorelenkov et al., 2014). Interesting and important results on instabilities driven by passing EPs are reported from many tokamak and helical devices. On the other hand, so-called fishbone (FB) instability destabilized by trapped EPs was detected in a tokamak three decades ago.

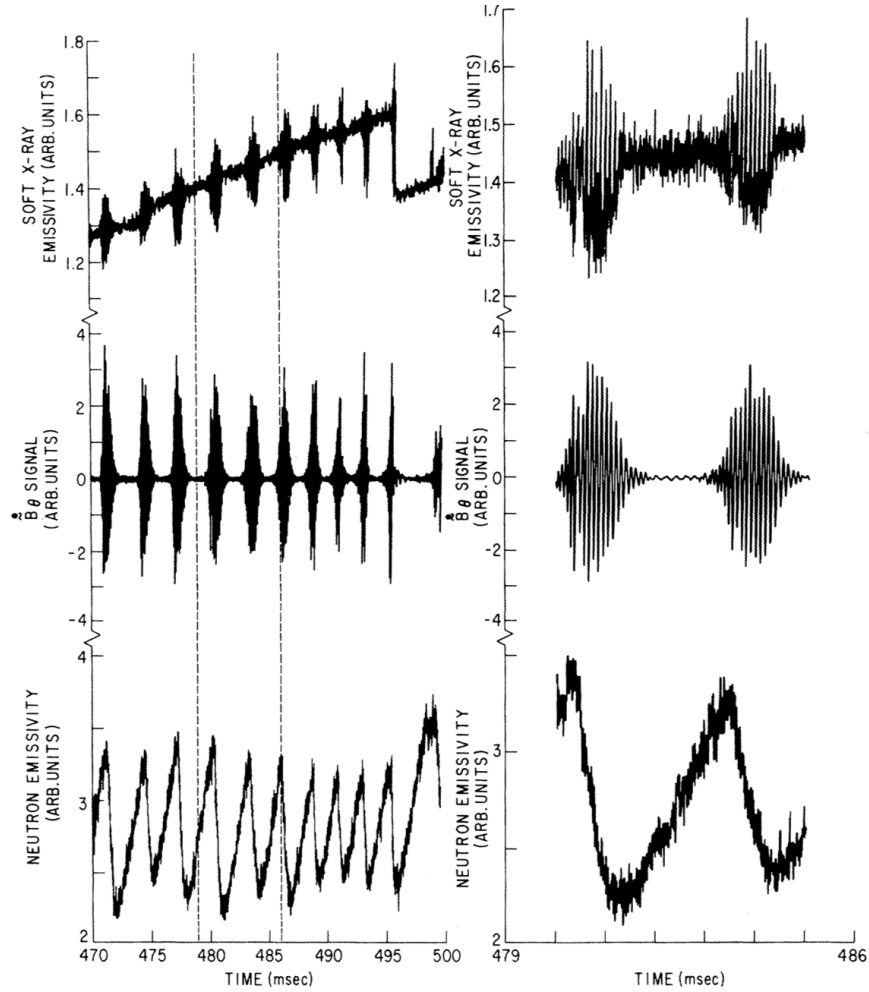


Fig. 1.6 The time evolution of the soft-x-ray emission along a central chord, the \tilde{B}_θ signal from a coil near the outer wall of the vacuum vessel, and the fast neutron flux. Expansion of the data near two "fishbones" is also shown (McGuire et al., 1983).

1.4.1 'Fishbone' instability

A strong bursting Magnetohydrodynamics (MHD) instability is firstly observed in PDX tokamak during the high power injection of nearly perpendicular neutral beams, having $m = 1/n = 1$, where m and n are the poloidal and toroidal mode number, respectively. The neutron yield decreases by as much as 40% at each burst of MHD activity, indicating losses of the energetic beam ions. The typical waveforms are shown in Fig 1.6. In the reference (McGuire et al., 1983), the authors found that the observed mode frequency is comparable to the precession frequency of deeply trapped energetic particles at about the beam injection energy. The authors also speculated that a resonance may exist between the MHD mode and the beam ions, which could enhance the loss of beam particles and it is also possible that

such a resonance could contribute to the instability. Soon later, the L. Chen pointed out that the energetic trapped particles are found to have a destabilizing effect on the $m = 1/n = 1$ internal kink mode in tokamak (Chen et al., 1984). Based on the models, the frequency of the mode is comparable to the toroidal precession frequency of trapped-particles and the growth rate is near the growth rate of the ideal internal kink mode. The details of the model is reviewed below.

In 1986, to mitigate the loss the of EPs induced by fishbone, two of the perpendicular NBI is reoriented to the tangential injection. However, during the injection of tangential NBI, the repetitive bursts with low frequency of MHD activity were observed again, accompanied with a high frequency mode. The decrease of the neutron yield by as much as 20% is observed at each low frequency burst and 5% at each high frequency burst are found. Unlike the 'fishbone' during the perpendicular NBI, the frequency of the burst is comparable to the plasma rotation in the core. Therefore, it cannot be explained by the model proposed by L. Chen (Chen et al., 1984). A new model is proposed by B. Coppi (Coppi and Porcelli, 1986) to explain the 'fishbone' oscillations. According to their model, phase velocity of the mode is equal to the core-ion diamagnetic velocity and the resonant interaction of the mode with the beam ions is viewed as a form of dissipation that allows the release of the mode excitation energy, related to the gradient of the plasma pressure (Coppi and Porcelli, 1986). Interestingly, both type of the fishbones: precessional drift FB and the ion diamagnetic drift fishbone mode are observed in ion-cyclotron-resonance-heated plasma in Joint European Torus plasma (JET) (Nabais et al., 2005).

1.4.2 Off-axis 'Fishbone' mode

Recently, 'fishbone' study has been expanded to the so-called energetic particle driven wall mode (EWM) (Matsunaga et al., 2009) or off-axis fishbone instability (Heidbrink et al., 2011), which is also destabilized by trapped EPs. Much attention is paid to the mode toward the burning plasma experiments because it often triggers the resistive wall mode and disruption. The typical example is shown in Fig 1.7. The initial mode frequency of EWM is close to the precession frequency of the trapped energetic particle, suggesting that the EWM is driven by trapped energetic particles. The mode would follow the basic approach of the model developed by L. Chen (Chen et al., 1984). The loss of energetic particles induced by EWM is investigated by various diagnostics in DIII-D tokamak. The results are shown in Fig. 1.8. (Heidbrink et al., 2011) It should be noted that fast ions are expelled to the outside of the plasma in a 'beacon' (with a fixed phase relative to the mode) as the authors pointed out.

A stability analysis for the resistive wall mode is made in the presence of trapped energetic particles (EPs) in the reference (Hao et al., 2011). The dispersion relation of the EWM is

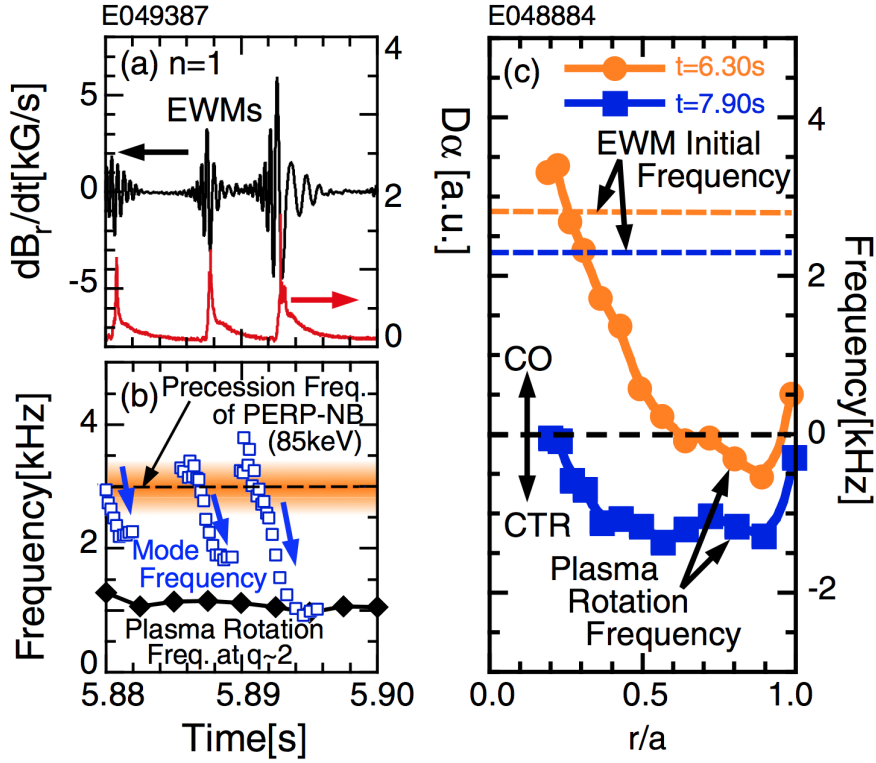


Fig. 1.7 Waveforms of (a) EWM and D_α emission, (b) mode frequency with the plasma rotation frequency at $q \approx 2$. (c) Comparison of plasma rotation profiles measured by CXRS with EWM initial frequency. (Matsunaga et al., 2009)

derived by employing the mode eigenfunction of the resistive wall mode and $m = 2/n = 1$ based on the the similar assumption and model in (Chen et al., 1984). The author concludes that if the perpendicular beta β_\perp exceeds a certain threshold, the EWM with the eigenfunction of external kink mode can occur and the real frequency of the mode is determined by the precession frequency of energetic particles around the mode rational surface.

1.4.3 Energy principle including hot component

To understand the MHD instability driven by the trapped energetic ions, it is of great importance to visit the energy principles. The energy principle with the hot component (contribution from EPs) can be derived from the equation of motion, as follow.

$$\rho_m \frac{\partial \mathbf{u}}{\partial t} = -\nabla \cdot \mathbf{P} + \mathbf{j} \times \mathbf{B} \quad (1.15)$$

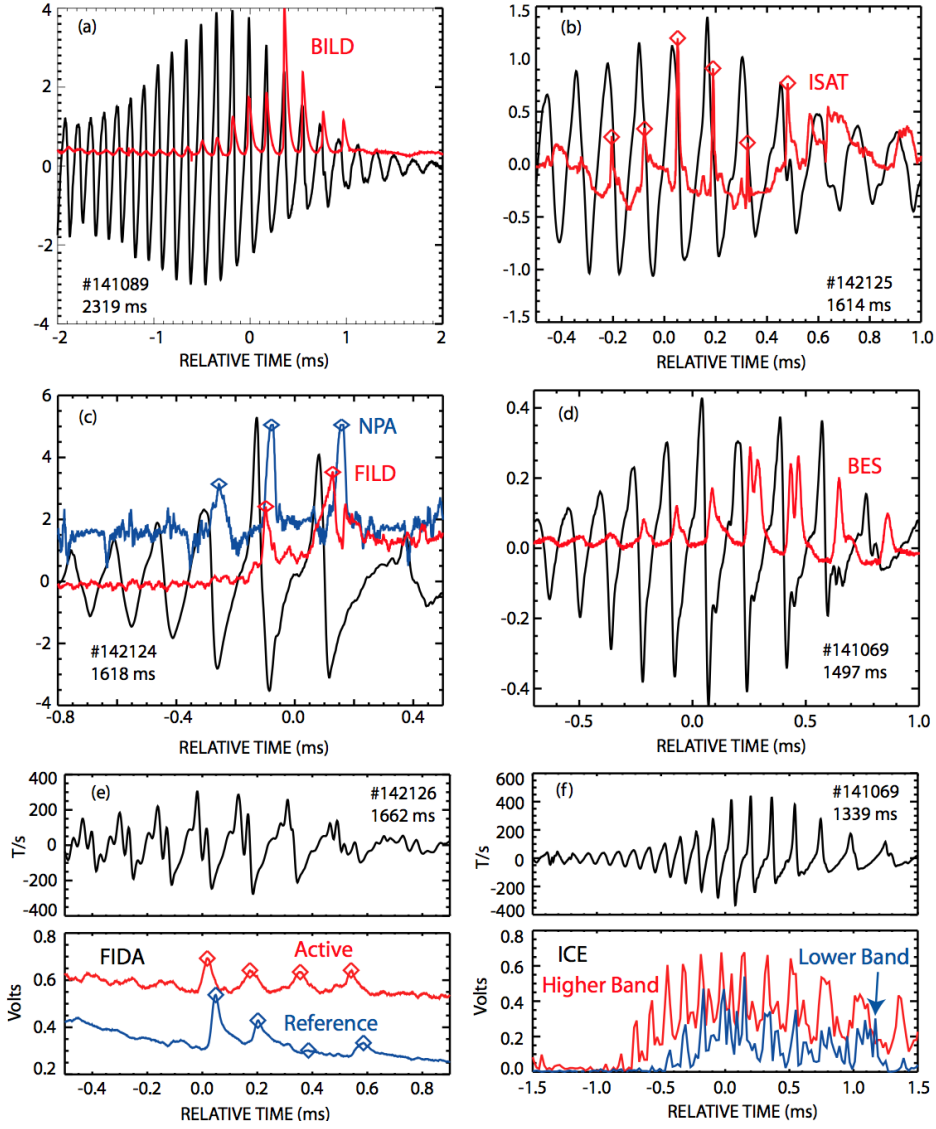


Fig. 1.8 Loss-detector data during a fishbone burst from (a) the BILD foil, (b) the Langmuir probe I_{sat} tip, (c) the FILD scintillator and SSNPA detector, (d) a central BES channel on a discharge without any beam emission, (e) active and passive f-FIDA channels and (f) ICE passband signals that include the fundamental cyclotron resonance (lower band) or the first few harmonics (higher band). The diamonds represent peaks used to measure the phase relative to the Mirnov signal. (Heidbrink et al., 2011)

The first-order linearized equations are,

$$-\rho_m \omega^2 \xi = -\nabla \cdot \tilde{\mathbf{P}}_h - \nabla \cdot \tilde{\mathbf{P}}_b + \mathbf{j} \times \tilde{\mathbf{B}} + \tilde{\mathbf{j}} \times \mathbf{B}, \quad (1.16)$$

where a normal mode $\xi(\mathbf{r}, t) = \xi(\mathbf{r}) \exp(-i\omega t)$ is considered. \tilde{P}_h and \tilde{P}_b is the first order pressure perturbation of the hot component and bulk component of plasma, respectively. The

following ideal MHD relations holds:

$$\tilde{\mathbf{E}}_{\perp} = i\omega \boldsymbol{\xi} \times \mathbf{B}_0, \quad \tilde{\mathbf{E}}_{\parallel} = 0, \quad \tilde{\mathbf{B}} = \nabla \times (\boldsymbol{\xi} \times \mathbf{B}_0),$$

By multiplying $\frac{1}{2} \int d\mathbf{r} \boldsymbol{\xi}^*$ on the eq. (1.16), we have

$$\delta I + \delta W_{MHD} + \delta W_k = 0, \quad (1.17)$$

where,

$$\delta I = -\frac{\omega^2}{2} \int \rho_m |\boldsymbol{\xi}|^2 d\mathbf{r}, \quad (1.18)$$

$$\delta W_k = \frac{1}{2} \int \boldsymbol{\xi} \cdot \nabla \cdot \tilde{\mathbf{P}}_h d\mathbf{r}, \quad (1.19)$$

If assuming the MHD instability, which is destabilized by the bulk plasma, is marginally stable, i.e., $\delta W_{MHD} \sim 0$, the mode can be destabilized by the free energy contributed from the hot component, i.e., δW_k . The integral of hot component contributed from the EPs is given by the reference (Chen et al., 1984), as follow.

$$\frac{\delta W_k}{2\pi R} = -2^{5/2} \pi^2 m \int r dr \int d(\lambda B_0) \int dE E^{5/2} K_b \frac{2\bar{J}^* \bar{J} Q}{\omega - \langle \omega_d \rangle}, \quad (1.20)$$

where,

$$J \equiv -\frac{v_{\parallel}^2 + v_{\parallel}^2/2}{v_{\perp}^2} (\boldsymbol{\kappa} \cdot \boldsymbol{\xi}), \quad (1.21)$$

$$Q \equiv \frac{\mathbf{k} \times \mathbf{b}_0 \cdot \nabla f_0}{eB_0} + \omega \frac{\partial f_0}{\partial U_0}, \quad (1.22)$$

If the distribution function of the beam is assumed as,

$$f_0 = c_0 \frac{\delta(\lambda - \lambda_0)}{E^{3/2}}, \quad (1.23)$$

where the λ_0 is the initial pitch angle between the beam and the magnetic field line. The plasma displacement ξ_r for internal kink mode is assumed to be constant for $0 < r < r_s$ and $\xi_r = 0$ for $r > r_s$. Then the dispersion relation can be derived, as follows,

$$-i\Omega\alpha_h + \Omega \ln \left(1 - \frac{1}{\Omega} \right) + 1 = 0, \quad (1.24)$$

where $\Omega \equiv \omega/\omega_{dm}$, ω_{dm} is the averaged precession frequency at the injected energy of beam ions and $\alpha_h \equiv \frac{\omega_{dm}}{\omega_A} \left(\pi \left(\frac{K_2}{K_b} \right)^2 (-\beta'_h) R \right)^{-1}$. The detail derivation could be found in the Appendix A. The simple analysis of the dispersion relation reveals that a threshold for β'_h is necessary to meet for destabilization of the mode,. That is,

$$-\frac{\partial \beta_h}{\partial r} > \frac{\omega_{dm}}{\omega_A} \frac{1}{R\pi^2} \frac{K_b^2}{K_2^2} \quad (1.25)$$

Similar with the analysis for the EP-driven internal kink mode, the dispersion relation of the EP-driven external kink mode could be derived by employing the mode displacement as (Hao et al., 2011),

$$\xi_{\perp} = \text{amp} \rho^{m-1} (\mathbf{e}_r + i\mathbf{e}_{\theta}) e^{i(m\theta - n\phi)} / F_0, \quad (1.26)$$

where m and n are poloidal and toroidal mode numbers, $F_0 = (m - nq)a / (Rq)$. The normalized dispersion relation is given as follows.

$$\delta W_b + \left(\delta W^{\infty} - \delta W^b \right) / [1 - i(\Omega_r + i\gamma/\omega_{ds}) \omega_{ds} \tau_w^*] + \delta W_{K0} = 0 \quad (1.27)$$

The detail of the derivation can be found in the reference (Hao et al., 2011).

1.5 Resonance Conditions

1.5.1 Resonance condition in tokamak

Before deriving the equation of the resonance condition in stellarator and helical plasmas, we shortly discuss the resonance in tokamak, which is a simplified case. From the eq. (1.20), the resonance condition in tokamak is given by,

$$\omega - \langle \omega_d \rangle = 0, \quad (1.28)$$

where ω_d is as follows, and \mathbf{k} is the wave vector of the MHD mode,

$$\omega_d \equiv \mathbf{k} \cdot \mathbf{v}_m, \quad (1.29)$$

A simple picture to understand the resonance condition in tokamak for trapped energetic ions, having $\mathbf{v}_{\perp} \gg \mathbf{v}_{\parallel}$ is described here. Considering the precession motion of trapped particle, having banana orbit, the averaged drift velocity in toroidal direction $\langle \mathbf{v}_{\phi} \rangle$ can be derived as

follows,

$$\langle v_\phi \rangle = \oint_{\tau_b} (v_D \cos \alpha) dt / \oint_{\tau_b} dt \sim \langle v_D \cos \alpha \rangle, \quad (1.30)$$

$$\langle v_\theta \rangle = \oint_{\tau_b} (v_D \sin \alpha) dt / \oint_{\tau_b} dt \equiv 0, \quad (1.31)$$

where $\oint_{\tau_b} dt$ means that integration for one bounce motion in poloidal direction, i.e. $\oint_{\theta=0}^{\theta=2\pi} d\theta \equiv \oint_{\tau_b} dt$. The term α is the pitch angle of the magnetic valley in tokamak, since the trapped EPs in tokamak can only precess toroidally, i.e., $\alpha = 0$. Therefore the resonant frequency is,

$$\omega = \mathbf{k}_\phi \cdot \langle \mathbf{v}_\phi \rangle + \mathbf{k}_\theta \cdot \langle \mathbf{v}_\theta \rangle = \frac{n}{R} v_D = n \omega_D, \quad (1.32)$$

This means that the frequency of the MHD modes is determined by the toroidal precession drift motion of the orbit.

1.5.2 Resonance condition in Stellarator and Helical Plasmas

Comparably, the resonance condition in stellarator and helical plasmas is much more complicated compared with that in tokamak. The complete and strict derivation is fairly lengthy and here we only introduce a simple way to derive (Kolesnichenko et al., 2002). The energy exchange rate between the energetic particles and the waves is described by the following equation:

$$\frac{d\mathcal{E}}{dt} = e (v_\parallel \tilde{E}_\parallel + \mathbf{v}_d \cdot \tilde{\mathbf{E}}_\perp) + \mu_p \frac{\partial \tilde{B}}{\partial t}, \quad (1.33)$$

For MHD waves, since $E_\parallel \sim 0$, then

$$v_\parallel E_\parallel \ll \mathbf{v}_d \cdot \tilde{\mathbf{E}}_\perp, \quad (1.34)$$

and the third term $\mu_p \partial \tilde{B} / \partial t$ might be important for trapped EPs, which $\mu_p \gg 0$ (Kolesnichenko et al., 2002). For low frequency waves lower than the ion cyclotron frequency, this term might be neglected. We assume the equilibrium radial electric field is not important, i.e. $E_0 \sim 0$, then the drift motion of EPs is mainly dominated by the magnetic drift motion as followings,

$$\mathbf{v}_d = \frac{1}{\Omega} \mathbf{b} \times \left(\frac{\mu}{m} \nabla B + v_\parallel^2 \boldsymbol{\kappa} \right), \quad (1.35)$$

The magnetic field in a 3D toroidal plasma can be generally expanded into the Fourier series given by,

$$B_0 = \bar{B} \left(1 + \sum_{\mu, \nu} \varepsilon_B(r)^{(\mu\nu)} \cos(\mu\theta - \nu\phi) \right), \quad (1.36)$$

Therefore, the drift motion can be written under the Fourier expansion and neglecting the terms of the ordering of ε^2 , given by,

$$v_D^1 = \frac{(v^2 + v_{\parallel}^2 \bar{B})}{2\omega_B} \sum_{\mu, \nu} \varepsilon_B^{(\mu\nu)} \mu \sin(\mu\theta - \nu\phi), \quad (1.37)$$

$$v_D^2 = \frac{(v^2 + v_{\parallel}^2 \bar{B})}{2\omega_B} \sum_{\mu, \nu} \varepsilon_B^{(\mu\nu)'} \mu \cos(\mu\theta - \nu\phi) + \frac{4\pi v_{\parallel}^2}{\omega_B \bar{B}} \frac{\partial p_0}{\partial \psi}, \quad (1.38)$$

$$v_D^3 \approx 0, \quad (1.39)$$

The perturbation from MHD inabability can be written as,

$$\tilde{E}_{\perp} = -\nabla \tilde{\phi}, \quad (1.40)$$

$$\phi_{m,n} = \sum_{m,n} \phi_{m,n}(r) \exp(im\theta - in\phi - i\omega t), \quad (1.41)$$

Thus,

$$\begin{aligned} \mathbf{v}_D \cdot \nabla_{\perp} \tilde{\phi} &= (\phi_{m,n})' \frac{(v^2 + v_{\parallel}^2 \bar{B})}{2\omega_B} \sum_{\mu, \nu} \varepsilon_B^{(\mu\nu)} \mu \sin(\mu\theta - \nu\phi) \exp(im\theta - in\phi - i\omega t) \\ &+ m\phi_{m,n} \left(\frac{(v^2 + v_{\parallel}^2 \bar{B})}{2\omega_B} \sum_{\mu, \nu} \varepsilon_B^{(\mu\nu)'} \mu \cos(\mu\theta - \nu\phi) \right) \exp(im\theta - in\phi - i\omega t) \\ &+ m\phi_{m,n} \left(\frac{4\pi v_{\parallel}^2}{\omega_B \bar{B}} \frac{\partial p_0}{\partial \psi} \right) \exp(im\theta - in\phi - i\omega t) \end{aligned} \quad (1.42)$$

This indicates that the resonance condition is contributed from the term v_D^2 as follows,

$$\pm(\mu\theta - \nu\phi) + (m\theta - n\phi - \omega t) = 0, \quad (1.43)$$

or by the last term of the eq. (1.42)

$$m\theta - n\phi - \omega t = 0, \quad (1.44)$$

Formalizing the equation gives,

$$\omega - (m + j\mu) \langle \omega_\theta \rangle + (n + j\nu) \langle \omega_\phi \rangle = 0, \quad (1.45)$$

where, $j = 0, \pm 1$ and $\langle \dots \rangle$ means the averaged precession frequency of the energetic ions. ϕ'_{mn} is $\partial \phi_{mn} / \partial r$ and $\epsilon_B^{(\mu\nu)'} is $\partial \epsilon_B^{\mu\nu} / \partial r$.$

It should be noted that the case of $j = 0$ recovers the resonance condition for tokamak. The magnetic spectrum for a stellarator/ helical plasma, i.e., an LHD plasma, is shown in the following figure.

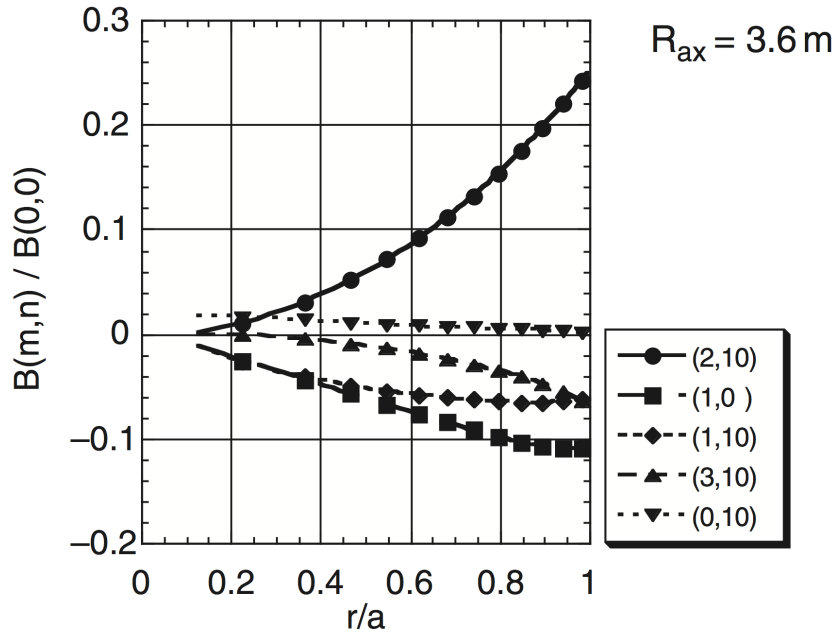


Fig. 1.9 Radial profiles of the Fourier components of the magnetic field strength in a low β plasma of $R_{ax} = 3.6m$ configuration.

The deeply trapped energetic ions in LHD is called 'helically trapped energetic ions' and the detail orbits will be introduced in the later section. The relation between the poloidal and toroidal precession frequency can be written as,

$$\langle \omega_\phi \rangle = \frac{\langle \omega_\theta \rangle}{5}, \quad (1.46)$$

Therefore, the resonance condition in LHD is as follows,

$$\omega_{MHD} = \left(m - \frac{n}{5} + j \left(\mu - \frac{\nu}{5} \right) \right) \langle \omega_{\theta} \rangle, \quad (1.47)$$

For $m = 1/n = 1$ mode, i.e., helically trapped energetic ions driven resistive interchange mode analyzed in this thesis, the possible resonance frequencies are shown in the table 1.1. Interestingly, the calculated resonance frequency indicates that the mode frequency can be opposite to the poloidal precession frequency of helically trapped energetic ions, i.e, $\omega_{mode} = -1.2\langle \omega_{\theta} \rangle$.

Table 1.1 Potential resonance frequency for $m = 1/n = 1$ mode in an LHD plasma

m	n	j	μ	ν	ω_{MHD}
1	1	1	2	10	$0.8\langle \omega_{\theta} \rangle$
1	1	0	2	10	$0.8\langle \omega_{\theta} \rangle$
1	1	-1	2	10	$0.8\langle \omega_{\theta} \rangle$
1	1	1	1	0	$1.8\langle \omega_{\theta} \rangle$
1	1	0	1	0	$0.8\langle \omega_{\theta} \rangle$
1	1	-1	1	0	$-0.2\langle \omega_{\theta} \rangle$
1	1	1	1	10	$-0.2\langle \omega_{\theta} \rangle$
1	1	0	1	10	$0.8\langle \omega_{\theta} \rangle$
1	1	-1	1	10	$1.8\langle \omega_{\theta} \rangle$
1	1	1	3	10	$1.8\langle \omega_{\theta} \rangle$
1	1	0	3	10	$0.8\langle \omega_{\theta} \rangle$
1	1	-1	3	10	$-0.2\langle \omega_{\theta} \rangle$
1	1	1	0	10	$-1.2\langle \omega_{\theta} \rangle$
1	1	0	0	10	$0.8\langle \omega_{\theta} \rangle$
1	1	-1	0	10	$2.8\langle \omega_{\theta} \rangle$

Chapter 2

Experimental Setup

In this chapter, we will introduce the main diagnostics systems, which will be employed in the analysis of the helically trapped energetic ion driven resistive interchange mode below.

2.1 Soft X-ray systems

In the experimental campaigns of LHD, various kind of MHD fluctuations excited in core and edge plasma regions have clearly been detected by this installed soft X-ray diagnostic system (Du et al., 2012). For example, the characteristic behaviors of the ELM activity in H-mode plasmas and the helically trapped energetic ion driven resistive interchange mode induced by the perpendicular neutral beam injection (NBI) were analyzed by the soft X-ray data. Hereafter, we firstly introduce the soft X-ray system which we developed for MHD studies.

2.1.1 Principle of soft X-ray diagnostic system

The radiation that occurs when a free electron is decelerated in the electric field of a charged particle is called bremsstrahlung. In fact, for collisions with a positively charged particle such as an ion, the radiative event can consist of free-free transition, in which the final state of the electron is also free and free-bound transition, in which the electron is captured by the ion into a bound final state. The free-bound transition are often called recombination radiation. Note that the electron-electron collisions will be ignored because their contribution to radiation is generally small unless their velocity are sufficiently relativistic (Hutchinson,

1987). The free-free radiation from collisions with the ions are expressed as followings:

$$j(\nu) = 8 \times 10^{-55} n_e n_i Z^2 \left(\frac{T_e}{eV} \right)^{-1/2} e^{-h\nu/T_e} \times \bar{g}_{ff} \quad (2.1)$$

In the soft X-ray diagnostic system, the upper limit of energy spectrum of the free-free radiation will be determined by the detector responsibility, i.e., thickness of effective silicon material in photo-diode ($D(h\nu)$). The lower limit will be determined by a beryllium foil to cut the visible light as a filter, i.e., $F(h\nu)$. Therefore, the soft X-ray emission intensity detected by soft X-ray system in experiment is as follows,

$$I_{sx} \propto \int_l i_{sx} dl \quad (2.2)$$

$$\propto \int_l \left(\int_0^\infty n_e n_i Z^2 T_e^{-1/2} e^{-E/T_e} D(E) F(E) dE \right) dl \quad (2.3)$$

$$\approx \int_l \left(-n_e n_i Z^2 T_e^{1/2} \left(\int_{E_{min}}^{E_{max}} e^{-E/T_e} d\left(-\frac{E}{T_e}\right) \right) \right) dl \quad (2.4)$$

$$\approx \int_l \left(n_e n_i Z^2 T_e^{1/2} e^{-E_{min}/T_e} \right) dl, \quad (2.5)$$

where $E_{max} \gg T_e$ and E_{min} is the cut-off energy by the filter, i.e., a beryllium foil there. In present case, $E_c \sim 1keV$ for $15\mu m$ B_e foil on the assumption of $n_i \sim n_e$, the calculated intensity of volume soft X-ray emission (i_{sx}) is shown in Fig. 2.1. Moreover, the fluctuation of soft X-ray emission, i.e., \tilde{i}_{sx} can be also derived as follows.

$$\frac{d}{dx} (\ln(i_{sx})) \propto \frac{d}{dx} \left(\ln(n_e) + \ln(n_i) + 2\ln(Z) + \frac{1}{2}\ln(T_e) - \frac{E_c}{T_e} \right) \quad (2.6)$$

$$\frac{i'_{sx}}{i_{sx}} = \frac{n'_e}{n_e} + \frac{n'_i}{n_i} + \frac{2Z'}{Z} + \frac{T'_e}{2T_e} + \frac{E_c}{T_e^2} T'_e \quad (2.7)$$

$$\frac{\tilde{i}_{sx}}{i_{sx}} = \frac{\tilde{n}_e}{n_e} + \frac{\tilde{n}_i}{n_i} + \frac{2\tilde{Z}}{Z} + \frac{\tilde{T}_e}{T_e} \left(\frac{1}{2} + \frac{E_c}{T_e} \right) \quad (2.8)$$

If we assume that the electron density and temperature are the flux function, the iso-radiation surface of the soft X-ray emission can be a good estimate of the flux surface. As seen from the eq. (2.8), the soft X-ray emission fluctuations reflect dominantly the electron temperature fluctuations in the plasma region of $T_e \ll E_c = E_{min}$. However, in the region of $T_e \gg E_c = E_{min}$, the soft X-ray fluctuations are mainly determined by the density fluctuations.

MHD instabilities would cause the deformation of the magnetic flux surfaces. Therefore, the internal structure of the MHD activities can be studied from the soft X-ray emission.

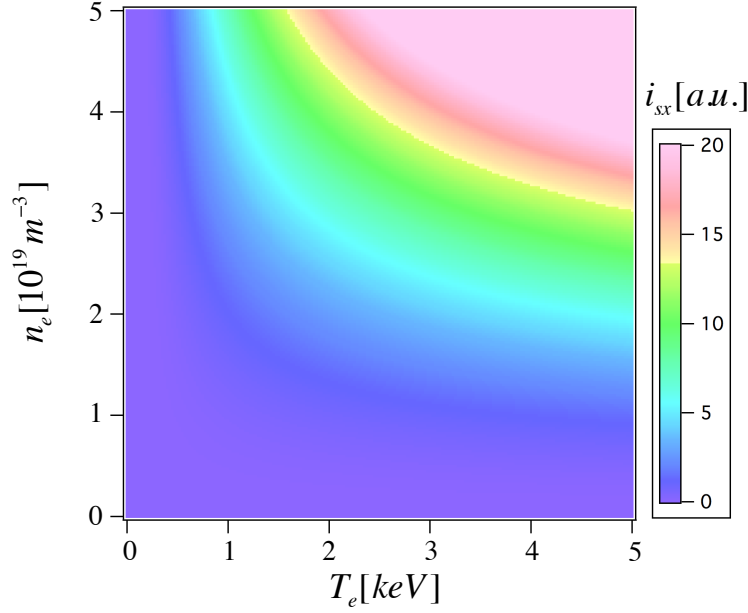


Fig. 2.1 Soft X-ray emission as the function of the electron density and temperature.

From the Taylor expansion, the plasma displacement can be derived as,

$$i_{sx}(x) = i_{sx}(a) + i'_{sx}(a)(x - a) + \dots, \quad (2.9)$$

Therefore, the plasma displacement could be expressed by,

$$\xi_r \sim \frac{\tilde{i}_{sx}}{\nabla i_{sx}}, \quad (2.10)$$

2.1.2 Development of an array system of soft X-ray detectors with large sensitive area

A 17-channel soft X-ray diagnostic system was developed for a study of magnetohydrodynamics (MHD) fluctuations and it was installed on the LHD. The absolute X-ray ultraviolet photo-diodes (AXUV-100 model) with the 5.6 times larger sensitive area ($10\text{mm} \times 10\text{mm}$) than the previous system (Du et al., 2012), which are made by International Radiation Detectors, Inc., are adopted as the new detectors. The detectors have an effective silicon thickness of 100 microns. The sensitivity of the detector is shown in Fig. 2.2 (blue curve).

The detector is sensitive to the photon energy up to 30keV . Specifically, the high sensitive energy range for the coming photons is from 1keV to 6keV . A beryllium foil of $15\mu\text{m}$ thickness is arranged before the pinhole to shut down the visible light and vacuum ultraviolet

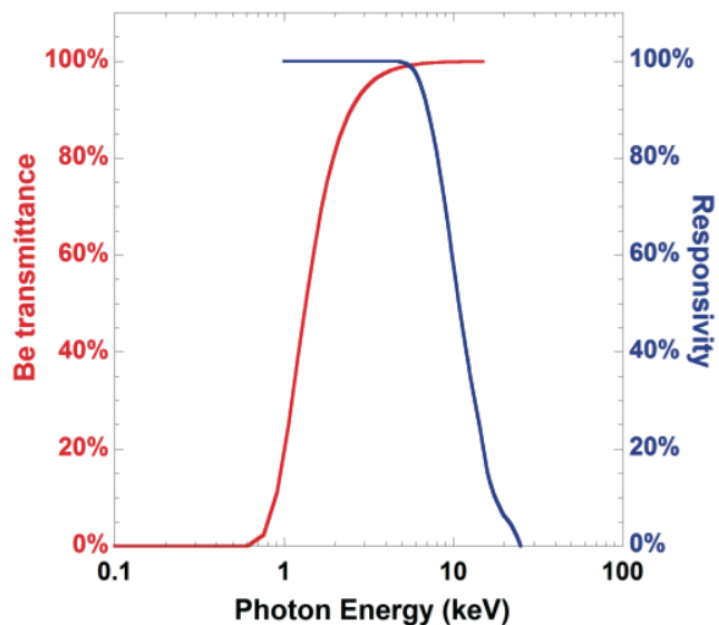


Fig. 2.2 Responsibility of AXUV photo-diodes with 100 microns effective S_i thickness (blue curve) and the transmittance coefficient for $15\mu\text{m}$ B_e foil filter (red curve).

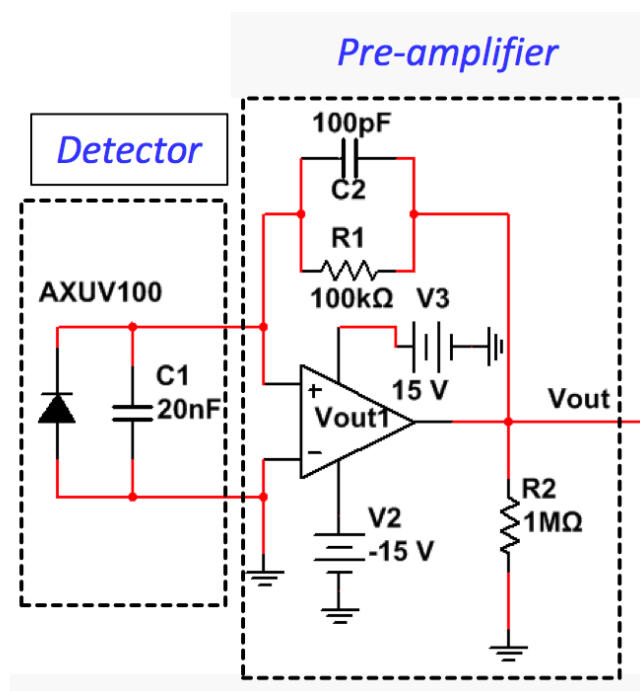


Fig. 2.3 The circuit of the pre-amplifier of soft X-ray system.

emissions. The transmission coefficient is shown in Fig. 2.2 (red curve). In other words, it determines the lowest coming photon energy, around $1.5keV$.

When the photons enter the detector, the current is induced in the detector. In the pre-amplifier, the current is converted to the voltage signal and then further amplified inside the vacuum vessel. The circuit of the pre-amplifier is shown in Fig. 2.3. In the circuit, the resistivity to convert current to voltage is chosen as $100k\Omega$. The effective capacitance is estimated as $100pF$. Then the upper limit of the frequency response $f_c = 1/\pi R_1 C_1$ is about $16kHz$. Therefore, the low frequency MHD modes less than $10kHz$ can be detected by this soft X-ray array system with large sensitive area at present.

The schematic plot of the arrangement of the system is shown in Fig. 2.4. The sightlines are designed to cover the whole vertical elongated poloidal cross section of the plasma with $3.8cm$ space separation at the equatorial plane of an LHD plasma. A trapezoid shaped aluminum box $1.6m$ in height is designed to support and shield the detector. A pinhole ($25mm \times 7mm$) is opened on the top of the box to give the image of the plasma.

Here, the performance of the new detector system is roughly estimated under the arrangement of Fig. 2.5. Consider the radiation from the plasma with a distance s from the pinhole. The emission from the area $[a \times (s/t)] \times [b \times (s/t)]$ enters the detector. The length $a(b)$ and $c(d)$ denote the size of the detector and pinhole in the radial (toroidal) direction, respectively. The distance from the detector to the pinhole and from the pinhole to the plasma is denoted as t and s . The solid angle where the emission enters the pinhole is in proportional to $(c \times d)/(4\pi s^2)$. Since the total emission is a line integral of the emission over the sight line, the value $(abcd)/(4\pi t^2)$ can be used as a good measure of the brightness of the system. Radial and toroidal resolution of the system is also roughly estimated as the $c \times [(s+t)/t]$ and $d \times [(s+t)/t]$ respectively. The characteristics of the new system with detector of large sensitive area and previous systems are summarized in Table 2.1.

Table 2.1 Comparison the arrangements of the old and the new soft X-ray detector system

SX system	a	b	c	d	t	s	Brightness	Δr	$R\Delta\phi$
	mm	mm	mm	mm	mm	mm	[a.u.]	mm	mm
Old SX system	12	1.5	9	5	900	4274	80	52	29
New SX system	10	10	25	7	1150	2400	1053	77	22

According to the table 2.1, this new detector system can expect at least 10 times larger signal level than the old system. In order to further improve the signal to noise ratio in the complicated electromagnetic environment of the experimental hall, condensers with large capacitance ($6.8mF$) are inserted in the power supply to mitigate the large impulse noise

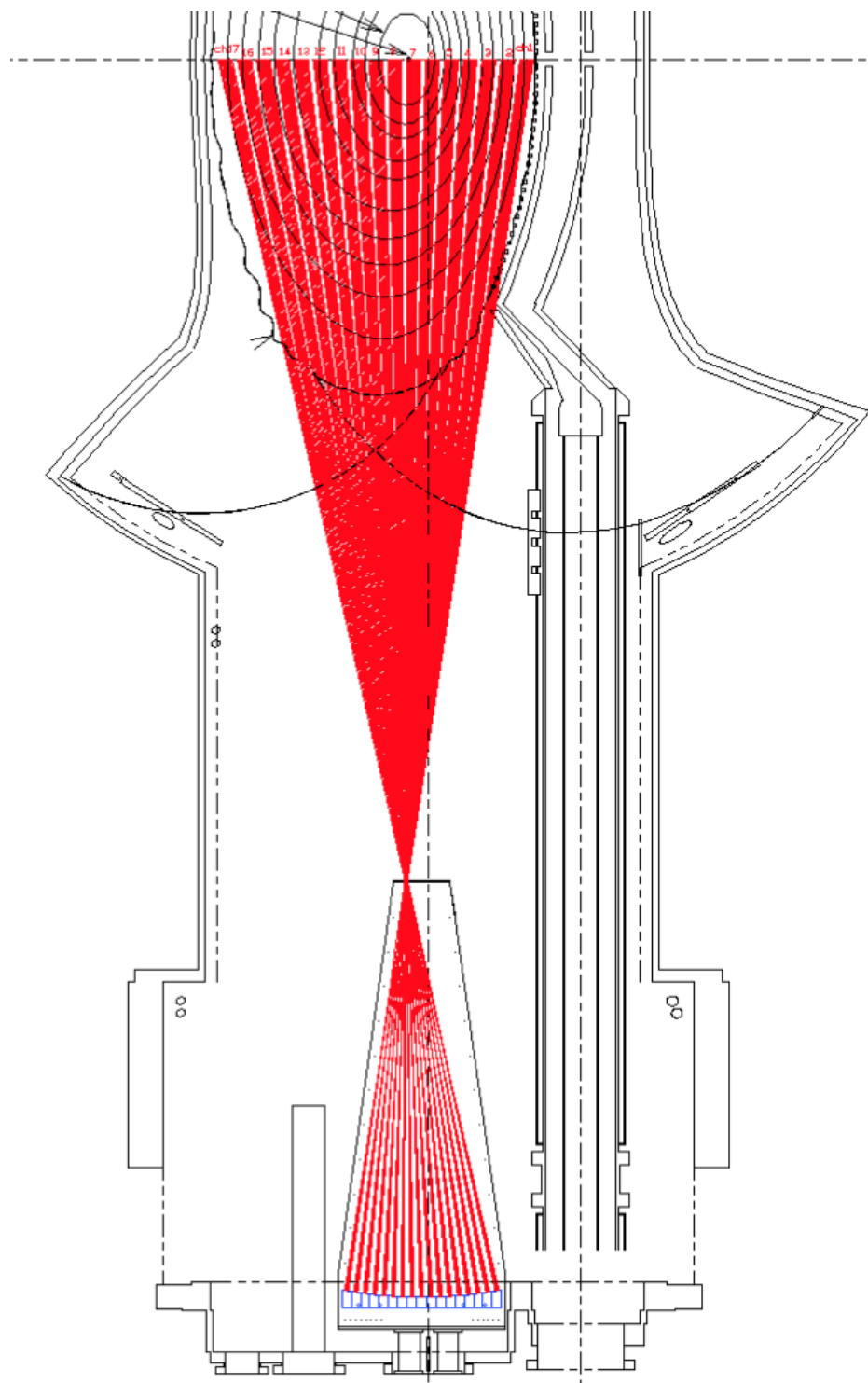


Fig. 2.4 The schematic plot of the layout of soft X-ray system and arrangement of the sightlines.

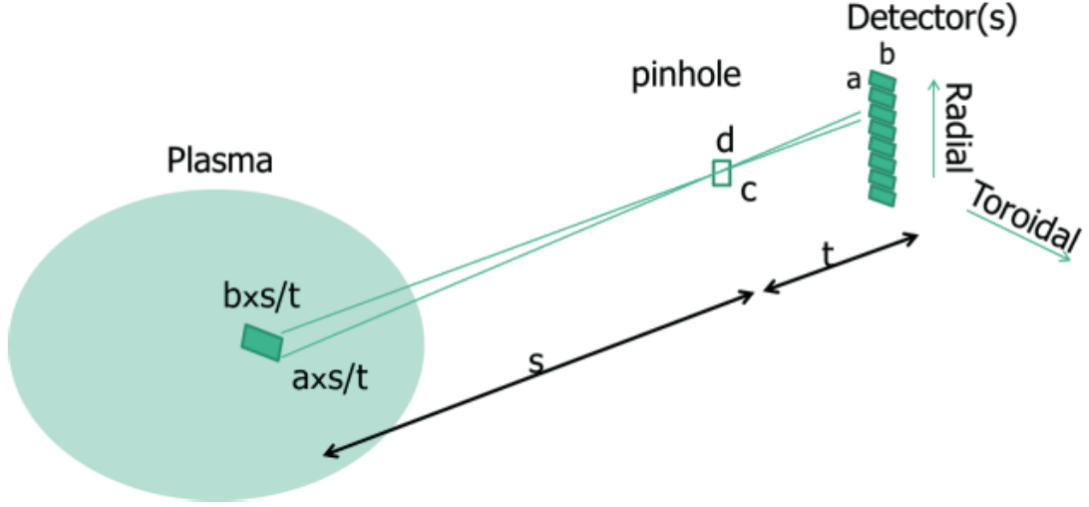


Fig. 2.5 Layouts of the installed soft X-ray system.

from the turn-on or turn-off of the NBI power supply. After using the condenser, the noise level around $10kHz$ is reduced by a factor of 10.

2.1.3 A model to derive mode eigenfunction from soft X-ray system

Since the soft X-ray system detects the soft x-ray emission, which is volume-integrated along the sightlines through a pinhole placed in front of the detectors, as seen from Fig. 2.5, the determination of mode eigenfunction from soft X-ray emissions is not as straightforward as the local fluctuation measurement, such as electron cyclotron emission (ECE) of which diagnostic system in LHD is also briefly introduced in sub-section 2.2.2. In LHD, a model is successfully employed to help derive the mode eigenfunction. In net current free plasmas of LHD, the MHD instabilities are pressure driven instabilities, such as resistive and ideal interchange mode. Thus, the local fluctuation of soft X-ray emission can be roughly expressed for the instabilities localized at a certain radial location, as follows.

$$\tilde{i}_{sx} = \xi_r \cdot \exp \left(- \left(\frac{\rho - \rho_{rs}}{w_{mode}} \right)^2 \right) \cos(m\theta - n\zeta - \omega t) \cdot \nabla i_{sx}, \quad (2.11)$$

where m and n are the poloidal and toroidal mode numbers, respectively, the θ and ζ are the poloidal and toroidal angles in boozier coordinate, ρ_{rs} is the peak location of the mode, w_{mode} is the radial width of the mode and ω is the frequency of the mode in plasma frame, i.e., $\omega = \omega_{doppler} + \omega_{mode}$.

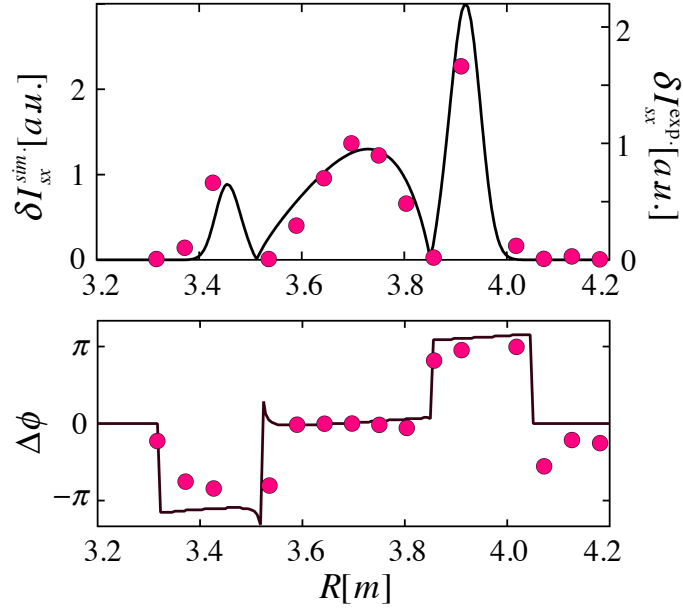


Fig. 2.6 The radial profiles of the measured soft X-ray fluctuation (solid dot) and the best-fitted one simulated from the modeled one (curve) shown in upper figure. The radial profiles of the measured phase differences among different channels of soft X-ray fluctuation (solid dot) and the simulated one from the best-fitting result in lower figure.

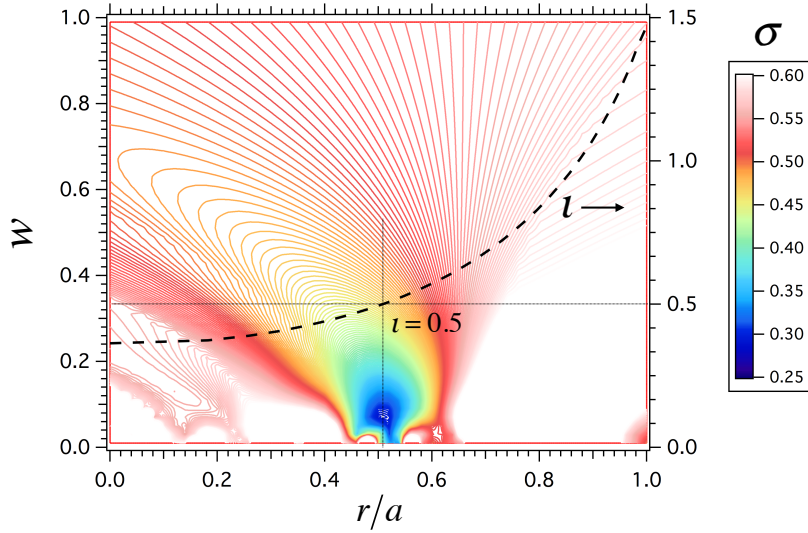


Fig. 2.7 The scan of the mode width and mode location to obtain the best-fitted result for the measured soft X-ray emission.

Comparably, the observed signal of the soft X-ray system is the line integrated one, as follows.

$$\tilde{I}_{sx} = \int_V \tilde{i}_{sx} dV \quad (2.12)$$

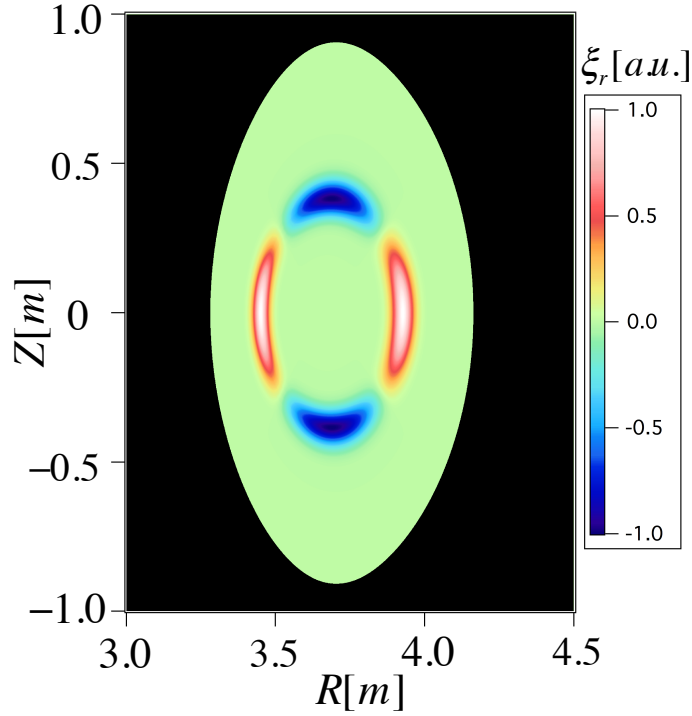


Fig. 2.8 The mode eigenfunction best fitted the measured soft X-ray fluctuation.

That is, if the shape and the phase of emission signals at all sightlines calculated by the sightline integration of the model emission profile expressed as eq. (2.11) are best-fitted to those of the measured soft X-ray fluctuation signals by scanning the unknown variables (m , ρ_{rs} and w_{mode}), the local soft X-ray fluctuation profile induced by an instability can be obtained.

One typical example obtained by using the above procedure is shown in Fig 2.6. In this case, the radial profile of measured soft X-ray emission agrees quite well with the calculated one not only for the shape but also for the phase difference among different channels. This best-fitted result of the simulation result is obtained from the scanning the mode width and the mode location, as seen from the Fig 2.7, indicating the mode locates at the $r/a \sim 0.51$ with the mode width $w_{mode} \sim 0.08a$ and the poloidal mode number is $m = 2$. The equilibrium in this shot calculated by VMEC (Hirshman and Whitson, 1983) taking account of the finite plasma β effect shows the $\iota = 0.5$ for $r/a \sim 0.51$, suggesting the mode is the $m = 2/n = 1$ mode. Note that, this is consistent with both the poloidal mode number $m = 2$ derived from the soft X-ray system and the mode number derived from magnetic probe arrays as $m = 2/n = 1$. The derived best-fitted mode eigenfunction is depicted in Fig 2.8.

2.2 Short reviews for other main diagnostics employed in the EIC study

2.2.1 Neutral particle analyzer (NPA)

The neutrals arise from atoms or molecules released from the first wall of the vacuum vessel and divertor target plates. At the plasma edge region very close to the wall, hydrogen molecule is dissociated as,



The birth of these neutrals with a few eV is isotropic and neutral density in the plasma core region is quite low because they are easily ionized by electrons near the plasma edge or ionized by charge-exchange process with ions. Very small amount of neutrals can exist in hot and dense core plasma region due to the multiple charge-exchange processes. Accordingly, the neutral hydrogen atom density is strongly localized very near the plasma edge, i.e., it has an extremely hollow profile. Charge exchange neutral flux dominantly generated in plasma edge region can be detected by a neutral particle analyzer (NPA) and some of them will penetrate into center of the plasma. These neutrals will undergo charge-exchange reactions with plasma ions and produce a new neutral and again the birth of the secondary neutral is isotropic. That is, some escape from the plasma and some moves radially inward with a further charge-exchange reaction. By this means, a low density hydrogen atoms can penetrate the whole plasma, with a quite hollow profile. On the other hand, the neutrals, which escape from the plasma freely, can be detected by a neutral particle analyzer. For a plasma satisfying the Maxwellian distribution function, the source function for the distribution of the escaping flux is,

$$S(E_0) = n_0 n_i \langle \sigma_0 v_i \rangle f_i(v_i) = n_0 n_i \langle \sigma_0 v_i \rangle \frac{2E_0^{1/2}}{\pi^{1/2} T_i^{3/2}} e^{-E_0/T_i}, \quad (2.14)$$

where E_0 is the energy of the neutrals. Therefore, measurement of the energy spectrum of the neutrals can determine the ion temperature especially in the low energy range.

NPA can also provide the valuable information on the energy distribution of the energetic ions, when the auxiliary heating such as NBI and ICRF is carried out. The energy distribution function is very important to study the confined energetic ion, especially when the EP-driven MHD instability occurs. In the EIC study, two types of the NPA is employed to provide the information of the confined helically trapped energetic ions. First, a compact NPA (CNPA)

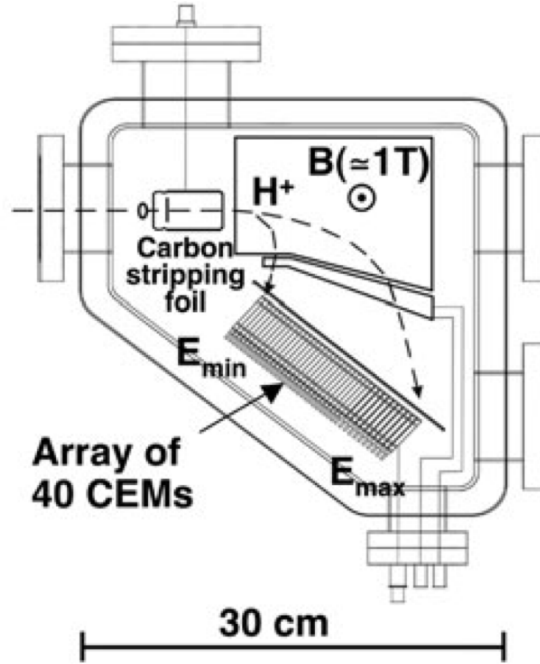


Fig. 2.9 The schematic plot of the CNPA system in LHD. (Goncharov et al., 2006)

viewing nearly perpendicular to the magnetic field line is used to detect the charge exchanged energetic neutrals up to 150keV escaped from the main plasma (Goncharov et al., 2006). The CNPA differs from the conventional NPA system by replacing the gas-filled stripping cell with the a thin diamond-like foil of 5nm thickness. The schematic plot for the system is shown in Fig. 2.9. Such concept of the compact NPA is developed in Ioffe Physicotechnical Institute in Russia.

In this study, the solid-state NPA (ssNPA) is also employed. The solid state NPA is based on the silicon photo-diode with different filter thickness to obtain the fast time resolution and coarse energy resolution. A charge-exchanged fast neutral particle incident into the sensitive layer of the detector element produces electron-hole pairs proportional to the energy of incident particle. These charges are drawn by an externally applied bias DC voltage to the electrodes. Compared with the conventional NPA or the compact NPA, the SSNPA system is quite small volume without complicated stripping cell or the large magnets and it can even work under the high magnetic field strength condition. However, the lower bound of the energy strongly depends on the the thickness of the filter and therefore it cannot be used for the purpose of the measurement of ion temperature. Instead, the SSNPA is powerful to study the charge-exchanged energetic neutral from escaped from the confinement region by the EP-driven instability. In LHD, the silicon diodes (SiFNA) viewing nearly perpendicular to

the LHD plasma are used as detectors of the SSNPA. The arrangements is shown in Fig. 2.10

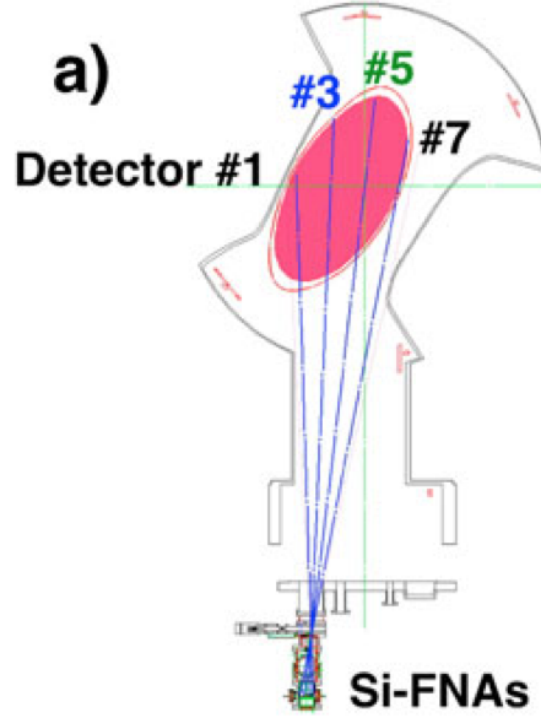


Fig. 2.10 The arrangements of the SSNPA system in LHD (Isobe et al., 2010).

2.2.2 Charge exchange recombination spectroscopy

The injection of energetic neutrals (hydrogen) by the NBI provide the great opportunities to diagnose the local plasma parameter. For example, the radiation is produced as a result of excitation of the beam and also following charge exchange reactions between the beam neutrals and plasma ions. If such radiation is observed at an non-zero arbitrary angle to the beam direction. the local plasma parameter can be acquired.

A typical reaction of interest is given,



After the reaction, the electron received by the C^{5+} in a state with a high principal quantum number and will decay with the emission of visible radiation. The spectra of this C^{6+} is at $\lambda = 529.05nm$. The line emission by charge-exchanged process between C^{6+} ions and edge

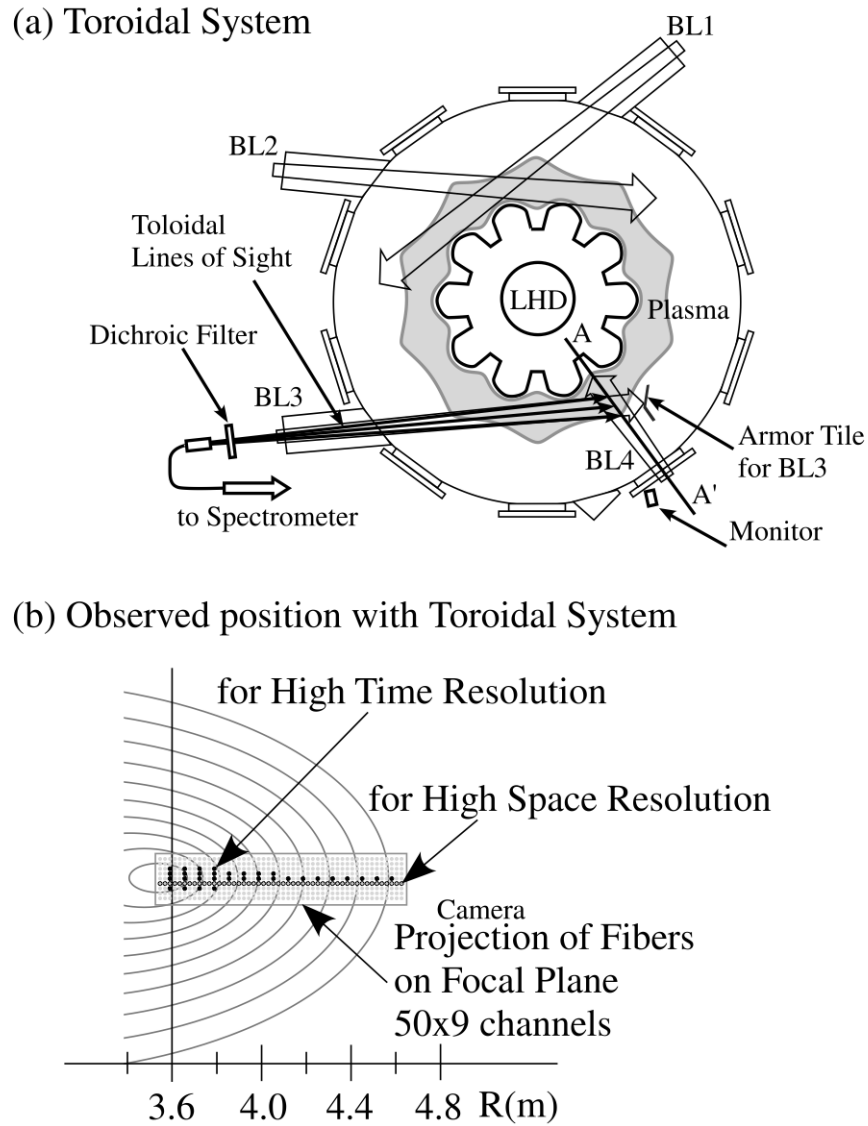


Fig. 2.11 Schematic views of CXS systems on LHD. (a) Top view of LHD and the toroidal lines of sight. (b) Projected position of the fibers on focal plane for toroidal lines of sight. (Yoshinuma et al., 2010)

neutral becomes large noise and it is suppressed by the injected energetic beam. The impurity ion temperature and flow velocity can be extracted from the parameters of a Gaussian function fitted to the Doppler broadened and shifted line at $\lambda = 529.05\text{nm}$, when assuming the impurity ion is under the Maxwellian distribution function. One typical example of the emission spectrum of charge exchanged spectrum of C^{6+} measured by the fast CXS system in LHD is shown in Fig. 2.12 (Yoshinuma et al., 2010). Note that the background emission

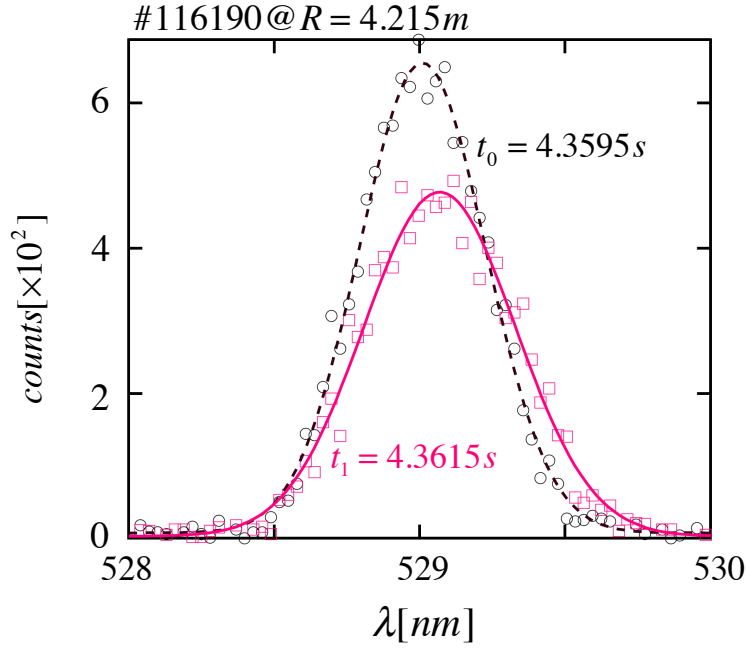


Fig. 2.12 The measured charge exchanged spectra at two time slices by the CXS system in LHD.

form the line-integrated effect of the sightline and also other beam line is eliminated by the modulation of the beam line 4, as graphed in Fig. 2.11.

2.2.3 Heavy ion beam probe

If the gyro-radius of minority ions can be comparable with the minor radius of the torus device, the ions move on an orbit with their gyro-radius ρ_i , i.e primary ions, until at some region in the plasma they become further ionized due to the collisions with plasma electrons. The further ionized ions move on an orbit with smaller radius at $\rho_i/2$. The energy difference between the primary ions and secondary ionized ions are as followings,

For primary ions,

$$E_{f1} = E_i + q(\phi_b - \phi_b) = E_i, \quad (2.16)$$

For secondary ions,

$$E_{f2} = E_i + q(\phi_I - \phi_b) + 2q(\phi_b - \phi_I) = E_i + q(\phi_I - \phi_b), \quad (2.17)$$

where ϕ_b is the plasma potential at the plasma boundary and Φ_I is the plasma potential at the interaction zone of the beam ions and the bulk plasma, where the beam ions is ionized further. Therefore,

$$\Delta E = E_{f2} - E_{f1} = q(\phi_I - \phi_b) \quad (2.18)$$

The secondary beam ions which is ionized in the interaction zone bring the potential information at the place where it is ionized out, if we analyze the energy of the secondary of the beam ions.

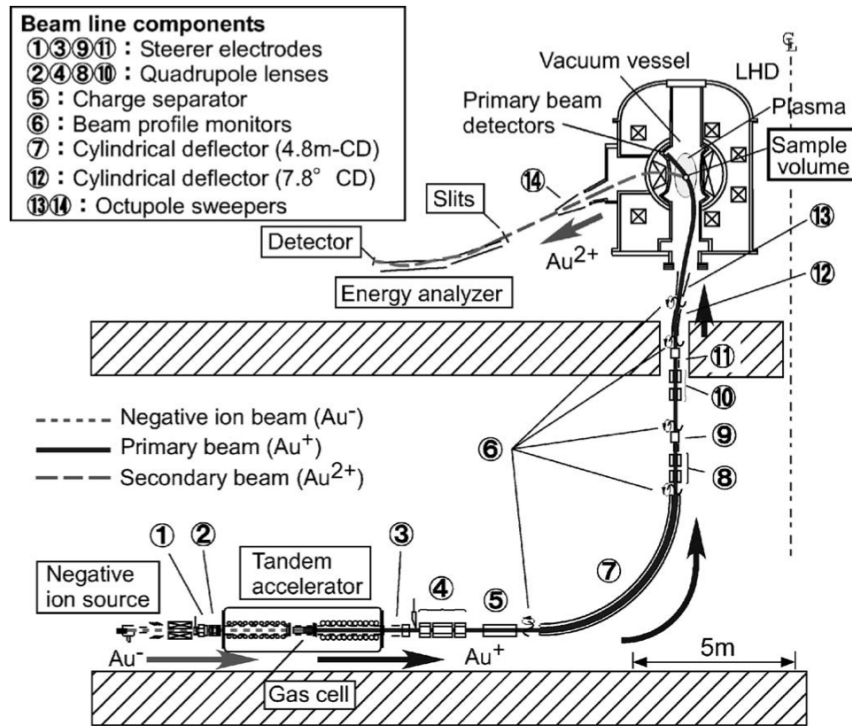


Fig. 2.13 Beam line of HIBP in LHD. (Ido et al., 2006)

Moreover, the information of potential fluctuation $\tilde{\phi}$ can also be measured. If we keep the intensity of the beam to be constant, the intensity of the secondary beam will be proportional to the plasma electron density in the interaction zone and the density fluctuation \tilde{n}_e is also measured. The electron density that HIBP is applicable is limited to lower level in a plasma with the large minor radius, because of the large attenuation of the probe beam. In addition, the beams are shifted toroidally from the cross-section that the secondary beam is generated by the presence of the poloidal field. A measurement from the movements on the detectors from the neighboring ionization points can determine the amplitude of the B_θ and the

fluctuation too in an axisymmetric case such as a tokamak, because of the conservation of the toroidal canonical momentum of the probe beam ion. For the non-axisymmetric case such as a stellarator/helical plasma, they would be determined approximately.

2.3 Numerical Analysis methods for analysis of fluctuation signals

2.3.1 Fast Fourier Transform

Suppose $f(x)$ is absolutely integrable in $(+\infty, -\infty)$, then the Fourier transform of $f(x)$ is given by,

$$\mathcal{F}(k) = \int_{-\infty}^{+\infty} f(x) e^{-ikx} dx \quad (2.19)$$

The inversible Fourier transformer is given by,

$$f(x) = \frac{1}{2\pi} \int_{-\infty}^{+\infty} \mathcal{F}(k) e^{ikx} dk \quad (2.20)$$

In the real measurement, we have a discrete result as $a = (a_0, a_1, \dots, a_{N-1})$ and we define discrete Fourier transformer (DFT) of a as $c = (c_0, c_1, \dots, c_{N-1})$, yielding

$$c_k = \sum_{j=0}^{N-1} a_j e^{-jk \frac{2\pi i}{N}}, \quad k = 0, \dots, N-1 \quad (2.21)$$

The inversion of discrete Fourier transformer of c is defined as,

$$a_j = \frac{1}{N} \sum_{k=0}^{N-1} c_k e^{jk \frac{2\pi i}{N}}, \quad j = 0, \dots, N-1 \quad (2.22)$$

Here i is the imaginary unit and $\omega \equiv e^{-\frac{2\pi i}{N}}$. Therefore, the DFT can be considered as a linear transformation. The Fourier matrix can be defined by,

$$F = \begin{pmatrix} 1 & 1 & \dots & 1 \\ 1 & \omega & \dots & \omega^{N-1} \\ \dots & \dots & \dots & \dots \\ 1 & \omega^{N-1} & \dots & \omega^{(N-1)^2} \end{pmatrix} \quad (2.23)$$

Then,

$$\mathbf{c} = F\mathbf{a} \quad (2.24)$$

The inverse DFT can also be considered as a linear transformation. Define inverse Fourier matrix

$$F^{-1} = \begin{pmatrix} 1 & 1 & \cdots & 1 \\ 1 & \omega^{-1} & \cdots & \omega^{-(N-1)} \\ \cdots & \cdots & \cdots & \cdots \\ 1 & \omega^{-(N-1)} & \cdots & \omega^{-(N-1)^2} \end{pmatrix} \quad (2.25)$$

and

$$\mathbf{a} = F^{-1}\mathbf{c} \quad (2.26)$$

If we compute DFT directly, the N^2 multiplications and $N(N-1)$ additions are necessary. Here we consider one simple case for $N=4$, where $e^{-i\frac{\pi}{2}} = -i$ and

$$F = \begin{pmatrix} (-i)^0 & (-i)^0 & (-i)^0 & (-i)^0 \\ (-i)^0 & (-i)^1 & (-i)^2 & (-i)^3 \\ (-i)^0 & (-i)^2 & (-i)^4 & (-i)^6 \\ (-i)^0 & (-i)^3 & (-i)^6 & (-i)^9 \end{pmatrix} = \begin{pmatrix} 1 & 1 & 1 & 1 \\ 1 & -i & -1 & i \\ 1 & -1 & 1 & -1 \\ 1 & i & -1 & -i \end{pmatrix} \quad (2.27)$$

and therefore,

$$\mathbf{c} = F\mathbf{a} = \begin{pmatrix} (a_0 + a_2) + (a_1 + a_3) \\ (a_0 - a_2) - i(a_1 - a_3) \\ (a_0 + a_2) - (a_1 + a_3) \\ (a_0 - a_2) + i(a_1 - a_3) \end{pmatrix} \quad (2.28)$$

From the observation of the above equation, instead to calculate the 4^2 computation, we only need to calculate $a_0 + a_2$, $a_1 + a_3$, $a_0 - a_2$, and $a_1 - a_3$ and two multiplication, i.e. $4\log_2 4 = 8$. Therefore, the lengthy computation can be dramatically reduced by the so called fast Fourier method as,

$$\mathcal{O}(N^2) \rightarrow \mathcal{O}(N\log_2 N) \quad (2.29)$$

FFT method is very powerful method to analyze the fluctuations. The amplitude of the magnetic fluctuation of X can be expressed as,

$$P_{XX}(k) = \frac{1}{T} E[X^*(k)X(k)] \quad (2.30)$$

The cross power of the two fluctuation is useful to calculate the the cross-correlation or cross-covariance between two time series, given by

$$P_{XY}(k) = \frac{1}{T} E[X^*(k)Y(k)] \quad (2.31)$$

The cross-coherence is given by,

$$\gamma_{XY} = \frac{|P_{XY}(k)|}{\sqrt{P_{XX}(k)P_{YY}(k)}} \quad (2.32)$$

and the phase between two time series are given by,

$$\theta_{XY}(k) = \tan^{-1} \left(\frac{\text{Im}(P_{XY}(k))}{\text{Re}(P_{XY}(k))} \right) \quad (2.33)$$

Here one typical example to calculate the toroidal mode number by the FFT method is given in Fig. 2.14. The toroidal mode number can be estimated from the phase difference between each magnetic probe, which can be identified up to $n = 4$ from the 6 toroidal magnetic probes and the layout of the arrangements of the magnetic probes in LHD is also shown.

Furthermore, The spectrum of the toroidal mode number can also be calculated. The coherence between two different Mirnov Probes (MP) are calculated. If the coherence exceeds the 0.7, the coherent MHD instability is thought to be recognized. Then, at that specific mode frequency, the mode number can be estimated through the phase difference, as mentioned above. On typical example is shown in Fig. 2.15. In the spectrum, the MHD instabilities, having $m = 2/n = 1$, $m = 1/n = 1$, $m = 2/n = 3$ and $m = 2$ or $m = 3/n = 4$, are found to be destabilized in different frequency range.

2.3.2 Empirical mode decomposition method

Spectral analysis is synonymous with Fourier-based analysis. However, the well-known Fourier spectra can only give meaningful interpretation to linear and stationary processes. Application to data from nonlinear and non stationary processes is often problematical but the real time series signals, i.e. the bursting MHD instabilities, is usually nonlinear and non-stationary. The Hilbert-Huang transform (HHT) is a powerful method for nonlinear and non-

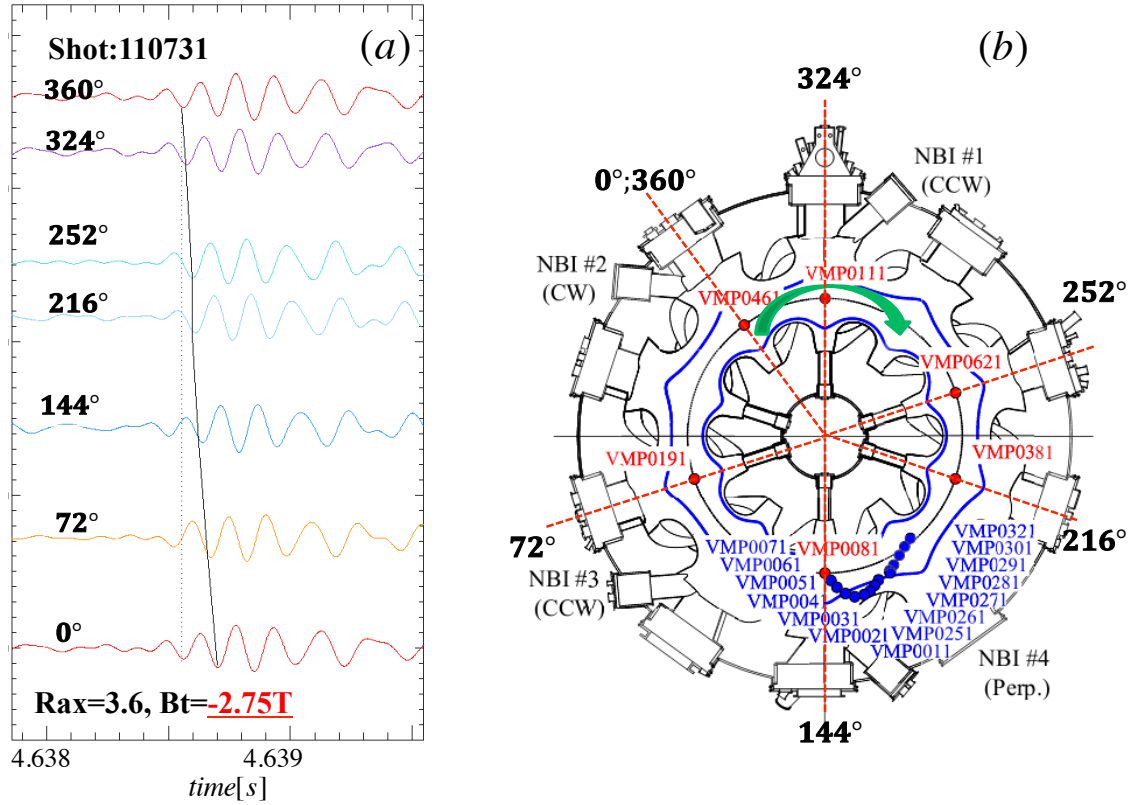


Fig. 2.14 The phase difference between the magnetic probes indicates the $n = 1$ mode is destabilized and the layout of the magnetic probes in LHD is also shown.

stationary vibrations analysis. This approach consists of two basic parts of empirical mode decomposition (EMD) and Hilbert spectral analysis (HSA). To analyze a multi component signal, it is essential to decompose the signal into mono component functions. Huang proposed the EMD method to extract mono-component functions from the nonlinear and non-stationary signals, which are known as the intrinsic mode functions (IMFs). An IMF is defined as a function that satisfies the following requirements:

1. In the whole data set, the number of extrema and the number of zero-crossings must either be equal or differ at most by one.
2. At any point, the mean value of the envelope defined by the local maxima and the envelope defined by the local minima is zero.

The procedure of extracting the IMFs is called sifting and the process of the sifting is as follows,

1. Identify all the local extrema in the data of $x(t)$.

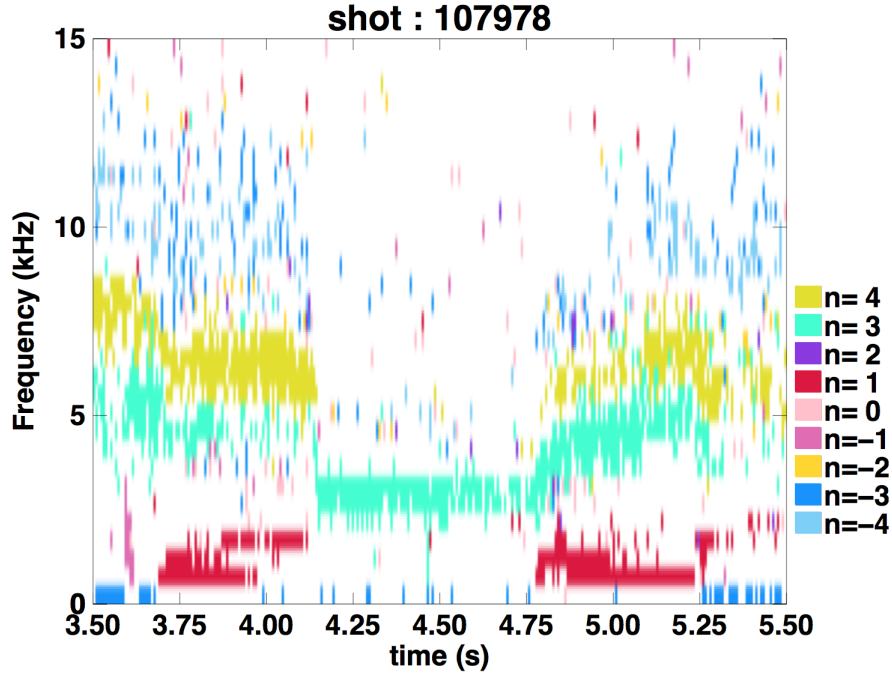


Fig. 2.15 Cross Coherence frequency spectrum between the toroidal Mirnov probes is shown. The $m=2/n=1$, $m=1/n=1$, $m=2/n=3$ and $m=2$ or $3/n=4$ are destabilized.

2. Connect all the local maxima by a cubic spline line as the upper envelope, i.e. $e_{max}(t)$.
3. Repeat the procedure for the local minima to produce the lower envelope, i.e. $e_{min}(t)$.
4. The mean value of the upper and lower cubit lines are the $m(t) = (e_{max}(t) + e_{min}(t)) / 2$ and the difference between the mean value and the raw data is treated as the detail of $d(t) = X(t) - m_1$.

(Note that if the IMF criterion is satisfied (zero mean value) for the $d(t)$, it is marked as the first IMF function $c_1(t)$. If not, the first iterating steps 1 to 4 upon the detail signal $d(t)$ should be conducted, until this latter can be considered as zero-mean according to some stopping criterion. Once this is achieved, the detail is referred to as an Intrinsic Mode Function (IMF), the corresponding residual is computed and step 5 applies.)

5. Iterate on the residual $r_1(t) = x_1(t) - c_1(t)$.
6. Finally, when the residue $r_n(t)$ is the non-vibration mono-function or the constant, the decomposition process is completed and the function $x(t)$ can be written as,
$$x(t) = \sum_{i=1}^n c_i(t) + r_n(t).$$
 A flow chart to show the above sifting process (decomposition procedure) is shown in Fig. 2.17.

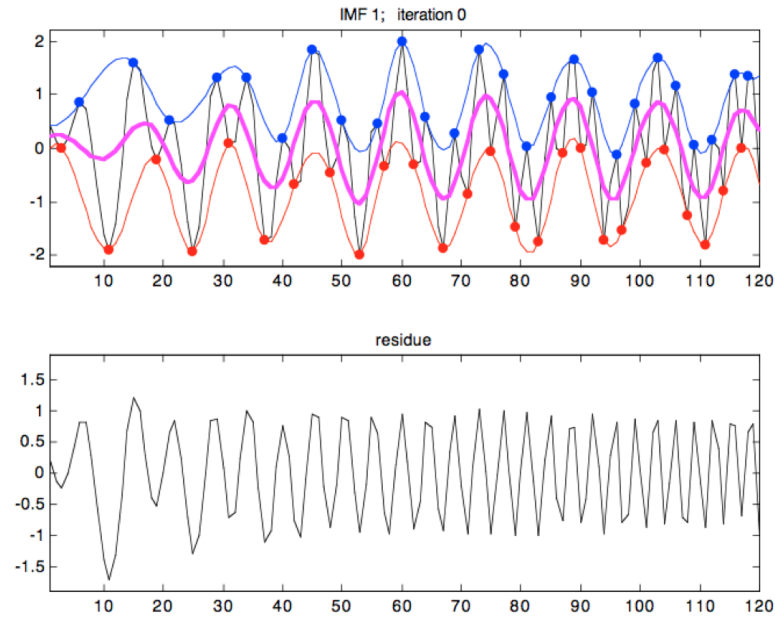


Fig. 2.16 The process of the sifting. (Huang and Wu, 2008)

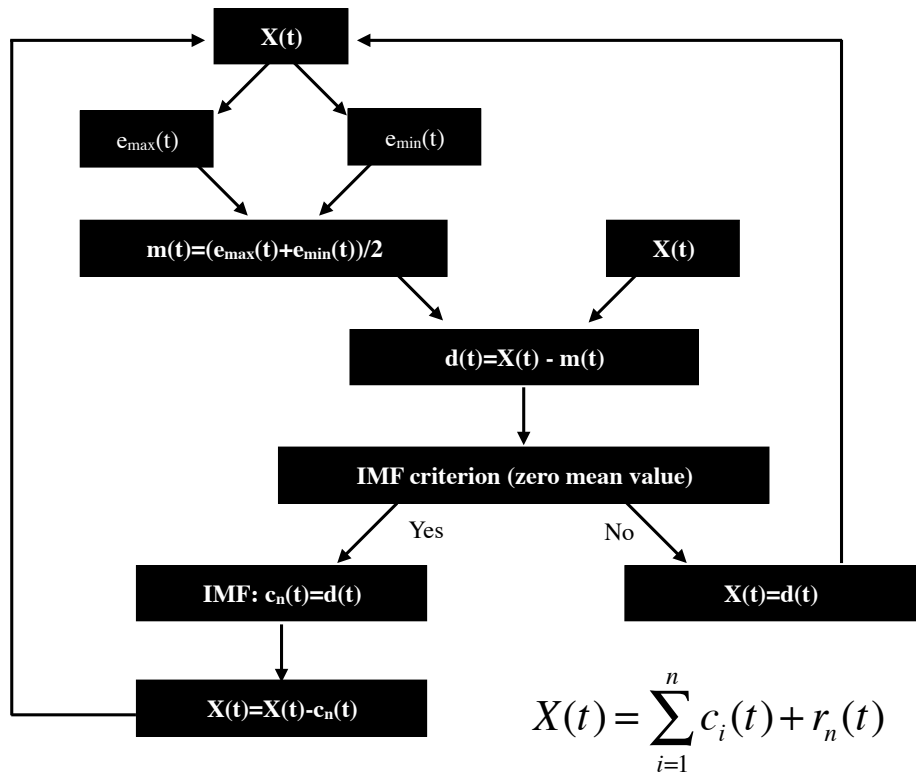


Fig. 2.17 The flow chart of the sifting process.

The typical example for using the EMD method to analyze the EIC mode is given. The ECE channels are decomposed here into several intrinsic mode functions and the magnetic probe signal is plotted together. It is found that on intrinsic mode function in the channel measure the $r/a \sim 0.86$ strongly correlates with the fluctuation in the magnetic probe, indicated by the reference channel in Fig. 2.18 [between the dashed line].

The radial profile of the fluctuations at the each crest and trough of the reference channel in this time window can be graphed, shown in Fig 2.19. A beautiful interchange type odd function is derived from the EMD method. The conditioning average for the crest and trough, respectively, are also given together.

Here we also include the mode structure derived by the traditional FFT method to compare with the result derived by this novel EMD. The radial profile of the electron temperature fluctuation can be given by,

$$\tilde{T}_e(\rho) = \gamma^2(\rho) \frac{1}{T} E[X(k)X^*(k)], \quad (2.34)$$

where γ is the cross-coherence between the each ECE channels with the magnetic probe signal. The result is shown in Fig. 2.20. The radial profile of the temperature fluctuation derived from the FFT and the EMD is quite similar with each other. It should be noted that FFT method is averaged over a wide time window from 4.2s to 5.0s. Comparably, the EMD method can handle the rapid change of the mode eigenfunction in a short time window and even for a transient event in principle. Therefore, EMD method together with the conditioning average is a very powerful tool to study the bursting MHD event, for which the frequency and amplitude of the oscillation may rapidly change and the wave pattern might be far away from the sinusoidal oscillations.

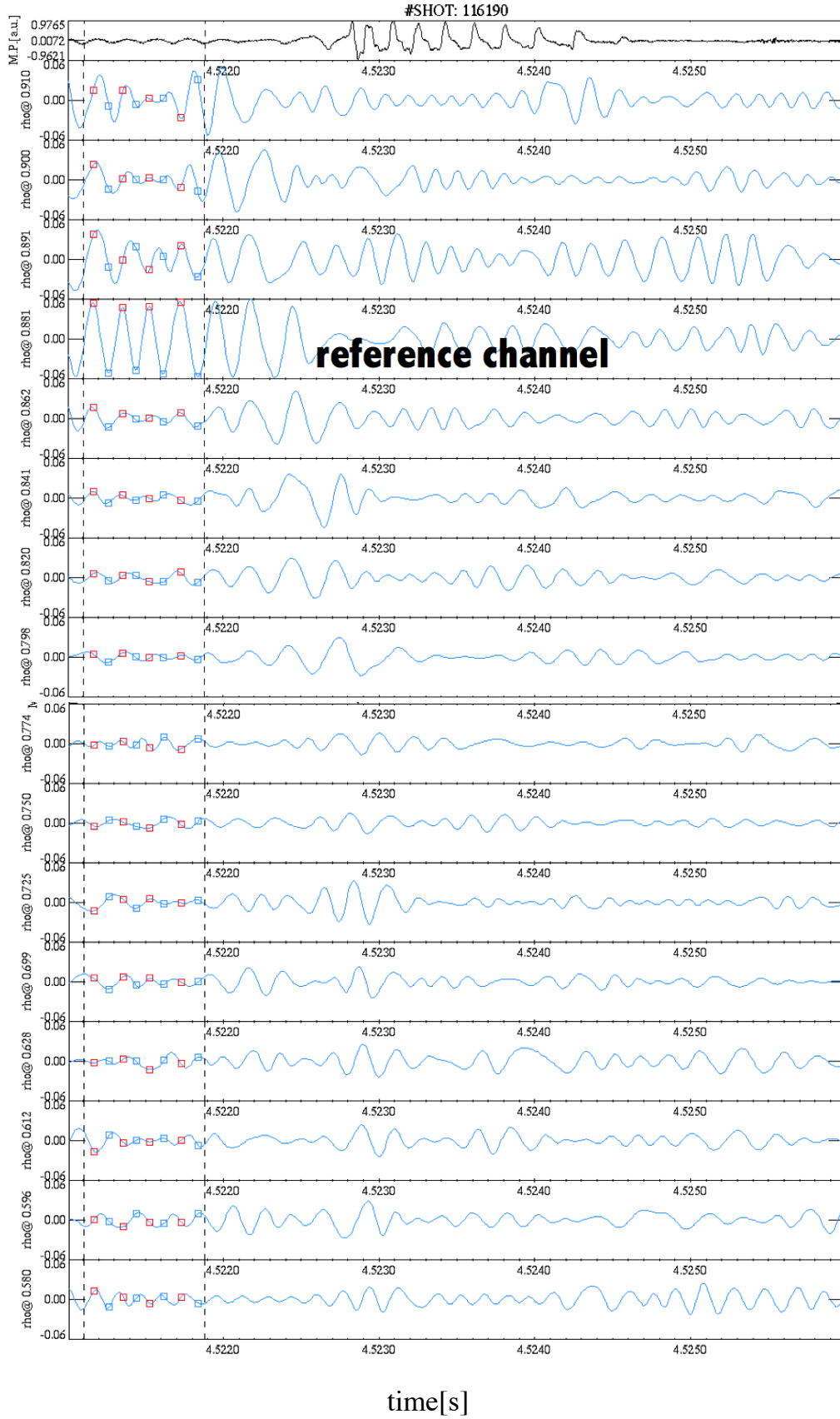


Fig. 2.18 One example for the EMD method on the electron temperature fluctuation \tilde{T}_e induced by resistive interchange mode by ECE.

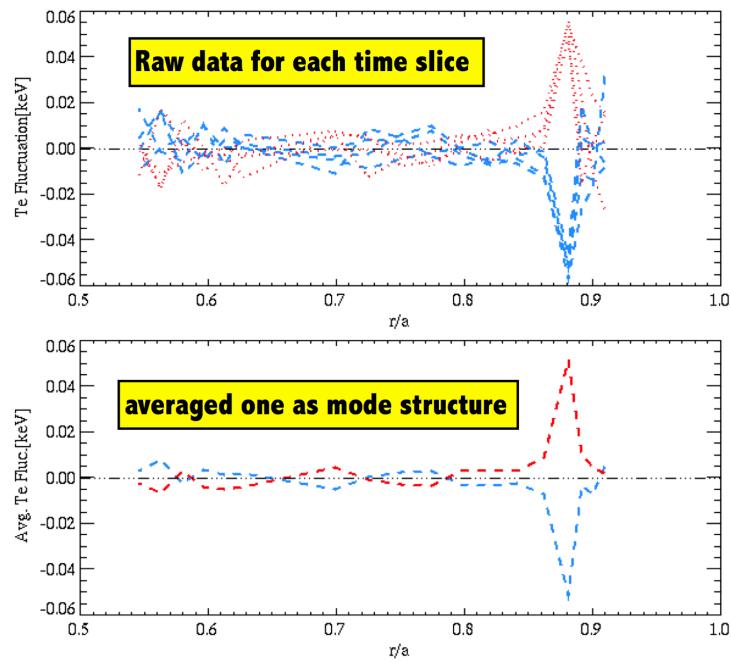


Fig. 2.19 Upper: the radial profile of electron temperature fluctuation \tilde{T}_e derived by the EMD method. Lower: the radial profile of electron temperature fluctuation \tilde{T}_e calculated by the conditioning average.

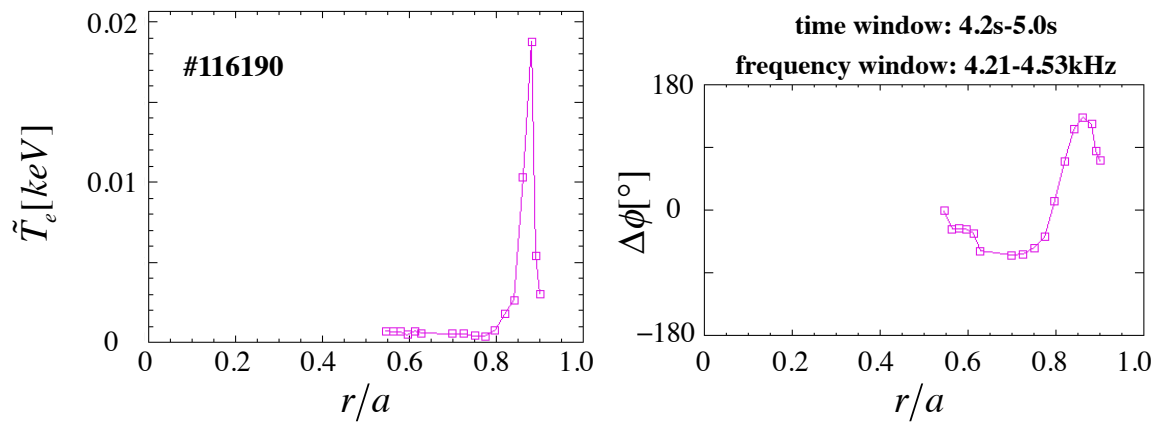


Fig. 2.20 Left: the radial profile of electron temperature fluctuation \tilde{T}_e derived by FFT method. Right: the radial profile of phase difference of \tilde{T}_e between each ECE channel derived by FFT method.

Chapter 3

Identification of the EIC in LHD

3.1 Destabilization of EIC in LHD experiment

The resistive interchange mode (RIC) is destabilized by finite pressure gradient in magnetic hill and it can be excited even below the beta limit predicted by the Mercier criterion when the magnetic shear stabilization effect disappears due to the effect of resistivity. In recent years, the RIC has been studied experimentally for H-mode plasmas with steep pressure gradient near the edge in the Large Helical Device (LHD) (Toi et al., 2004, 2005), as the magnetic hill exists in the peripheral region (Watanabe et al., 2010). It is found that the RIC localizes at the mode rational surface, having an even function (Gaussian type) with fairly narrow width (Watanabe et al., 2007, 2006a, 2011), consistent with the prediction from a linear resistive MHD theory (Ueda et al., 2014). Furthermore, a recent numerical study on solving an eigenvalue problem of the RIC has unveiled the existence of an island type eigenmode having a comparable linear growth rate with that of the largest-growth-rate eigenmode (i.e., the usual Gaussian-type interchange eigenmode) (Ueda et al., 2014). According to the linear resistive MHD theory, the growth rate of the RIC is predicted as (Carreras et al., 1987), where λ , κ , and ℓ_s are the scale length of the pressure gradient, the flux-surface-averaged magnetic curvature, electrical resistivity and the magnetic shear length at the rational surface, respectively. Moreover, the nonlinear saturation level of the RIC may increase with the plasma beta value (β =plasma pressure/toroidal magnetic pressure) and decrease with the magnetic Reynolds number ($\propto 1/\eta$), as similar to the tendency of the linear growth rate. Actually, experimental results in LHD support the above predictions (Sakakibara et al., 2008). Moreover, in DIII-D tokamak a bursting mode identified as the RIC is observed in the negative central shear discharge with high-normalized beta β_N , having a localized mode structure similar to the RIC (Chu et al., 1996; Jayakumar et al., 2002). A local flattening of the safety factor, toroidal rotation and pressure profiles at the mode

rational surface in the negative shear region is induced by the RIC. A coupling of the RIC and tearing/kink mode often triggers a major disruption.

In this thesis, we focus on the first observation of a bursting RIC destabilized by resonant interaction with helically trapped energetic ions (EPs) in LHD, named as the helically trapped energetic-ion-driven resistive interchange mode, or ‘EIC’. The EICs have recently been observed in the low frequency range ($f < 10\text{kHz}$) with rapid frequency chirping-down in low β plasmas ($\beta < 1\%$) where hydrogen neutral beam injection nearly perpendicular to magnetic field line (PERP-NBI) is applied (Du et al., 2015). The mode has $m = 1/n = 1$, where m and n are poloidal and toroidal mode numbers respectively and localizes at the mode rational surface in the peripheral region of current-free plasma. The eigenfunction shows a similar shape with the predicted eigenfunction of the RIC, which is clearly distinguished from the EP-driven internal kink mode in tokamak well known as ‘fishbone’ (Matsunaga et al., 2009) or EP-driven external kink mode, so called EP-driven wall mode in JT-60U (Okabayashi et al., 2011) or off-axis fishbone in DIII-D (Heidbrink et al., 2011; Okabayashi et al., 2011). In the peripheral region of the LHD plasma, the helical field ripple is large, i.e., $\varepsilon_h \sim 0.2$. Consequently, energetic ions generated by PERP-NBI are deeply trapped in the helical ripple, called ‘helically trapped energetic ions’ (Watanabe et al., 2006b). The EIC bursts strongly enhance radial transport of the trapped energetic ions. They also have transient but significant effects on the bulk plasma through losses and radial redistribution of helically trapped energetic ions induced by the EIC, that is, a large change of toroidal rotation, clear suppression of micro-turbulence near the mode rational surface and transient improvement of bulk plasma confinement. Although the observed confinement improvement triggered by the EIC in LHD is still transient so far, the underlying physics is thought to be similar to that in other similar confinement improvement events triggered by EP-driven modes such as fishbone and TAE bursts (Günter et al., 2002; Toi et al., 2011). The physics mechanisms are expected to work effectively in future burning plasmas where some EP-driven modes might be destabilized.

3.1.1 The EIC in so-called high T_i discharge

LHD is a helical device with a pair of superconducting helical coils, having non-axisymmetric three-dimensional magnetic configuration. The EIC is mainly investigated in NBI-heated plasmas of the magnetic configuration of $R_{ax} = 3.6\text{m}$, $\gamma = 1.254$ and $B_q = 100\%$ at the toroidal field strength $B_t = -2.85\text{T}$, where R_{ax} is the magnetic axis position of the vacuum field, γ is the pitch parameter of the helical coil (a_C/R_C) / (N/l) (R_C and a_C : the major and minor radii of the helical coil winding respectively; N and l : the toroidal and poloidal pole numbers of the helical coil) and γ is the quadrupole field components of the poloidal

coils normalized by that of the helical coils (Watanabe et al., 2010). The negative sign of B_t is defined to be in the counter clockwise direction. The averaged minor radius of the configuration is $a = 0.64m$. Three neutral hydrogen beam lines with negative ion sources of beam energy up to $180keV$ are injected nearly parallel to the magnetic axis (TANG-NBI), and the other two beam lines with positive ion sources of $E_b = 34keV$ are injected nearly perpendicular to the magnetic axis. The plane view of the NBI arrangements is depicted in Fig. 3.1 and the locations of main plasma diagnostics employed in the EIC studies are also graphed together.

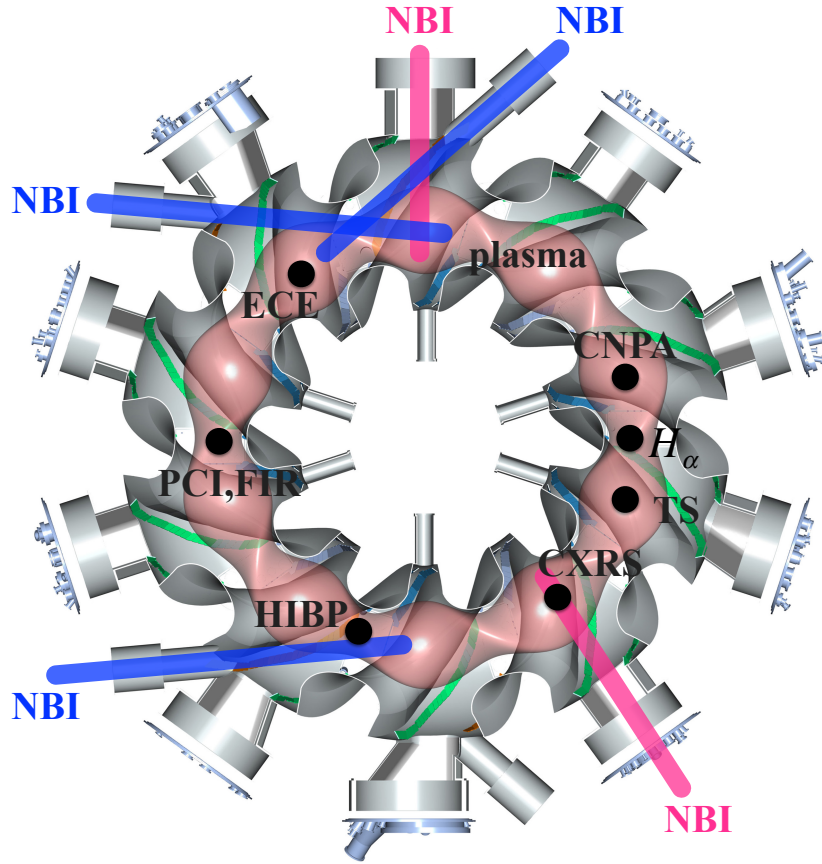


Fig. 3.1 Arrangements of tangential and perpendicular NBI beamlines and main plasma diagnostics employed in EIC studies.

As shown in Fig. 3.2, the EICs are often observed in relatively low-density plasmas so-called high-Ti discharges (Nagaoka et al., 2011) with high power injections of both PERP-NBI and TANG-NBI of absorbed power of total $6MW$. The electron temperature T_{e0} and density n_{e0} typically have parabolic radial profiles, of which central values reach $T_{e0} \sim 3.5keV$ and $n_{e0} \sim 0.8 \times 10^{19}m^{-3}$, respectively. The volume-averaged toroidal beta

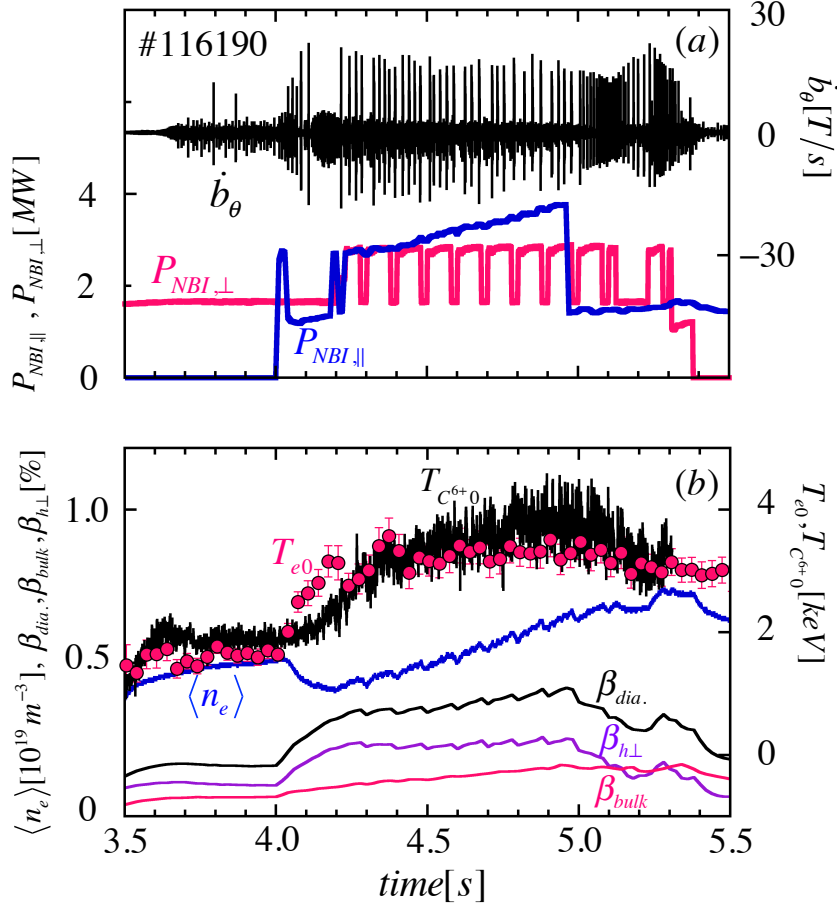


Fig. 3.2 (a) Temporal evolutions of magnetic fluctuations measured by a magnetic probe signal (\dot{b}_θ) and absorbed powers of TANG-NBI ($P_{NBI,\parallel}$) and PERP-NBI ($P_{NBI,\perp}$). (b) Temporal evolutions of the central electron temperature (T_{e0}), central ion temperature ($T_{C^{6+0}}$), line-averaged electron density ($\langle n_e \rangle$) and volume-averaged bulk plasma beta (β_{dia}) derived from Thomson scattering diagnostics (β_{bulk}) and volume-averaged beam beta perpendicular to magnetic field line ($\beta_{h\perp}$) derived from a diamagnetic loop as $\beta_{h\perp} = \beta_{dia} - \beta_{bulk}$.

of bulk plasma β_{bulk} , evaluated from the YAG-laser Thomson Scattering system (Narihara et al., 2001) on the assumption that the electron and ion pressures are nearly the same, is fairly low due to the low electron density and high toroidal magnetic field strength. The volume-averaged beam beta perpendicular to magnetic field line $\beta_{h\perp}$ is comparable with β_{bulk} due to large slowing down time of helically trapped energetic ions. The $\beta_{h\perp}$ is estimated as $\beta_{h\perp} = \beta_{dia} - \beta_{bulk}$, where the diamagnetic beta β_{dia} is obtained by a diamagnetic loop. It should be noted that is dominated by the contribution from helically trapped EPs because that

from passing EPs can be neglected. As seen from Fig. 3.2(a), magnetic fluctuations of the EIC measured by a magnetic probe exhibit fishbone-shape oscillations, when $\beta_{h\perp}$ is large.

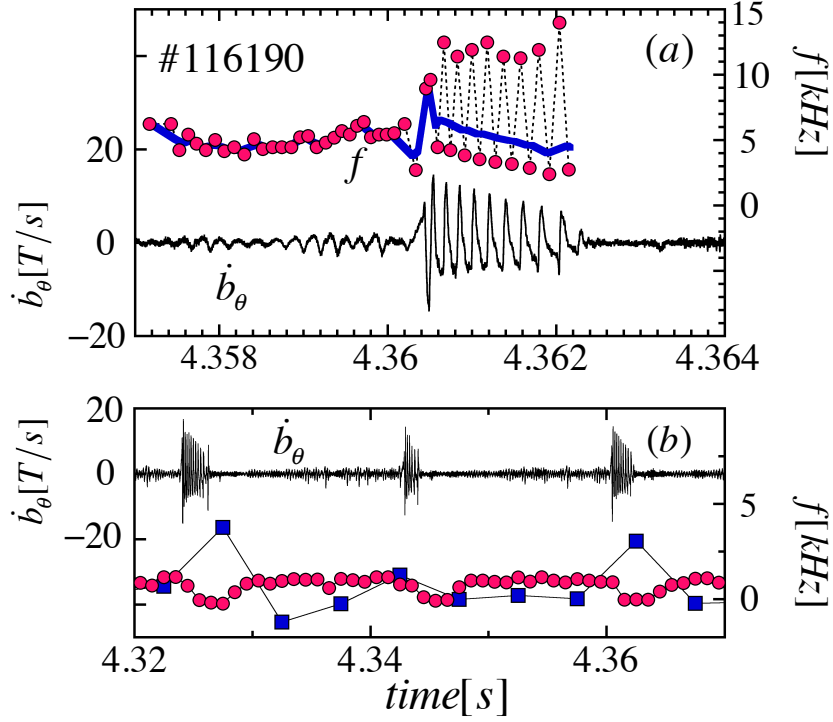


Fig. 3.3 (a) Time evolution of the magnetic probe signal (\dot{b}_θ) and the temporal frequency (f) calculated by each half period of EIC (solid circle) and full period (line) for a typical EIC. (b) Magnetic probe signal (\dot{b}_θ) with three EICs and the Doppler frequencies evaluated from poloidal (squares) and toroidal (circles) rotation velocities measured by CXRS at $t = 1$ location.

The typical expanded waveform is shown in Fig. 3.3(a). A weak sinusoidal oscillation of $\sim 5\text{kHz}$ is observed from 4.357s to 4.36s, and grows rapidly in $\sim 0.2\text{ms}$ before the onset of an EIC burst. This oscillatory mode is thought to be a usual pressure-driven RIC. It suddenly evolves into the EIC having large amplitude and strongly distorted waveform. Here, the temporal frequency of the EIC is evaluated from each half period. The frequency from the trough to the crest is much larger than the one from the crest to trough in one period of oscillation, suggesting the strong distortion away from the sinusoidal oscillations. The frequency is also evaluated from one full period of oscillation, showing a characteristic of rapid chirping-down from 8.5kHz to 3.5kHz in 2ms, accompanied with a gradual decay of the amplitude of magnetic fluctuations. Then, magnetic fluctuations disappear for a few ms just after the EIC burst. In addition, the Doppler frequencies arising from bulk plasma rotations in the poloidal and toroidal directions are evaluated from the rotations of ions

measured by charge exchange spectroscopy (CXRS) (Yoshinuma et al., 2010). As seen from Fig. 3.3(b), the contribution from the Doppler frequencies to the observed frequency of the EIC is considerably small because the non-axisymmetric magnetic field structure brings about large parallel viscosity and strongly slows down the toroidal and poloidal flows in peripheral region of LHD plasma (Shaing, K.C. and Callen, 1983). In other words, the EIC as well as the RIC do have the real frequency itself in the plasma frame. Moreover, according to the phase analysis of magnetic probe arrays, both the RIC and the EIC with $m = 1/n = 1$ mode structure propagate in the electron diamagnetic drift direction poloidally and counter- B_t direction toroidally in the plasma frame, respectively. This is the same propagation direction of the usual pressure-driven RIC observed in various LHD plasmas (Takemura et al., 2013).

3.1.2 Destabilization of the EIC only by PERP-NBI

A specific experiment is conducted to destabilize the EIC by only PERP-NBI of initial beam energy $E_b \sim 34keV$, without any TANG-NBIs, shown in Fig. 3.4. In this experiment, electron cyclotron heating (ECH) with $77GHz$ is employed to maintain the plasma performance throughout the discharge. One PERP-NBI of $\sim 1.6MW$ deposition power is applied with full power modulation throughout the discharge and the other PERP-NBI of $\sim 1.6MW$ is superimposed during the short time window from $t = 4.0s$ to $4.18s$, as shown in Fig. 3.4(d). Oscillatory mode destabilized weakly is observed in magnetic probes in the time interval from $t = 4.0s$ to $4.18s$ where two PERP-NBIs are overlapped, as shown in Fig. 3.4(b). The destabilization of the oscillatory mode is caused by the increase of β_{dia} . In the latter half of the time interval, strong bursting events are detected in magnetic probes. As seen from the expanded view in Fig. 3.4(a), the oscillatory mode of $\sim 2kHz$ is firstly destabilized. Then, the magnetic fluctuation amplitude is suddenly enhanced with strongly distorted waveforms instead of sinusoidal oscillations, similar to the EICs observed in the so-called high-Ti discharge shown in Figs. 3.2 and 3.3. An important point is that the mode frequency suddenly jumps up to $8kHz$, and then rapidly chirps down to $2kHz$ in $\sim 2ms$. The Doppler frequency evaluated from the carbon toroidal flow measurement by CXRS is significantly small compared with the EIC mode frequency especially on the condition without the toroidal momentum input by TANG-NBI. In the low power phase of PERP-NBI after $t \sim 4.18s$, the bursting mode is no longer destabilized, as seen from Fig. 3.2(b). Note that two tiny tips of this phase in the probe signal are pick-ups due to PERP-NBI switch-off. This suggests that the EIC can be destabilized only by a large amount of helically trapped energetic ions produced with intense PERP-NBI. The threshold for the amount of the trapped energetic ions is discussed in the sub-section (2.3).

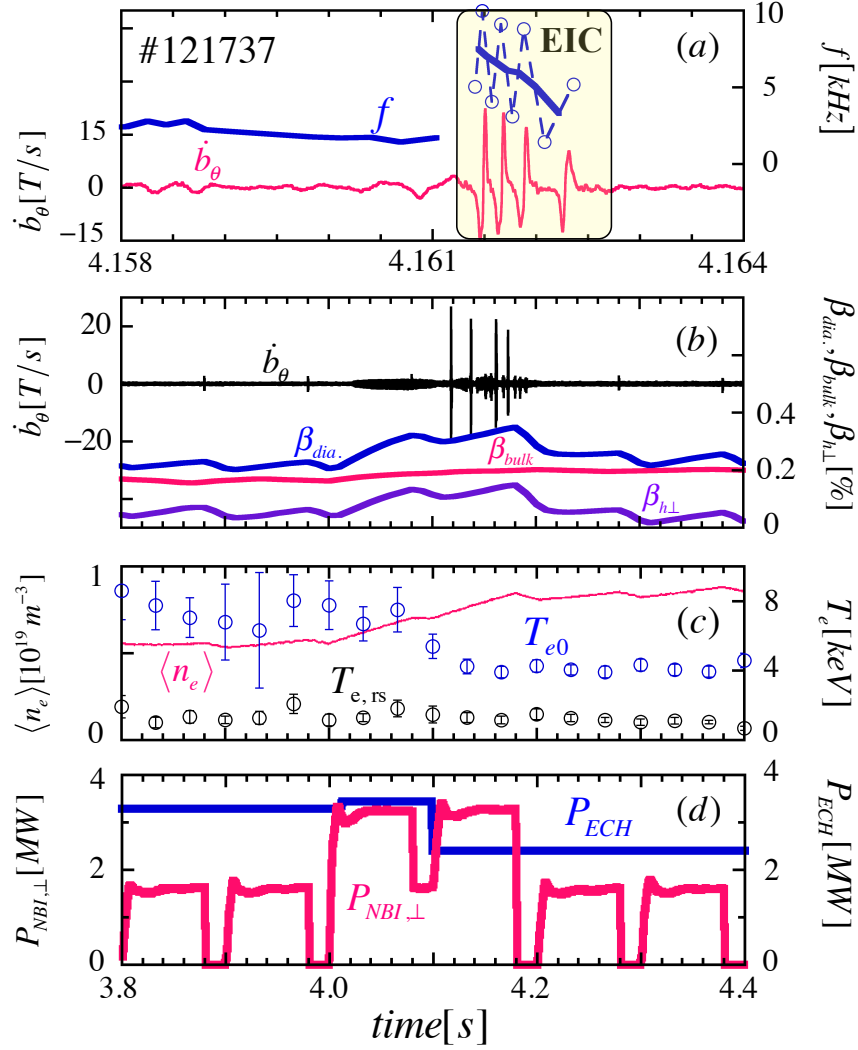


Fig. 3.4 (a) An expanded view of magnetic probe signal (\dot{b}_θ) and its frequency. (b) Time evolutions of \dot{b}_θ and volume-averaged bulk plasma beta (β_{bulk}) derived from Thomson scattering diagnostics and volume-averaged beam beta perpendicular to magnetic field line ($\beta_{h\perp}$) derived from a diamagnetic loop as $\beta_{dia.}$, (c) electron temperature at the plasma center (T_{e0}) and that at $t = 1$ surface ($T_{e,rs}$) measured by Thomson scattering diagnostics together with the line-averaged electron density $\langle n_e \rangle$, and (d) absorbed power of ECH (P_{ECH}) and that of PERP-NBI ($P_{NBI,\perp}$).

3.2 Trajectories of helically trapped energetic ions in LHD

To investigate the resonant interaction between the RIC and energetic ions, the orbit of helically trapped energetic ions produced by PERP-NBI is investigated numerically by a full orbit code called ‘LORBIT’ (Isobe et al., 1999). One typical example is depicted in Figs. 3.5(a) and (b), where a proton with energy $E_b \sim 34keV$ and pitch angle $\chi \sim 85^\circ$ is launched from the top location ($\theta \sim \pi/2$) of a helical ripple valley on the $\iota = 1$ flux surface and tracked numerically. Note that there are two magnetic valleys existing in LHD due to the existence of a pair of helical coils. It can be seen that the proton makes a bounce motion and is deeply trapped in the helical ripple valley. Simultaneously, it also circulates helically around the torus with the helical pattern of $\cos(l\theta - N\phi)$ in the ion diamagnetic drift direction poloidally and in the counter- B_t direction toroidally, being trapped in the magnetic valley where the magnetic field is weak ($l = 2$: polarity of helical field, $N = 10$: toroidal field number). The toroidal and poloidal precession frequencies of helically trapped ions are calculated by scanning the radial launching position of the test proton from the normalized minor radius $r/a \sim 0.5$ to 1.0 . The results are summarized in Fig. 3.5(c). From the calculation results, the absolute value of the poloidal precession frequency increases radially from $3kHz$ at $r/a \sim 0.5$ to $12kHz$ at the plasma boundary ($r/a \sim 1$) and toroidal precession frequency is found to be $f_{tor}^{prec} = (l/N)f_{pol}^{prec}$, as expected, due to the topology of the magnetic field. The negative sign of the precession frequencies stands for the ion diamagnetic drift direction poloidally and counter- direction toroidally.

3.3 Resonance Condition

The resonance condition for a heliotron/stellarator plasma is given by the reference (Kolesnichenko et al., 2002),

$$f_{MHD} - (m + j\mu)\langle f_{pol}^{prec} \rangle + (n + j\nu)\langle f_{tor}^{prec} \rangle = 0 \quad (3.1)$$

where $j = 0, 1$. The bracket $\langle \dots \rangle$ means the flux-surface-average. Here, the precession motions in the magnetic field structure are decomposed by the Fourier components $[\mu, \nu]$. The resonance frequencies for the EIC are calculated by substituting the precession frequencies of the helically trapped energetic ions at the mode rational surface. The observed frequency of the EIC is consistent with the calculated frequency corresponding to the bumpiness component $[0, 1]$ of the precession motion with $j = +1$, that is $f_{EIC} = -1.2f_{\theta}^{prec} = 8.4kHz$. This indicates that the RIC can resonate with the precession motion of helically

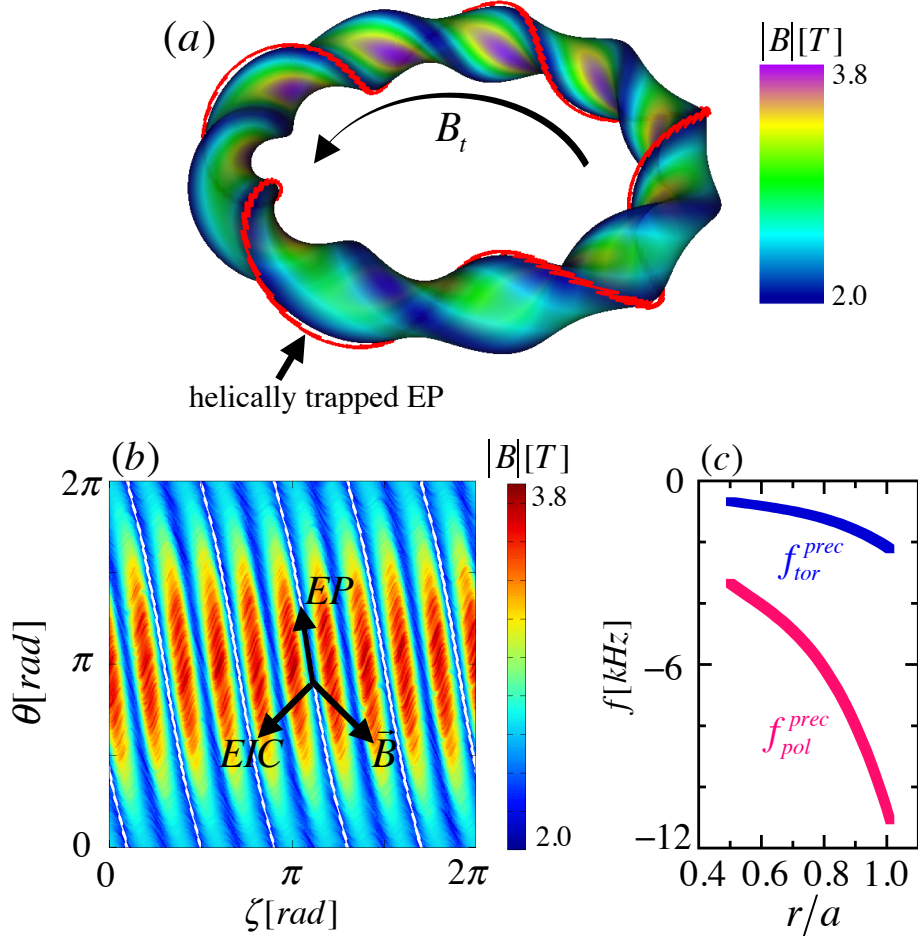


Fig. 3.5 (a) A bird's-eye view of the LHD plasma with the contour plot of the field strength and the orbit of a helically trapped energetic ion with the energy $E_b \sim 34keV$ and pitch angle $\chi \sim 85^\circ$. (b) Contour of the field strength expanded onto the 2D plane of poloidal and toroidal angle at $\iota = 1$ surface, indicating the EP orbit. The directions of the magnetic field, the EP orbit and EIC propagation are also indicated with the arrows. (c) The poloidal (f_{pol}^{prec}) and toroidal (f_{tor}^{prec}) precession frequencies calculated from the orbit simulations shown in (a) and (b).

trapped energetic ions, and this resonance will lead to the destabilization of the EIC, even if the RIC propagates poloidally in the opposite direction to that of the energetic ions.

3.4 Mode eigenfunctions

The spatial structure of the radial plasma displacement ξ_r of the EIC is substantially important for the understanding of the new instability. It will provide the important basic informations for both experiment and theory, such as the impact region of the EIC on LHD plasma and also the category of MHD instability that the EPs resonate with and so on. As a first step before deriving the real mode eigenfunction, we try to evaluate the stability of the LHD plasma in the high T_i discharge and search for the potential MHD instability, which helically trapped EPs may resonate with.

3.4.1 Simulated mode eigenfunction during the RIC linear growth

To identify this weakly unstable mode, the Mercier criterion is accessed by the VMEC code (Hirshman and Whitson, 1983). The ideal interchange mode is accessed to be stable due to the large stabilization term by strong magnetic shear and small destabilization term of low β_{bulk} , shown in Fig. 3.6(b). In a further investigation, a global calculation of resistive modes based on the reduced linear MHD equations in a helical cylinder plasma is performed to solve the eigenvalue problem (Ueda et al., 2014) for a typical EIC shot. The radial structure of the scalar potential perturbation has a Gaussian-shape at the mode rational surface with quite a narrow width, as shown with the curves in Fig. 3.6(c).

Scanning the magnetic Reynolds number S and plasma β_{bulk} reveals that the linear growth rate of the numerically observed mode agrees well with the S and β_{bulk} dependences of the growth rate of the RIC analytically derived by the linear MHD theory (Carreras et al., 1987), i.e. $\gamma \propto S^{-1/3} \beta$, as seen in Figs. 3.7(a) and (b). The above calculation result strongly suggests that the most likely candidate of the observed weakly destabilized mode before the EIC is the RIC. In a magnetic hill region where magnetic shear stabilization is not expected, the RIC would be always unstable in the case without any kinetic stabilization effects.

3.4.2 Mode eigenfunctions of the RIC and EIC in LHD experiment

Because the electron temperature T_e is supposed to be a function of magnetic flux surface, T_e data measured by electron cyclotron emission (ECE) (Kawahata et al., 2003) in optical thick plasma with 100kHz sampling rate are adopted to derive \tilde{T}_e . The \tilde{T}_e is derived from

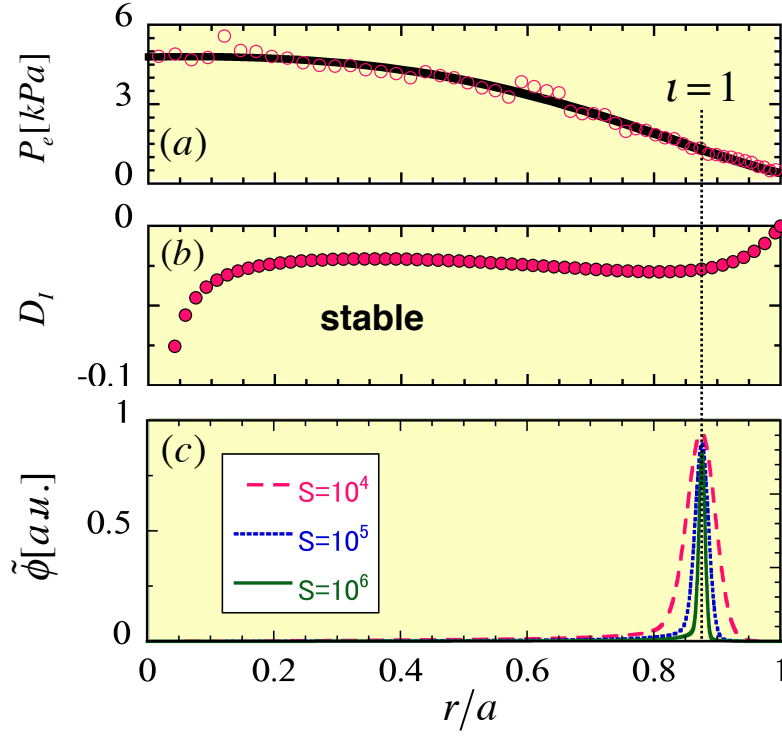


Fig. 3.6 (a) The radial profile of electron pressure in a typical shot with the EIC in LHD. (b) Mercier index for stability of ideal interchange mode. (c) The eigenfunctions of resistive interchange mode calculated by a linear resistive MHD code for $S = 10^4$, $S = 10^5$, and $S = 10^6$, respectively. The vertical dotted line indicates the $\iota = 1$ surface.

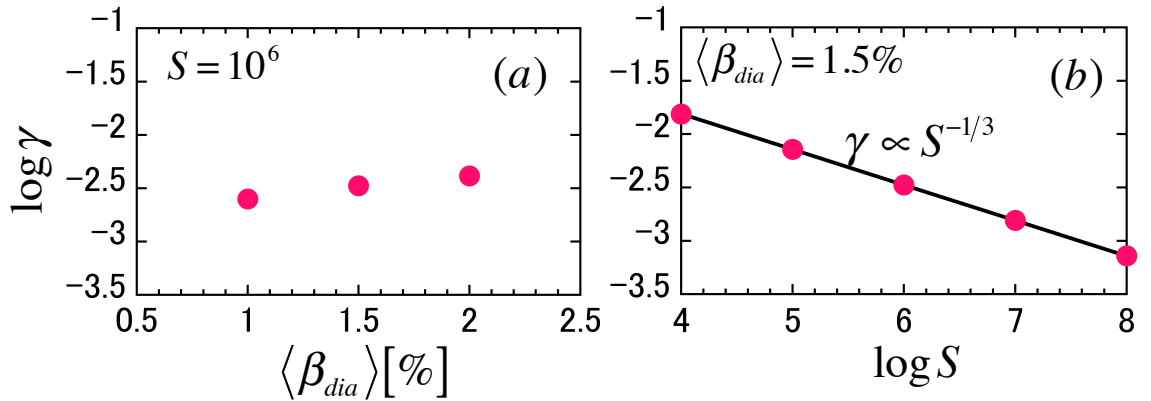


Fig. 3.7 (a) The linear growth rate of the RIC as the function of the plasma β for $S = 10^6$. (b) The linear growth rate of the RIC as the function of magnetic Reynolds number S for $\beta = 1.5\%$.

$\tilde{T}_e/T_{e,eq}$ on the assumption that plasma is incompressible, i.e., $\nabla \cdot \xi_r = 0$. Because the T_e can be expressed as follows, following the Taylor expansion:

$$T_e = T_e(a) + T'_e(x-a) + \dots \quad (3.2)$$

$$\tilde{T}_e \sim \xi_r \cdot \nabla T_{e,eq} \quad (3.3)$$

Here, \tilde{T}_e is electron temperature fluctuation induced by MHD instability and $T_{e,eq}$ is the electron temperature gradient of the background plasma. Since the waveform of the EIC is strongly distorted and the mode frequency rapidly chirps down in a few *ms*, as discussed previously, the traditional fast Fourier transform (FFT) is not an appropriate way to derive \tilde{T}_e induced by the EIC. Instead, the empirical mode decomposition (EMD) method is employed in this analysis. One typical example of extraction of \tilde{T}_e induced by the EIC from an ECE channel around the mode rational surface is shown in Fig. 3.8.

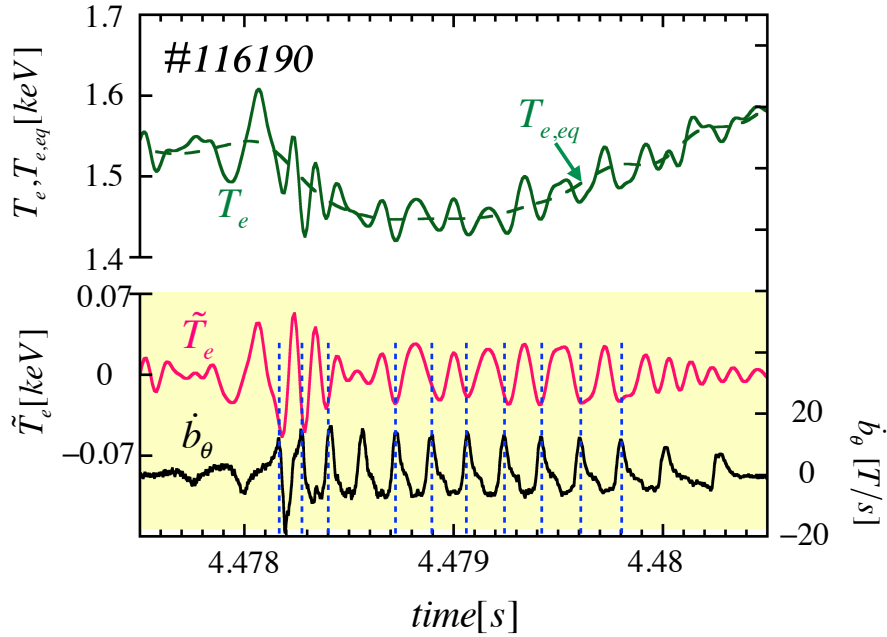


Fig. 3.8 Time evolutions of electron temperature T_e , measured by ECE (solid line) and the slowly evolving equilibrium component $T_{e,eq}$ derived from the EMD method (dashed line). The derived fluctuations of electron temperature \tilde{T}_e , correlated with the magnetic probe signal \dot{b}_θ by the EMD method.

As seen in Fig. 3.8, the EMD method decomposes the measured T_e into a slowly evolving component $T_{e,eq}$ [dashed curve] and rapidly oscillating component \tilde{T}_e . The former $T_{e,eq}$ reflects the slow time evolution of bulk electron temperature. The latter \tilde{T}_e is the intrinsic

mode function (IMF) associated with the EIC due to the high correlation between \tilde{T}_e and magnetic probe signal \dot{b}_θ . Note that each IMF derived by the EMD has different frequency, reflecting various fluctuations induced by MHD modes or noises. Then we define such ‘highly-correlated’ \tilde{T}_e as a reference signal. The radial structure of \tilde{T}_e can be obtained with reduced noises uncorrelated with the EIC, by conditionally averaging the profiles of \tilde{T}_e derived from all other ECE channels by EMD over each crest or trough in the waveform of the above-mentioned reference signal. The results obtained by the EMD technique are summarized in Figs. 3.9(b) – (e). We discuss them in detail as follows,

First, we analyze a weakly oscillatory mode of $\sim 4kHz$ in phase I before the EIC. As seen from Fig. 3.9(b), the \tilde{T}_e shows an even function strongly localized around $\iota = 1$ mode rational surface at $r/a \sim 0.88$. The trough (red) and the crest (blue) of \tilde{T}_e appear in phase and synchronize with the magnetic probe signal in Fig. 3.9(a). The eigenfunction in phase II just before entering the bursting phase (i.e., the EIC) has a similar localized character of that in phase I, but extends radially inward, having a much broader mode width. Although the amplitude of \tilde{T}_e is comparable to that in phase I, the magnetic fluctuation amplitude \tilde{T}_e derived from time integration of the probe signal is enhanced almost double compared with that in phase I. Then, in phase III the mode amplitude is significantly enlarged. It should be noted that at the beginning of phase III the mode frequency suddenly increases to $8.5kHz$, of which frequency is close to the precession frequency of helically trapped energetic ions, as discussed in subsection (2.1). As shown in Fig. 3.9(b), in phase III is strongly enhanced in the region of $0.88 < r/a < 0.91$, holding the RIC-type eigenfunction. Moreover, a complicated radial structure of develops in the inner region of $0.6 < r/a < 0.85$ for a very short time interval of $\sim 0.3ms$. The structure has several radial nodes and propagates inward. However, this complex radial structure does not survive and shrinks rapidly towards the mode rational surface. Soon after, a steady magnetic island-type structure appears in \tilde{T}_e of phase IV with $\sim \pi$ phase difference across the mode rational surface and persists in the latter half of the chirping phase of the EIC, as shown in Fig. 3.9(e).

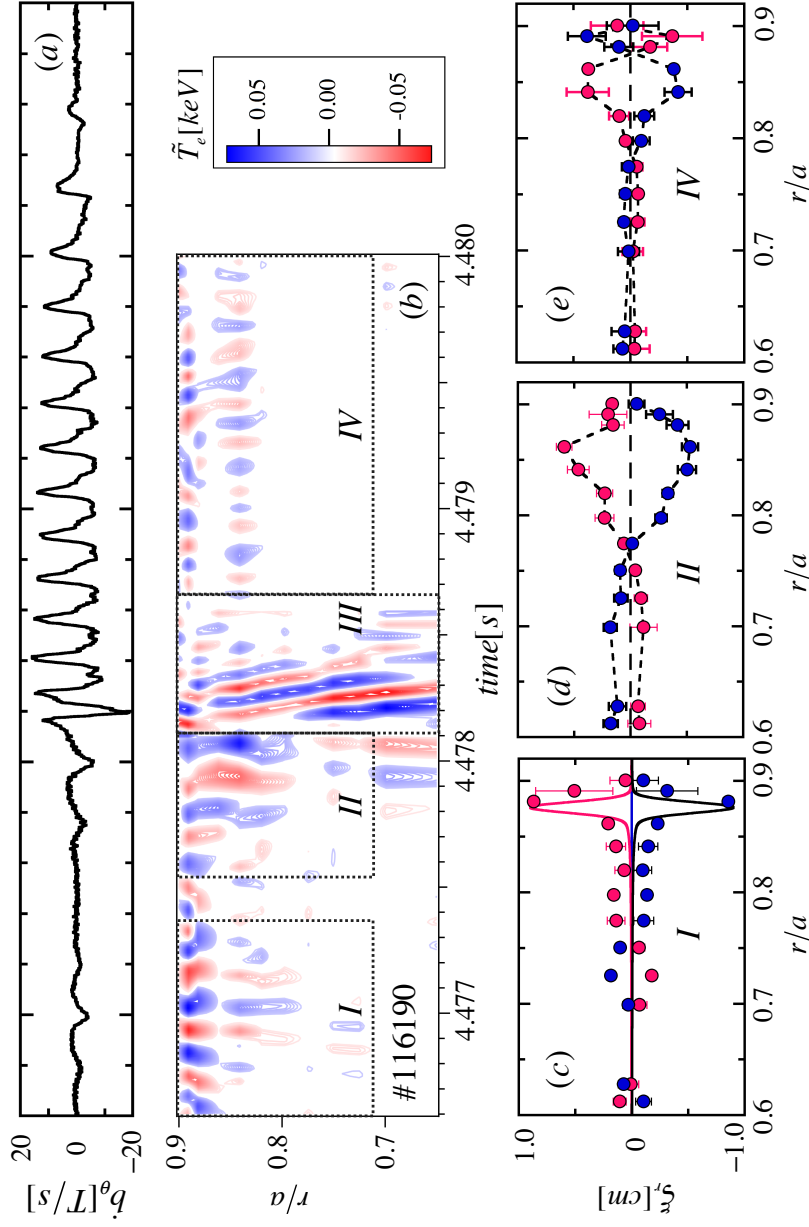


Fig. 3.9 Time evolutions of the magnetic probe signal with one typical EIC b_θ (a) and the radial structure of the electron temperature fluctuations \tilde{T}_e in (b). Radial displacements functions derived from conditionally averaged \tilde{T}_e data for each crest (black) and trough (red) of \tilde{T}_e in the phases I (c), II (d) and IV (e), and the error bars are estimated from the standard deviation of \tilde{T}_e . The eigenfunction of RIC calculated by a linear resistive MHD code is overlaid in (c) with solid curves.

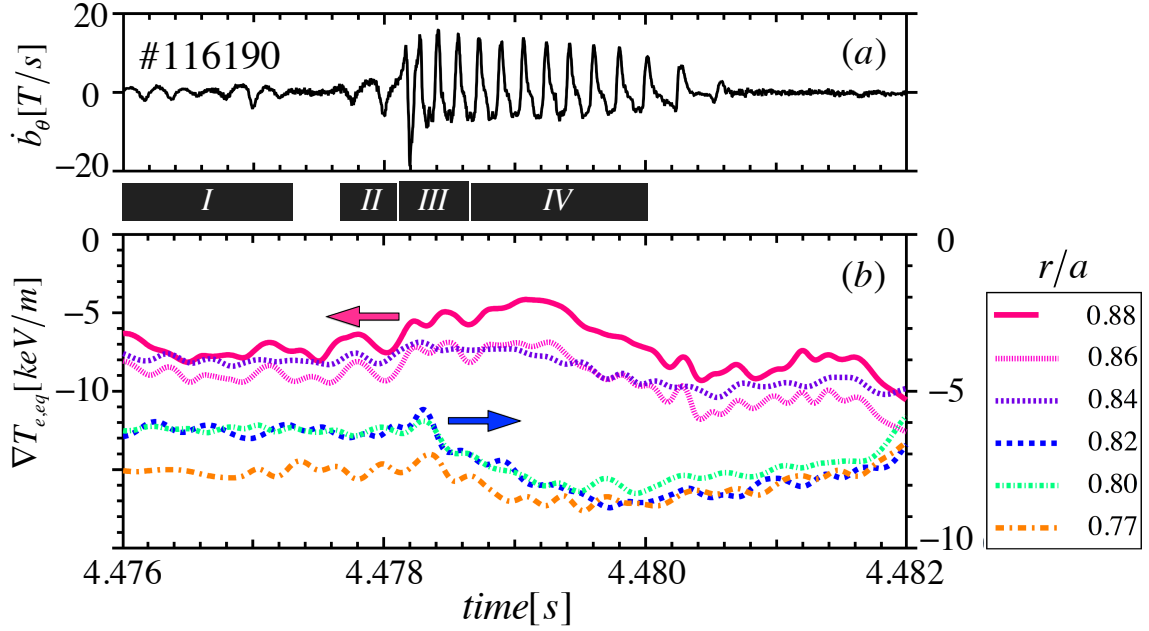


Fig. 3.10 Time evolutions of the magnetic probe signal with one typical EIC \dot{b}_θ (a) and the radial structure of the electron temperature fluctuations \tilde{T}_e in (b). Radial displacements functions derived from conditionally averaged \tilde{T}_e data for each crest (black) and trough (red) of \tilde{T}_e in the phases I (c), II (d) and IV (e), and the error bars are estimated from the standard deviation of \tilde{T}_e . The eigenfunction of RIC calculated by a linear resistive MHD code is overlotted in (c) with solid curves.

Second, the time evolution of the gradient of equilibrium electron temperature $\nabla T_{e,eq}$ is of assistance to explain the observed time behavior of \tilde{T}_e . Every five neighboring radial measurement points of the ECE are aligned as a group to estimate $T_{e,eq}$ for minor radii of $0.77 < r/a < 0.88$, as shown in Fig. 3.10. Before the EIC, $\nabla T_{e,eq}$ is nearly constant and is evaluated as an even function in phase I, of which peak is $\sim 1\text{cm}$ (see Fig. 7(c)). This agrees well with the eigenfunction calculated by a global resistive MHD eigenvalue code [9] for $S = 10^6$, as seen from Fig. 3.6(c) and Fig. 3.9(c). In phase II, the amplitude of ξ_r is comparable with that in phase I, but the mode width is clearly expanded. After the transition to the EIC that lasts for phases III and IV, a clear reduction of $\nabla T_{e,eq}$ near the $\iota = 1$ surface of $r/a \sim 0.88$ is observed. On the contrary, $\nabla T_{e,eq}$ on the inboard side of is obviously enhanced, associated with the flattening around the $\iota = 1$ surface by the EIC. The observed phenomena are caused by the flattening in $T_{e,eq}$ profile around the $\iota = 1$ surface during the EIC. The flattening of the trapped EP pressure profile by the EIC will be also predicted. Hence, it may contribute to destabilization of the EIC in more interior region with thus steepened gradient, that is, broadening the mode width inwardly in phase III of Fig 7(b). In phase IV,

the further reduction of is observed around the $\iota = 1$ surface. The peak-to-peak amplitude of ξ_r is evaluated as $\sim 1\text{ cm}$, comparable with those in phase I and II.

3.5 Threshold of the EIC excitation

Throughout the experimental campaign of the EIC study, the EICs are observed on a certain parameter range of the line-averaged electron density $\langle n_e \rangle$, central electron temperature T_{e0} , absorbed PERP-NBI power $P_{NBI,\perp}$, toroidal field B_t , the magnetic axis position R_{ax} and so on. So far, a systematic parameter scan is not carried out. Here the discharge condition that the EICs are observed is crudely investigated using a simple parameter space defined by T_{e0} and $\langle n_e \rangle$. It is shown in Fig. 3.11 for various injected PERP-NBI power. The figure also includes the data without the EIC even if the maximum injected power of PERP-NBI is applied. A clear electron density threshold of $\langle n_e \rangle \sim 1.5 \times 10^{19} \text{ m}^{-3}$ is found in plasmas where T_{e0} exceeds 1 keV , suggesting a certain lower bound of trapped energetic ion density should be satisfied for the EIC destabilization. This also suggests the existence of the threshold pressure of trapped energetic EPs.

Moreover, in a specific shot No. 116122, the volume-averaged beam beta $\beta_{h\perp}$ of helically trapped energetic ions is scanned in time by continuously decreasing $\langle n_e \rangle$ (and the central electron density n_{e0}) and increasing T_{e0} on the condition of nearly fixed absorbed power of PERP-NBI to study the threshold of the EIC destabilization, as shown in Fig. 3.12. This discharge scenario increases the slowing down time τ_s of helically trapped energetic ions gradually and accordingly increases $\beta_{h\perp}$. As seen from Fig. 11(a), the RIC is firstly ilized by the continuous increment of β_{bulk} from 0.2% to 0.3%. With the increase of $\beta_{h\perp}$, the RIC are suddenly transformed to repetitive several EIC bursts at $\beta_{h\perp} \sim 0.3\%$. That is, a transition from the RIC to the EIC takes place. The density of energetic ions produced by the PERP-NBI, estimated by a beam deposition code ‘MORH’ (Seki et al., 2013), is clearly increased at $t \sim 4.16\text{ s}$ compared with time slices without the EIC, i.e., $t \sim 4.06\text{ s}$, shown in Fig. 3.12(d). The threshold of the beam beta at $\iota = 1$ surface for the transition is also estimated to be $\beta \sim 0.2\%$.

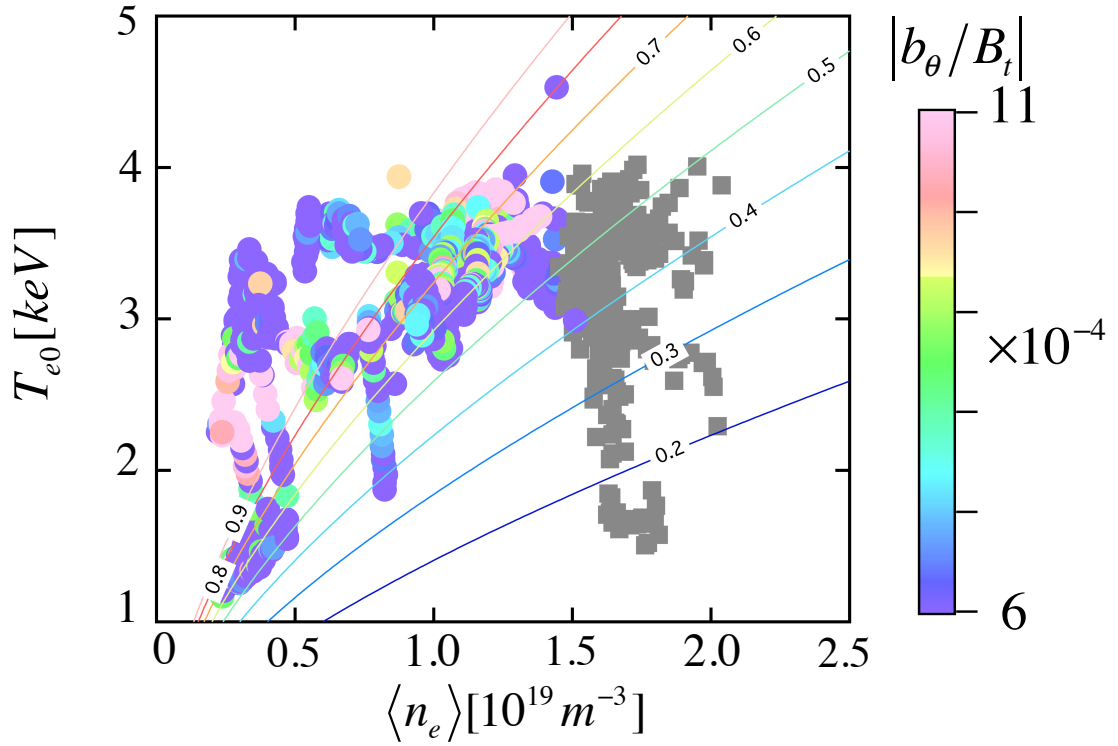


Fig. 3.11 Time evolutions of the magnetic probe signal with one typical EIC \dot{b}_θ (a) and the radial structure of the electron temperature fluctuations \tilde{T}_e in (b). Radial displacements functions derived from conditionally averaged \tilde{T}_e data for each crest (black) and trough (red) of \tilde{T}_e in the phases I (c), II (d) and IV (e), and the error bars are estimated from the standard deviation of \tilde{T}_e . The eigenfunction of RIC calculated by a linear resistive MHD code is overlotted in (c) with solid curves.

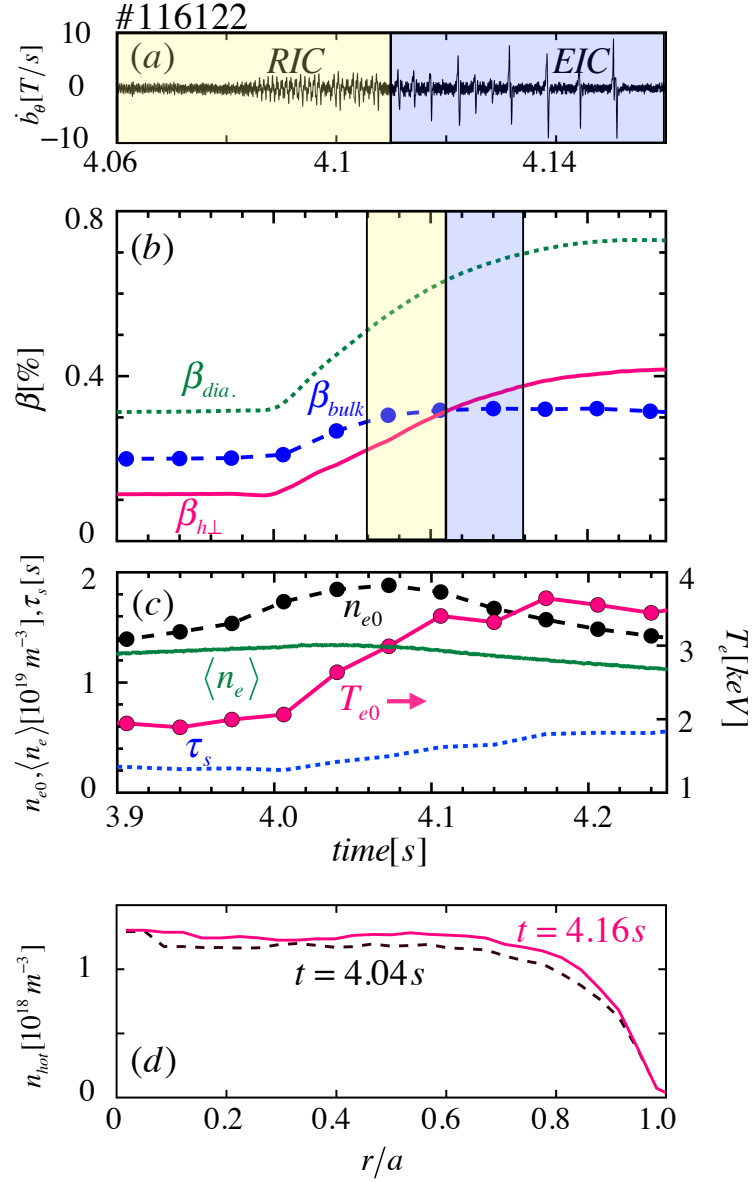


Fig. 3.12 (a) An expanded view of a magnetic probe signal (\dot{b}_θ) is shown. (b) Time evolutions of non-thermal component of volume-averaged plasma beta perpendicular to magnetic field line ($\beta_{h\perp}$) derived by subtracting volume-averaged bulk plasma beta (β_{bulk}) from diamagnetic plasma beta measured by a diamagnetic loop ($\beta_{dia.}$), (c) central electron temperature (T_{e0}), electron density (n_{e0}), line-averaged electron density ($\langle n_e \rangle$) and slowing down time (τ_s) of energetic ions. (d) The deposited density profile from PERP-NBI at $t = 4.04 \text{ s}$ and $t = 4.16 \text{ s}$ by MORH code, respectively.

Chapter 4

Experimental observations of the EIC impacts

4.1 Rapid change of perpendicular energetic neutral flux

The impacts of the EIC on the confinement of helically trapped energetic ions are investigated by a compact neutral particle energy analyzer (CNPA) with fast time response of $0.1ms$ [33]. The sightline of CNPA is arranged to monitor the neutral flux perpendicular to the magnetic axis. The energy distribution of charge-exchanged neutral particles having nearly 90° pitch angle can be obtained with the CNPA over the energy range E from $0.8keV$ up to $150keV$. Typical contour plot of the neutral flux up to $40keV$ observed in a shot having the EIC is shown in Fig. 4.1, where the injection beam energy of PERP-NBI is $34keV$.

The neutral flux suddenly increases in $E < 30keV$, synchronizing with each EIC. This indicates “clump” formation (Berk et al., 1996, 1999) through resonant interaction between the EIC and helically trapped energetic ions, as similar to the case of TAE bursts (toroidicity-induced shear Alfvén eigenmode) (Osakabe et al., 2006). However, the “hole” is not clearly observed so far. The neutral flux detected by the CNPA can be expressed as $\Gamma_0 = \int_V n_{EP} n_0 \langle \sigma v \rangle$, where n_{EP} and n_0 are the densities of the energetic ions and neutrals, respectively. The integration volume V is determined by the sightline and the solid angle of the detector of the CNPA viewing an LHD plasma. Sudden increase of the charge-exchanged neutral flux at the onset of the EIC occurs in the energy range from $\sim 10keV$ to $\sim 30keV$. This increase of the neutral flux is interpreted that the resonant energetic ions are transported from the area where the EIC is active to the edge region of higher neutral density, because the H_α emission indicating recycled neutrals do not increase during the EIC.

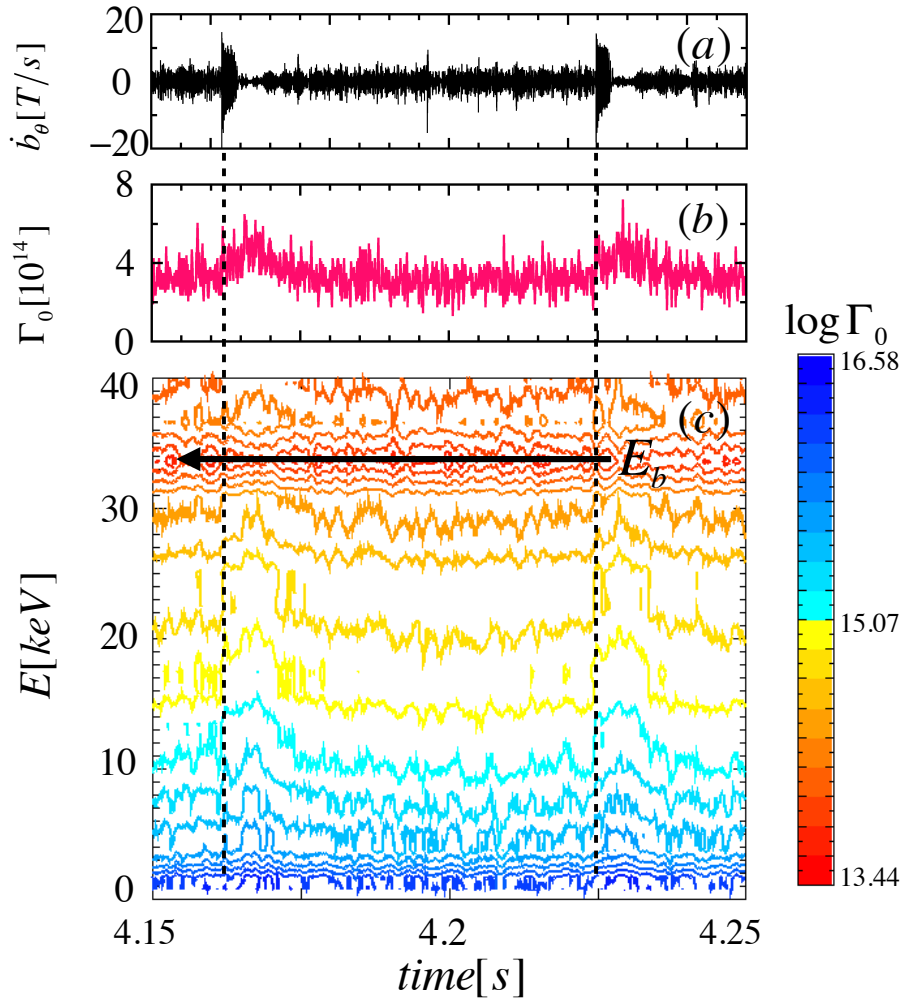


Fig. 4.1 Temporal evolutions of a magnetic probe signal with two EICs (a) and the charge-exchanged neutral flux at the energy of 20keV (b). Time evolution of the energy spectra obtained by the CNPA viewing perpendicular to the plasma (c).

4.2 Generation of negative radial electric field

It is interesting to measure the plasma potential change induced by the EIC, since non-ambipolar radial transport of the helically trapped EPs by the EIC is expected. In this experiment, plasma potential change is obtained with a heavy ion beam probe (HIBP) by measuring the energy change of the secondary beam (i.e., Au^{2+} ions) generated along the orbit of an HIBP primary Au^{1+} beam orbit in a plasma (Ido et al., 2006). Figure 4.2 illustrates a significant and sharp drop of plasma potential in the plasma core region of $0 < r/a < 0.5$, associated with each EIC. In this figure, a zoomed waveform of the potential change is also shown in Fig. 4.2(c). The detailed time evolution of the plasma potential is useful to discuss the EP loss process and toroidal rotation change in later sub-sections (3.3) and (3.4). The potential drop tends to increase and then saturate with the increase of the energetic neutral flux $\Gamma_0 > 10keV$, as shown in Figs. 4.2(b) and (d). The observed potential drop indicates that non-ambipolar radial transport, i.e., losses and redistribution, of helically trapped EPs is clearly induced by each EIC burst.

The radial profiles of the plasma potential drop induced by the EIC having nearly the same amplitude are obtained by a $10Hz$ radial sweep of a probe beam of the HIBP in the magnetic configurations of $R_{ax} = 3.6m$ and $R_{ax} = 3.75m$, where the time duration of the EIC of $\sim 3ms$ is much smaller than the radial scanning period of the beam of $50ms$. The result is shown in Fig. 4.3. In the $R_{ax} = 3.6m$ configuration (No. 122476), the beam is scanned in the region of $0 < r/a < 0.5$. The measured potential drop is $\sim 13keV$ and uniform over the region. Moreover, in the $R_{ax} = 3.75m$ configuration (No. 109190), the probe beam can be scanned over the wider region of $0 < r/a < 0.9$. The potential drop $\Delta\phi$ is nearly constant ($\sim 13kV$) in the core of $0 < r/a < 0.6$ and quickly increases in the peripheral region of $0.6 < r/a < 0.9$, as seen from Fig. 4.3(c). This clearly indicates a generation of negative radial electric field in the edge region. The radial electric field induced by the EIC is estimated from the fitted profile of the potential change $\Delta\phi$ shown with a solid curve in Fig. 4.3(c). The radial electric field profile is modeled as follows:

$$E_r = -85 \cdot \exp[-((\rho - 0.85)/0.15)^2] kV/m \quad (4.1)$$

It should be noted that the neoclassical radial electric field is much smaller than the EIC-induced in the edge region. The at the edge is dominated by induced by EIC and reaches .

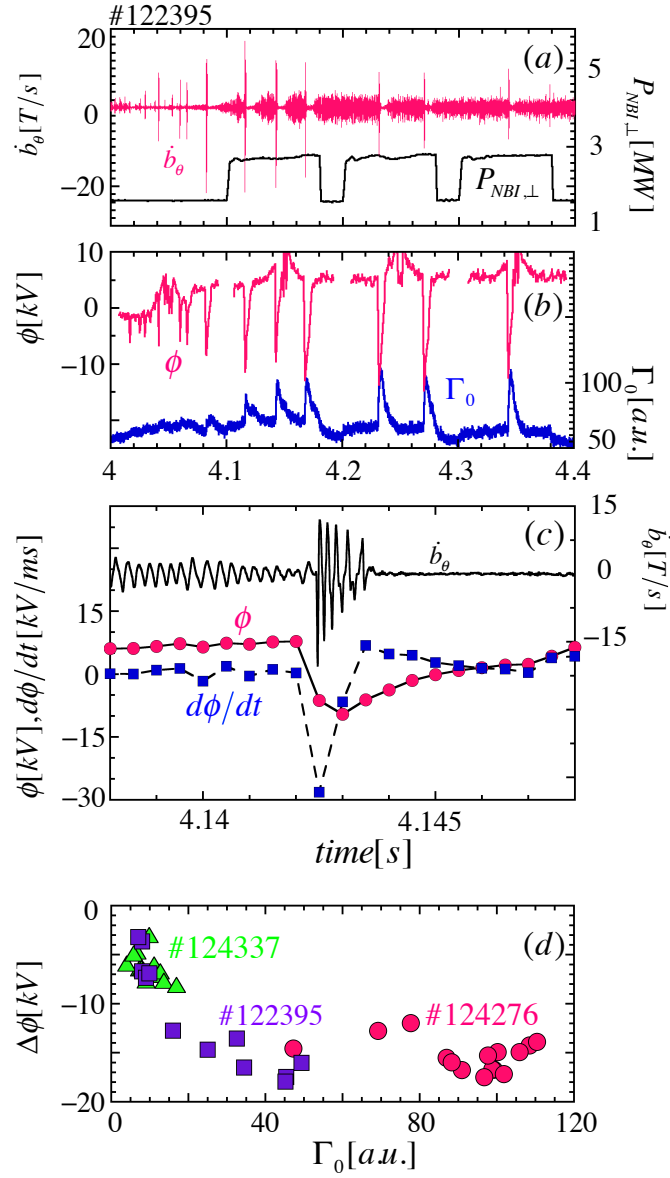


Fig. 4.2 Time evolutions of a magnetic probe signal (\dot{b}_θ) and the absorbed power of PERP-NBI ($P_{NBI\perp}$) (a) and the plasma potential near plasma center of by HIBP (ϕ) and the charge exchanged neutral flux (Γ_0) in the range of $E > 10\text{keV}$ measured by a Si-FNPA detector (b). An expanded view of \dot{b}_θ , ϕ and time derivative of ϕ ($d\phi/dt$) for one EIC (c). In (d), the data of potential drop at $r/a \sim 0$ by the EICs is shown as a function of Γ_0 .

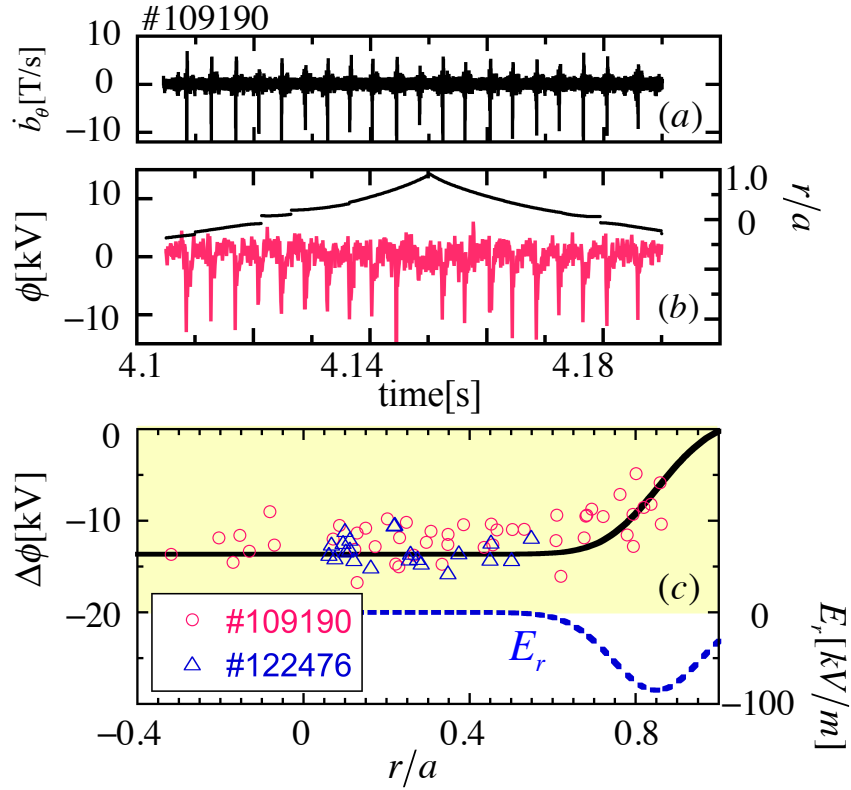


Fig. 4.3 Time evolutions of the magnetic probe signal (a) and the plasma potential obtained by a radial beam scan (r/a) of HIBP (b). Radial profile of the potential change during EIC burst in $R_{ax} = 3.75m$ (circles) in No.109190 and $3.6m$ (triangles) configurations in No.122476 and the fitted profile (black) (c). The radial electric field E_r derived from the fitted $\Delta\phi$ is also indicated with a broken curve.

4.3 Change of plasma flow by the EIC

As discussed above, very large radial electric field ($E_r \sim 85kV/m$) near the edge is transiently formed by the EIC. Thus, it is expected that the generated radial electric field could induce plasma mean flow and sheared flow significantly. The mean flow change induced by the EIC is investigated using the data obtained by the CXRS. The CXRS measures the Doppler effect on spectral lines emitted by recombination process of C^{6+} ions to acquire the mean velocity of thermal ions. Here, it should be noted that the temperature relaxation time of C^{6+} ions with C^{6+} ions and also with protons are typically $\tau_{CC} \sim 0.5ms$ and $\tau_{CH} \sim 10ms$, respectively. This means that the time evolution of plasma rotation detected by the CXRS during the EIC of $3ms$ duration can indicate the changes of C^{6+} ion temperature and the flow, and does not necessarily indicate the changes on thermal protons. A flow of bulk fuel

ions, i.e., protons would be modified the same as C^{6+} ions, although the flow changes would have noticeable differences between proton and impurity ions depending on collisionality regime. The toroidal rotation changes of ions by the EIC are seen from Figs. 4.4(b) and (c).

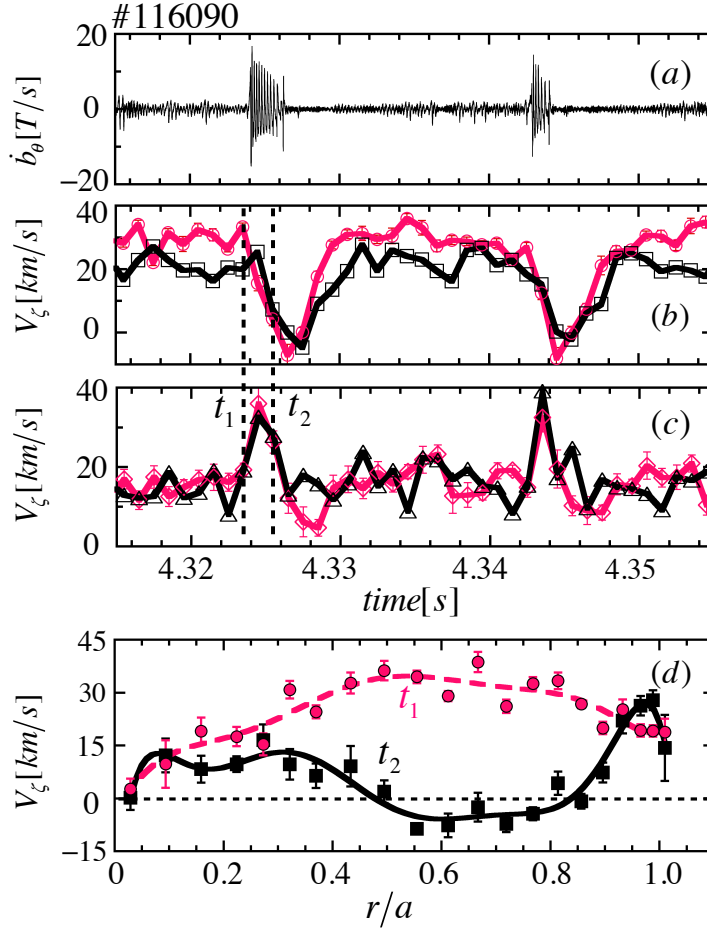


Fig. 4.4 Time evolution of a magnetic probe signal in the phase in which two EIC bursts appear (a), toroidal rotation velocities of C^{6+} ions at r/a 0.8 (circles), r/a 0.85 (squares) in (b) and those at r/a 0.92 (diamond) and r/a 0.98 (triangular) in (c), respectively. (d) The radial profiles of the measured toroidal rotation at $t = t_1$ (dashed line) and t_2 (solid line), marked in (c) and (d).

Co-directional toroidal rotation is braked by the EIC down to nearly no rotation or even slightly reversed in the region of $r/a < 0.9$. In contrast to the behavior in the plasma core region, the toroidal rotation in the very edge region of $r/a > 0.9$ is enhanced noticeably in

the co-direction, as shown in Fig. 4.4(c), even though the E_r remains negative during an EIC burst. The radial profile of toroidal flow at t_1 just before an EIC burst is compared with that at during the EIC in Fig. 4.4(d), where t_1 and t_2 are indicated with two dashed lines in Figs. 4.4(b) and (c). Note that the toroidal flow near the plasma center is fairly small at t_1 and t_2 because of the balanced injection of TANG-NBI. It should be noted that a significant modification of toroidal rotation takes place in a very wide region of $0.4 < r/a < 1.0$.

4.4 Suppression of micro-turbulence during the EIC

In LHD, the edge plasma transport is dominated by turbulent transport. The effects of the EIC on density fluctuations related to micro-turbulence are studied with the 2D phase contrast imaging (PCI) diagnostic system (Tanaka et al., 2008). Density fluctuations in the frequency range of 20kHz to 500kHz are measured by this technique in the region of $0.3 < r/a < 1.0$. The root-mean-squared amplitude of the line integrated density fluctuations $\delta n_{e,rms}$ is clearly reduced by up to $\sim 50\%$ during each EIC detected by magnetic probes, as shown in Fig. 18(a).

The radial profiles of density fluctuation amplitude and its phase velocity are derived from the PCI data by an inversion technique with the help of high magnetic shear of the magnetic configuration (Tanaka et al., 2008). The results show that intense density fluctuations propagating in the ion-diamagnetic drift direction in the laboratory frame are clearly identified around the phase velocity of 5km/s and are encircled with the rectangular frames in Fig. 4.5(b). Since the Doppler effect due to plasma rotation of the density fluctuations is thought to be small in the inter EIC burst phase where intense turbulent fluctuations are excited, the propagation direction and its phase velocity of the fluctuations are thought to be the same as those in the plasma frame. On the other hand, the density fluctuations are significantly suppressed during each EIC burst, as shown in Fig. 4.5(c). The suppressed density fluctuations at $r/a \sim 0.85$ have a peak around the perpendicular wavenumber normalized by a thermal ion gyro radius $k\rho_{Ti} \sim 0.3$. It should be noted that the density fluctuations at the same radial location are noticeably accelerated in the electron diamagnetic drift direction in both inboard and outboard sides, as seen from Fig. 4.5(c). An electrostatic gyrokinetic linear stability calculation is carried out with the GS2 code (Dorland et al., 2000), including multiple species, fully kinetic descriptions of all species and collision, to infer the candidate electrostatic fluctuations. The result shows that the suppressed turbulence is likely to be ion temperature gradient (ITG) mode (Nunami et al., 2012), as well as in the previous study (Mikkelsen et al., 2014), which locates in the region of $0.5 < 4/1 < 1.0$ with a peak at $r/a \sim 0.8$ and propagates in the ion diamagnetic drift direction. The linear growth rate is

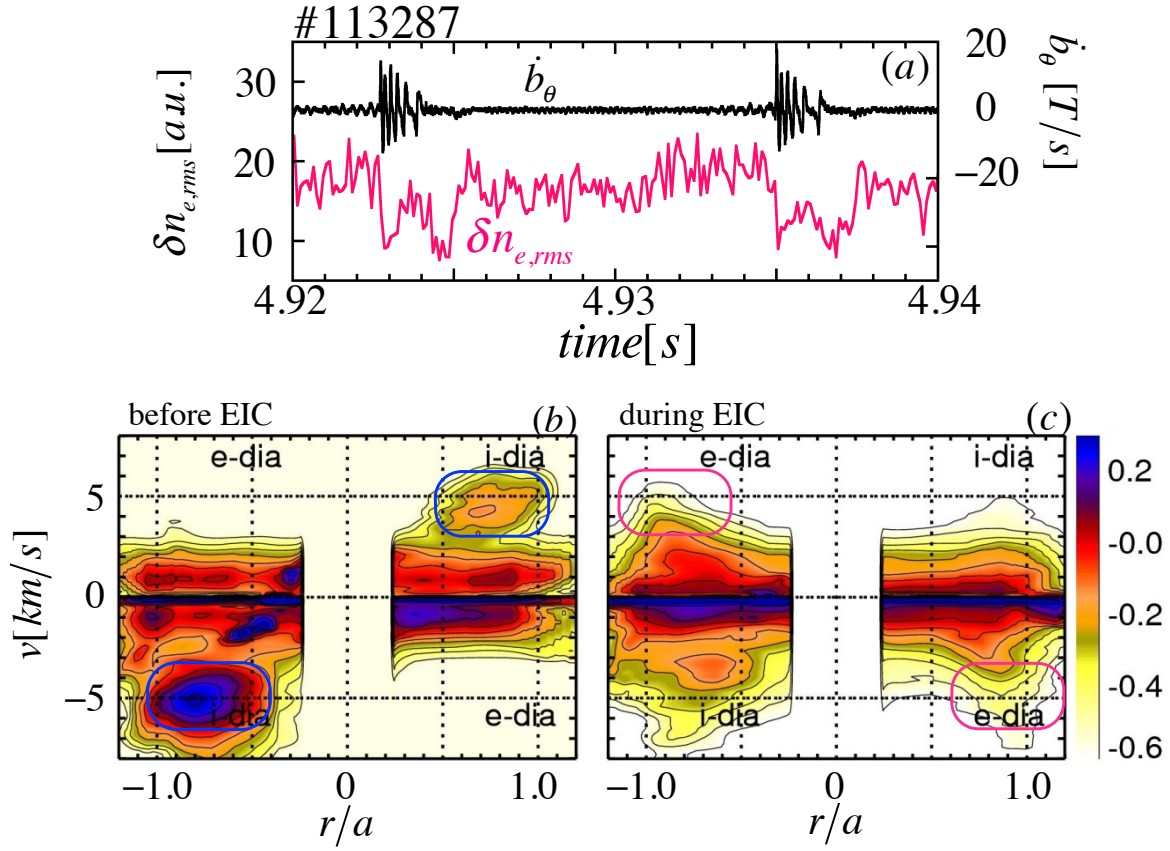


Fig. 4.5 Time evolution of a magnetic probe signal in the phase in which two EIC bursts appear (a), toroidal rotation velocities of C^{6+} ions at r/a 0.8 (circles), r/a 0.85 (squares) in (b) and those at r/a 0.92 (diamond) and r/a 0.98 (triangular) in (c), respectively. (d) The radial profiles of the measured toroidal rotation at $t = t_1$ (dashed line) and t_2 (solid line), marked in (c) and (d).

estimated to be $\sim 1.5 \times 10^5 s^{-1}$. On the other hand, the $E_r \times B$ shearing rate that would be realized by the EIC is estimated to be $\sim 2.5 \times 10^5 s^{-1}$ at $r/a \sim 0.88$ from the E_r profile modeled from the HIBP data in sub-section (3.2). The shearing rate expected from the experimental data is comparable or slightly larger than the linear growth rate predicted by GS2 code. This suppression of ITG mode might be attributed to the generation of significant sheared flow by the EIC (Ritz et al., 1990).

Chapter 5

Models to explain the EIC impacts

5.1 Estimation of helically trapped ion loss induced by the EIC

It is of great importance to evaluate the loss of helically trapped EPs from the point of view of serious damage of plasma facing components. It is also interesting to clarify the role of the EIC-induced EP loss as a cost in suppressing micro-turbulence, as will be discussed in the next section. Here, we employ the following simple methods to estimate the fraction of the EPs that would be lost or re-distributed by the EIC, since direct methods such as a lost ion probe and neutron diagnostics are not applicable to the present experimental condition. Two methods are employed here to overcome the above difficulties.

5.1.1 Loss/redistribution estimation from the potential reduction

The first method is based on the EIC-induced E_r , of which E_r is measured by the HIBP. From the Poisson equation and charge conservation equation:

$$\langle \nabla \cdot \vec{E} \rangle_r = \frac{Q}{\epsilon_0(\epsilon_{\perp} - 1)} \quad (5.1)$$

$$\langle \nabla \cdot \vec{j} \rangle_r = \frac{\partial Q}{\partial t} \quad (5.2)$$

Accordingly, the net radial current density j_r can be derived as follows:

$$\vec{j}_r = \epsilon_0(\epsilon_{\perp} - 1) \frac{\partial E_r}{\partial t} = -\epsilon_0(\epsilon_{\perp} - 1) \frac{1}{\partial t} \left(\frac{\partial \phi}{\partial r} \right) \quad (5.3)$$

The perpendicular dielectric tensor can be expressed as [43, 44],

$$\epsilon_{\perp} \sim \left(\frac{c}{v_A}\right)^2 \left(1 + \frac{q^2}{\sqrt{\epsilon_h}}\right), \quad (5.4)$$

where c is the light speed, v_A is the Alfvén velocity, q is the safety factor ($q = 1$) and ϵ_h is the helical ripple ($\epsilon_h = 0.25$ in this experiment).

Therefore,

$$\frac{v_A}{c} = 7.28 \mu^{-1/2} n_i^{-1/2} B = \frac{7.28 \times 2.75 \times 10^4}{\sqrt{0.25 \times 10^{13}}} = 0.126 \quad (5.5)$$

$$\epsilon_{\perp} \sim \left(1 + \frac{q^2}{\sqrt{\epsilon_h}}\right) \left(\frac{c}{v_A}\right)^2 = \left(\frac{1}{0.126}\right)^2 \left(1 + \frac{1}{\sqrt{0.25}}\right) = 188 \quad (5.6)$$

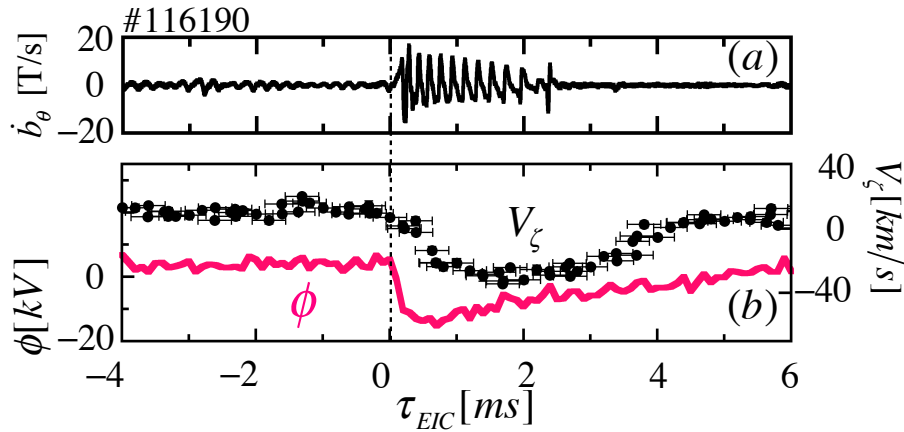


Fig. 5.1 Waveforms of the EIC burst (a) and the observed toroidal flow V_{ζ} and plasma potential ϕ (b), as a function of the relative time for the EIC onset.

At the beginning of the EIC, a rapid drop of plasma potential is observed in the experiment, as seen from Fig. 5.1(b) suggests that $j_{EP} \gg j_{return}$, where j_{return} is the total return current density generated by bulk plasma components, as mentioned above. Therefore, in this phase the net radial current density j_r is mainly dominated by j_{EP} , so that the magnitude of j_{EP} would be estimated as follows:

Thus,

$$j_{EP} = \epsilon_0(\epsilon_{\perp} - 1) \frac{\partial E_r}{\partial t} = 8.85 \times 10^{-12} \times 188 \times \frac{80 \times 10^3}{0.1 \times 10^{-3}} = 1.4[A] \quad (5.7)$$

On the other hand, the magnitude of j_{EP} can be also estimated by,

$$j_{EP} \sim e \langle n_{EP}^{loss} \rangle V_{EP}, \quad (5.8)$$

where n_{EP}^{loss} is the loss of EPs density averaged over the EIC-impact region of $0.6 < r/a < 1$ and V_{EP} is the effective radial drift velocity of resonant EPs, which is roughly the ratio of mode width to the duration of the EIC (Okabayashi et al., 2011).

$$V_{EP} \sim \frac{w_{RIC}}{dT} \sim \frac{0.15 \times 0.64[m]}{2[ms]} \sim 0.048[km/s], \quad (5.9)$$

Therefore, the density of the EP loss is roughly estimated as $n_{EP}^{loss} \sim 2.7 \times 10^{17} m^{-3}$. That is, the fraction of the EP loss at the mode rational surface is $\sim 40\%$ for the value calculated by MORH code (Seki et al., 2013).

5.1.2 Estimation from the diamagnetic loop

The second method is able to estimate the loss fraction of EPs from the plasma confinement region and is expected to exclude the redistribution of EPs where EPs would be still confined in a plasma. This method is based on the diamagnetic loop measurement. The diamagnetic loop can detect the perpendicular pressure of helically trapped EPs with the pitch angle nearly $\chi = 90^\circ$ in a non-isotropic pressure plasma as well as the bulk plasma pressure coming from thermal electrons and ions. A rapid drop of the time derivative of the stored energy obtained from the diamagnetic loop signal dW_{dia}/dt across an EIC burst will provide the information of the EP loss rate if the rapid change of the bulk plasma pressure by the EIC would be negligibly small. As will be discussed in the next section, the bulk plasma pressure is usually increased slightly by the EIC. This leads to a small positive contribution in across the EIC, but will be neglected at the just onset of the EIC.

Figure 5.2 shows that the maximum magnitude of the drop of dW_{dia}/dt is typically $\sim 1MW$ for *sim3MW* deposition power of PERP-NBI at the beginning of the EIC. This means that the loss rate of helically trapped EPs averaged over a whole plasma volume reaches $\sim 30\%$. Note that the time resolution of W_{dia} is $0.1ms$ and is expected to capture the rapid drop in dW_{dia}/dt by the EIC because the growth time of the EIC is $\sim 0.2ms$ as mentioned in section 4. The above result suggests that each EIC burst induces a large loss fraction of helically trapped energetic ions, i.e., $\sim 30\%$, averaged over the plasma volume. In the present experimental condition, the strong E_r generation by the EIC is dominantly caused by the losses and the effect of redistribution of the EPs is small. The large losses of the helically trapped EPs by the EIC may also be linked to the existence of wide loss cone

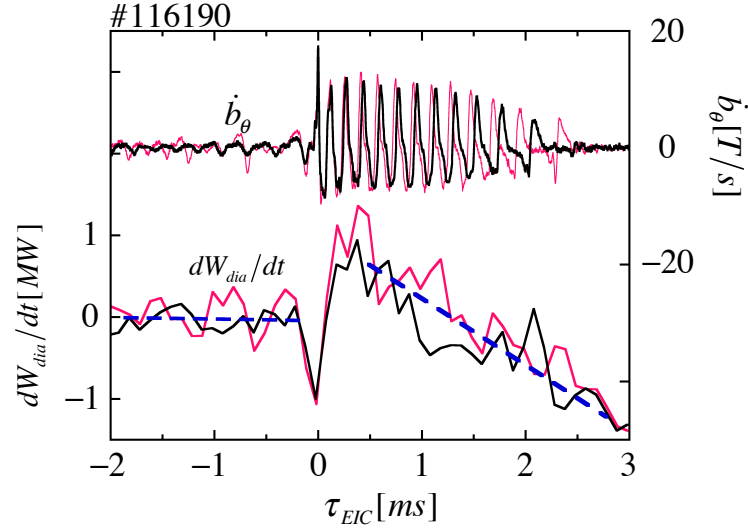


Fig. 5.2 Time evolutions of a magnetic probe signal (\dot{b}_θ) with two EIC bursts and the changes of time derivative of total stored energy measured by a diamagnetic loop (dW_{dia}/dt) corresponding to the two EICs, respectively. The relative time τ_{EIC} is defined at the onset of the EIC

region slightly away from the 90° pitch angle in the outboard side (larger major radius side) of the LHD plasma (Sanuki et al., 1990).

5.2 A model to explain toroidal rotation change

Since very large radial electric field ($E_r \sim 85kV/m$) near the edge is transiently formed by the EIC and the observed plasma mean flow is also strongly modified as shown in Fig. 4.4, it is interesting to connect the E_r inferred from HIBP and ΔV_ζ following the neoclassical theory.

5.2.1 Calculated ΔV_ζ based on the neoclassical theory

The toroidal flow change observed for C^{6+} ions comes from the toroidal torque input to bulk plasma as a reaction responding to non-ambipolar radial transport (losses and redistribution) induced by the EIC, i.e., $-\langle j_{EP} B_\theta \rangle$, because of toroidal momentum conservation. Here, j_{EP} is the effective outward EP-loss-driven current density and B_θ is the poloidal field. The minus sign of $-\langle j_{EP} B_\theta \rangle$ means a ‘reaction’ to the EP-loss induced torque. The bracket means the flux-surface averaging. The j_{EP} is balanced with a total return current density by bulk plasma

components,

$$j_{return} = j_{rt-p} + j_{rt-I} + j_{rt-e} \quad (5.10)$$

where j_{rt-p} , j_{rt-I} and j_{rt-e} are the return current densities by thermal protons, impurity ions (C^{6+} ions here) and electrons, respectively. Accordingly, the torque $-\langle j_{EP} B_\theta \rangle$ induced by EP losses is balanced with a sum of the torque by the above-mentioned three dominant return currents. As discussed in the previous chapter, the non-ambipolar EP losses can generate the negative radial electric field E_r near the edge through the excess of j_{EP} for the total bulk return current density. The torque induced by j_{rt-I} of C^{6+} ions or the generated negative E_r leads to the reduction of the toroidal flow observed for C^{6+} ions. The toroidal flow of protons also will be slowed down by the torques due to the bulk proton return current as similar to C^{6+} ions.

The following equation based on the neoclassical theory of non-axisymmetric toroidal plasma is employed to interpret the observed toroidal rotation change of the impurity ion (Nakajima and Okamoto, 1991):

$$\langle u_I \cdot \nabla \zeta \rangle = -\frac{1}{i} \left(\frac{1}{e_I n_I} \frac{dP_I}{d\psi} + \frac{d\phi}{d\psi} \right) + \frac{J}{i(J + iI)} \quad (5.11)$$

$$\left\{ (1 - \langle G_{BS} \rangle_I) \left(\frac{1}{e_I n_I} \frac{dP_I}{d\psi} + \frac{d\phi}{d\psi} \right) + \langle G_{BS} \rangle_I \left[-L_{54} \frac{1}{e_i} \frac{dT_i}{d\psi} + \frac{1}{e_I n_I} \frac{dP_I}{d\psi} - \frac{1}{e_i n_i} \frac{dP_i}{d\psi} \right] \right\}, \quad (5.12)$$

where $J \equiv RB_\zeta$, $\psi \equiv r^2 B_\zeta / 2$, $\langle G_{BS} \rangle_I$ is the normalized geometric factor for the impurity ion and $2\pi I$ is the total toroidal current inside the flux surface. Here, θ and ζ are the poloidal and toroidal angles in Boozer coordinates, respectively. The quantity ϕ is the plasma potential. Since the above-mentioned EIC-induced radial electric field is a dominant term for small neoclassical electric field and diamagnetic terms. From this approximation in eq. (2), the change of plasma toroidal flow of carbon impurity is simply expressed as a steady-state value for a net toroidal current free plasma ($I = 0$) as:

$$V_\zeta = - \left(\frac{R}{J} \right)^2 \left(\frac{\langle G_{BS} \rangle_I}{r} \right) \frac{d\phi}{dr}, \quad (5.13)$$

where V_ζ is the EIC-induced toroidal rotation velocity change. For a low beta plasma in the LHD magnetic configurations of $R_{ax} = 3.6m$ and $R_{ax} = 3.75m$, $\langle G_{BS} \rangle_I$ decreases from ~ 8 at the center to zero toward the plasma edge, and finally reverses the sign (~ -1) in the very edge region of $0.95 < r/a < 1.0$ (Nakajima and Okamoto, 1991; Watanabe et al., 1995).

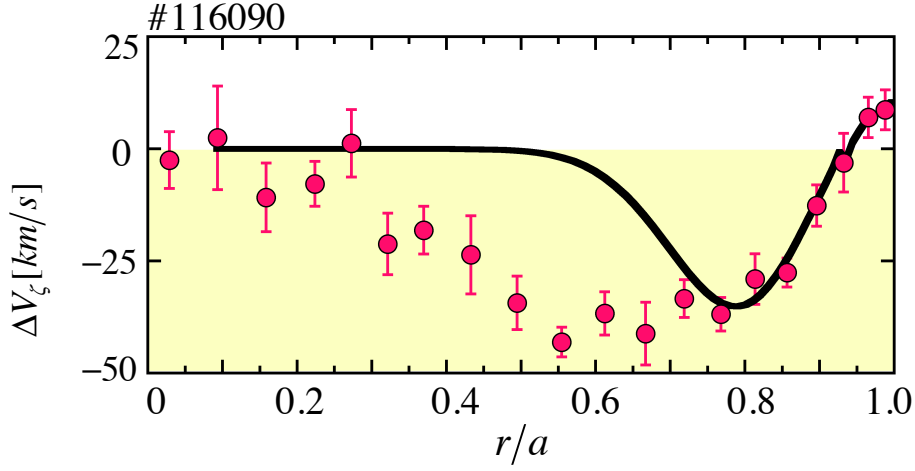


Fig. 5.3 A simulated toroidal rotation change based on neoclassical theory (curve) and the change of C^{6+} ions toroidal rotation velocity measured by CXRS (solid circles) are shown.

As seen from Fig. 5.3, the change of toroidal carbon flow ΔV_ζ calculated by the above equation using E_r inferred from the HIBP data $\Delta\phi$, shown in Fig. 4.3(c) at the time that the change reaches the maximum shows good agreement with the toroidal flow change measured by CXRS (solid circles) in the plasma peripheral region, including the flow reversal in the very edge of $0.9 < r/a < 1$.

5.2.2 Calculated ΔV_ζ by taking account of a hyper- μ_\perp profile

The model based only on the neoclassical theory can explain the toroidal rotation change in very edge region, but cannot explain the large deviation between the calculated carbon flow and the measured one in the inner region of $0.4 < r/a < 0.6$. This deviation may be explained by a viscous diffusive term of toroidal flow velocity $-\mu_\perp \nabla V_\zeta$ in the toroidal momentum balance equation for C^{6+} ions:

$$\frac{\partial V_\zeta}{\partial t} + \mu_\perp \nabla V_\zeta + \frac{F_\zeta}{m_I n_I} = 0 \quad (5.14)$$

where μ_\perp is the perpendicular momentum diffusivity. The quantity F_ζ is an external force in the toroidal direction to take into account the torque to C^{6+} ions induced by the EIC here.

In so-called high Ti discharges, the density fluctuations are theoretically suggested to be due to ion temperature gradient driven turbulence (ITG) (Mikkelsen et al., 2014; Nunami et al., 2012). Accordingly, the momentum diffusivity μ_\perp is predicted to be comparable

with ion thermal diffusivity χ_i , that is roughly, $\mu_\perp \sim \chi_i = 10m^2/s$, where the double of χ_i derived from the steady state ion heat balance (Nagaoka et al., 2011) is adopted to simulate the transient transport (Cardozo, 1995). For simplicity, μ_\perp is assumed to be constant ($= 10m^2/s$) in the region of $0 < r/a < 0.7$ and then gradually decays towards LCFS (last closed flux surface), as shown in Fig. 5.4.

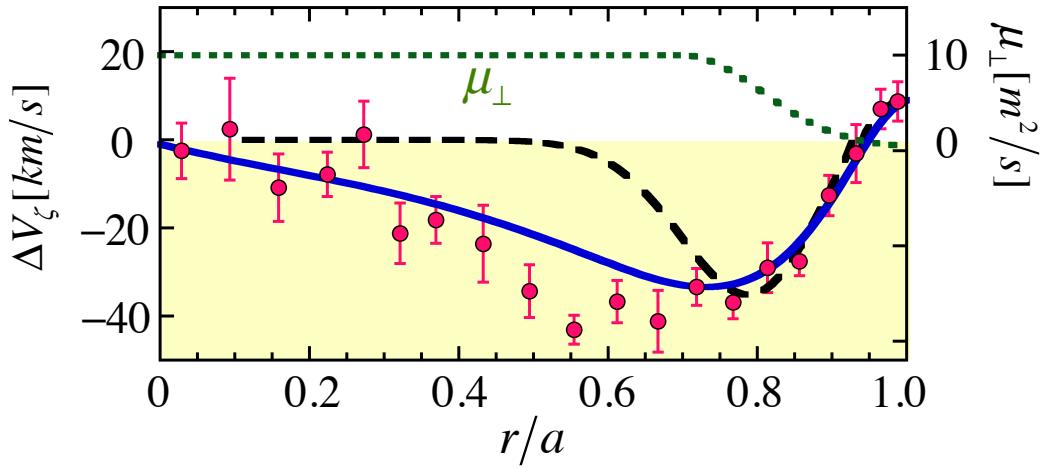


Fig. 5.4 Radial profiles of the assumed perpendicular viscosity μ_\perp (dotted line), a simulated toroidal rotation change based on neoclassical theory without the radial diffusion term by perpendicular viscosity (dashed line) and a simulated toroidal rotation change with the assumed perpendicular viscosity (solid line). The change of C^{6+} ions toroidal rotation velocity measured by CXRS is shown with circles.

The profile shape is assumed based on the experimental findings of the dramatic suppression of micro-turbulence around the mode rational surface during the EIC, which will be discussed below. In addition, the external force F_ζ related to the torque by the EIC in eq. (4) can be inferred from $\Delta V_\zeta / \tau_V$, where τ_V is a typical time scale of the observed toroidal rotation change, i.e., $\sim 1ms$ and ΔV_ζ is the toroidal rotation change calculated from the eq. 5.13. The solid curve in Fig. 5.4 illustrates the calculated toroidal rotation change on the assumed μ_\perp profile, in $2ms$ later from the initial rotation profile [shown with a dashed line in Fig. 4.4(d)]. The result calculated with the diffusion term shows better agreements with the experimental data over a wide radial region, compared with the steady-state solution without the diffusion term, i.e., $\mu_\perp = 0$. This indicates that the radial diffusion of the toroidal momentum due to the perpendicular viscosity plays a substantial role in the toroidal rotation change observed in the inner region away from the EIC mode center.

5.3 Transient improvement of bulk plasma confinement

In LHD plasmas with the EIC, clear increase of line integrated density near the edge is often triggered by each EIC, accompanying a sudden drop of H_α emission and noticeable reduction of density fluctuations, as shown in Fig. 5.5(b).

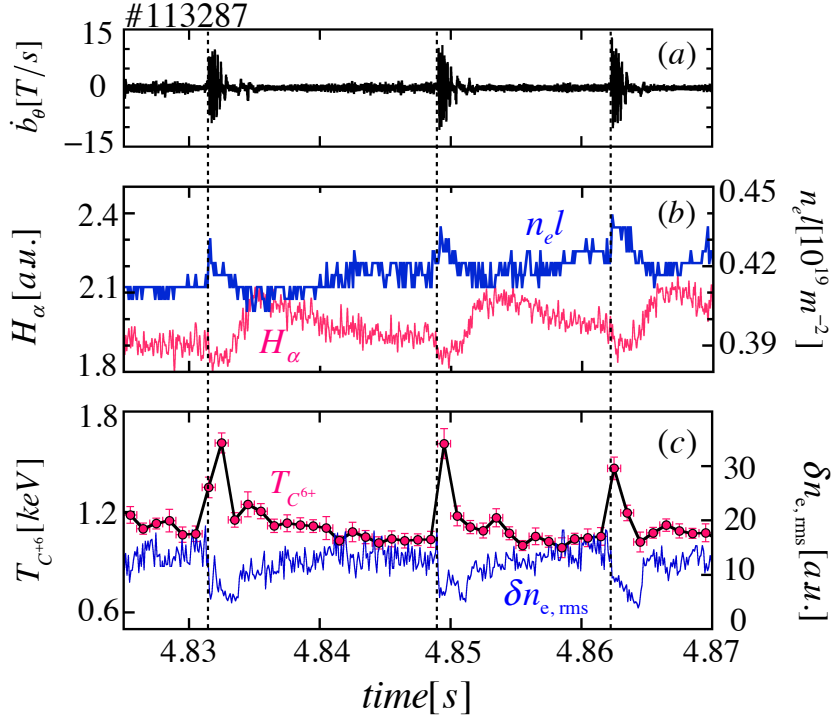


Fig. 5.5 Time evolutions of three EICs in a magnetic probe signal (a), the line integrated electron density ($n_e l$) at plasma peripheral region and the emission of H_α light (b) C^{6+} ion temperature ($T_{C^{6+}}$) around mode rational surface and the root mean squared fluctuations of line integrated density fluctuation ($\delta n_{e,rms}$) measured by PCI (c).

This result indicates the reduction of particle transport near the edge by the EIC. At the same time, rapid increase of C^{6+} temperature $\Delta T_{C^{6+}}$ of up to $\sim 50\%$ is observed in a wide region. The time evolutions of the radial profiles of the increase of C^{6+} ions temperature $\Delta T_{C^{6+}}$ and of the slight decrease of electron temperature ΔT_e across the EIC are shown in Figs. 5.6(b) and (c) for a different shot No. 116190, respectively, where the data of $T_{C^{6+}}$ are conditionally accumulated for nearly 10 EIC events to display the detailed time evolution since the time resolution determined by a CCD camera in the CXRS diagnostic is limited to 0.5ms.

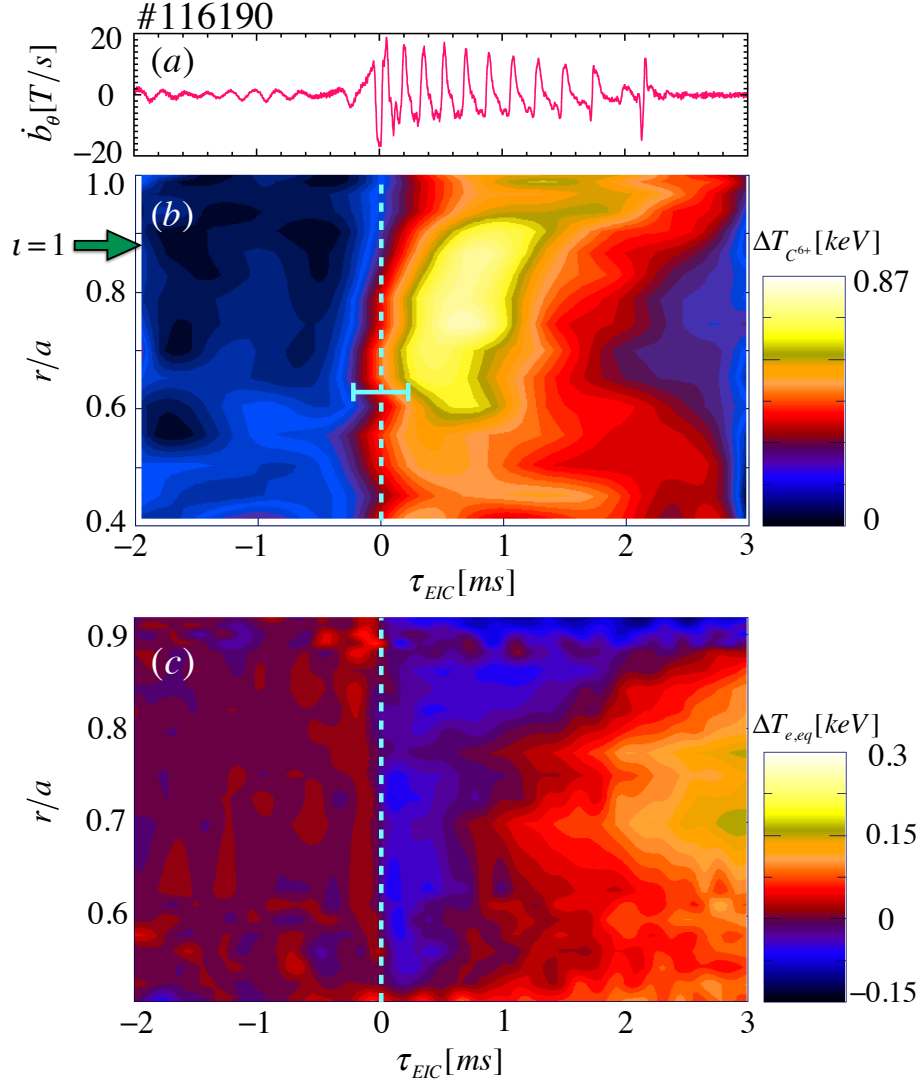


Fig. 5.6 The magnetic probe signal with one EIC (a) and the contour plots of the change in $T_{C^{6+}}$ (b) and T_e (c) as a function of the relative time for the onset of an EIC (τ_{EIC}). The uncertainty in the time caused by the time resolution of CXRS system is indicated by an error bar in (b).

It should be noted that this is consistent with the observation of the rapid increase of $dW_{dia.}/dt$ [Fig. 5.2] just following the sudden drop of $dW_{dia.}/dt$ which is due to the sudden loss of helically trapped energetic ions as discussed above. The collisional relaxation time among C^{6+} ions of $T_{C^{6+}} \sim 1keV$ and $n_{C^{6+}} \sim 0.05n_e$ is $\sim 0.5ms$, comparable to the

time resolution. Hence, the $\Delta T_{C^{6+}}$ is thought to be nearly equivalent to the increase of the equilibrium temperature of $T_{C^{6+}}$ rather than the increase of the effective temperature caused by an effective broadening of a non-Maxwellian distribution. This result suggests the reduction of ion thermal diffusivity of $T_{C^{6+}}$ ions presumably due to suppression of ITG-like micro-turbulence around the $\iota = 1$ surface. However, the turbulence suppression is not sustained throughout the EIC, because j_{return} by bulk plasma would quickly compensate the large plasma potential change and the resulting large E_r generated by the EIC-induced non-ambipolar transport of EPs. In contrast to $\Delta T_{C^{6+}}$, as seen from Fig. 5.6(c), the increment of electron temperature $\Delta T_{e,eq}$ becomes negative noticeably around the $\iota = 1$ rational surface during the former half of the EIC burst. This negative $\Delta T_{e,eq}$ is related to the decrease of $\nabla T_{e,eq}$ around the $\iota = 1$ rational surface, which is shown in Fig. 3.10(b). The results clearly indicate an appreciable enhancement of electron thermal diffusivity χ_e .

It should be noted that the rise rate of the stored energy of C^{6+} ions component at the onset of the EIC is roughly estimated by the time derivative of the volume integral of $\Delta T_{C^{6+}}$ as,

$$\frac{dW_{C^{6+}}}{dt} = \frac{3}{2} \frac{\int_V n_{C^{6+}} \Delta T_{C^{6+}} dV}{dt} \sim 0.47 [MW] \quad (5.15)$$

and even if the rise rate of C^{6+} is significantly high, it does not contradict with the power transfer from PERP-NBI and TANG-NBI to C^{6+} ions, evaluated as.

$$P_{C^{6+}} \sim \frac{n_{C^{6+}} Z^2}{n_H A_Z} P_i \sim 0.68 MW \quad (5.16)$$

Here, n_H, A_Z, Z and P_i are respectively proton density, mass number of C^{6+} ion, its charge and total deposited power to all of ion species. As similar to the impacts of the sheared flow on confinement of C^{6+} ions, the large sheared flow is expected to reduce the heat transport of fuel ions, i.e., protons and to improve the confinement of proton. The time derivative of the stored energy measured by a diamagnetic loop $dW_{dia.}/dt$ recovers quickly to a positive value of $+1MW$ within $\sim 0.25ms$ just after a sharp negative drop due to EP losses, as shown in Fig. 5.2. The positive value of $dW_{dia.}/dt$ is by a factor of 2 larger than $dW_{C^{6+}}/dt$. This suggests that the confinement of bulk fuel and C^{6+} ions is improved transiently by a sheared flow produced by EIC bursts.

Chapter 6

Summary and Conclusions

The resistive interchange modes destabilized through resonant interaction with a characteristic motion of helically trapped energetic ions are observed for the first time, exhibiting bursting character and rapid frequency chirping down in the LHD plasmas. The initial frequency of the mode is consistently explained by the mode-particle resonance condition in a non-axisymmetric LHD plasma. This resonant interaction is clearly found in the rapid changes in the energy spectra of charge exchanged neutral flux below the injected beam energy of 34keV measured by the CNPA. The mode structures derived from the ECE data show that the EIC has a quite similar eigenfunction of the radial displacement of the RIC. That is, the EIC is well localized at the mode rational surface, in the present case $\iota = 1$ surface, even if the EIC has low mode number $m = 1$ and $n = 1$. Moreover, the eigenfunction is an odd function around the rational surface, which indicates an island-type shape, having a localized character of the interchange mode. The EIC affects the electron temperature gradient of the background plasma noticeably. The threshold of the beta value of helically trapped energetic ions is inferred from the parameter scans of the electron density and the temperature of bulk plasma. In a specified shot where the beam beta is increased gradually in time with slowly decreasing $\langle n_e \rangle$ on a fixed NBI power, the threshold is also investigated. This study clearly shows the existence of the threshold of helically trapped energetic ions pressure, i.e., the volume-averaged $\beta_{h\perp} \sim 0.3\%$ and that of local beta of 0.2% at $\iota = 1$ surface.

The EIC also strongly impacts the confinement of helically trapped energetic ions and induces noticeable losses. The non-ambipolar radial transport of the helically trapped energetic ions is consistently inferred from the large and sudden drop of plasma potential measured by the HIBP. Consistently, thus generated radial electric field E_r strongly affects the plasma edge and even more interior region. The large edge E_r shear induces a significant sheared flow, which brings about clear suppression of micro-turbulence and transient improvement of bulk plasma confinement. If the EIC-induced EP losses are favorably controlled within an

acceptable level, the EIC-induced flow shear could trigger an improvement of bulk plasma in future large fusion devices .

References

- Berk, H., Breizman, B., and Pekker, M. (1996). Nonlinear dynamics of a driven mode near marginal stability. *Phys. Rev. Lett.*, 76(8):1256–1259.
- Berk, H. L., Breizman, B. N., Candy, J., Pekker, M., and Petviashvili, N. V. (1999). Spontaneous hole–clump pair creation. *Phys. Plasmas*, 6(8):3102.
- Bosch, H.-S. and Hale, G. (1992). Improved formulas for fusion cross-sections and thermal reactivities. *Nucl. Fusion*, 32(4):611.
- Cardozo, N. J. L. (1995). Perturbative transport studies in fusion plasmas. *Plasma Phys. Control. Fusion*, 37(8):799–852.
- Carreras, B. a., Garcia, L., and Diamond, P. H. (1987). Theory of resistive pressure-gradient-driven turbulence. *Phys. Fluids*, 30(5):1388.
- Chen, L., White, R., and Rosenbluth, M. (1984). Excitation of Internal Kink Modes by Trapped Energetic Beam Ions. *Physical Review Letters*, 52(13):1122–1125.
- Chu, M., Greene, J., Lao, L., Miller, R., Bondeson, A., Sauter, O., Rice, B., Strait, E., Taylor, T., and Turnbull, A. (1996). Resistive Interchange Modes in Negative Central Shear Tokamaks with Peaked Pressure Profiles. *Phys. Rev. Lett.*, 77:2710–2713.
- Coppi, B. and Porcelli, F. (1986). Theoretical Model of Fishbone Oscillations in Magnetically Confined Plasmas. *Phys. Rev. Lett.*, 57(18):2272.
- Dorland, W., Jenko, F., Kotschenreuther, M., and Rogers, B. N. (2000). Electron temperature gradient turbulence. *Phys. Rev. Lett.*, 85(26 Pt 1):5579–5582.
- Du, X., Ohdachi, S., and Toi, K. (2012). Development of an Array System of Soft X-ray Detectors with Large Sensitive Area on the Large Helical Device. *Plasma Fusion Res.*, 7:2401088–2401088.
- Du, X. D., Toi, K., Osakabe, M., Ohdachi, S., Ido, T., Tanaka, K., Yokoyama, M., Yoshinuma, M., Ogawa, K., Isobe, M., Nagaoka, K., Ozaki, T., Sakakibara, S., and Seki, R. (2015). Resistive Interchange Modes Destabilized by Helically Trapped Energetic Ions in a Helical Plasma. *Phys. Rev. Lett.*, 114:155003.
- Goncharov, P. R., Ozaki, T., Sudo, S., Tamura, N., TESPEL Group, LHD Experimental Group, Veshchev, E. A., Sergeev, V. Y., and Krasilnikov, A. V. (2006). Local pellet based and line-integrated nonperturbing charge exchange measurements with a compact neutral particle analyzer on Large Helical Device. *Rev. Sci. Instrum.*, 77(10):10F119.

- Gorelenkov, N., Pinches, S., and Toi, K. (2014). Energetic particle physics in fusion research in preparation for burning plasma experiments. *Nucl. Fusion*, 54(12):125001.
- Günter, S., Gude, A., Hobirk, J., Maraschek, M., Saarelma, S., Schade, S., Wolf, R., and Team, A. U. (2002). MHD phenomena in advanced scenarios on ASDEX Upgrade and the influence of localized electron heating and current drive. *Nucl. Fusion*, 41(9):1283–1290.
- Hao, G. Z., Wang, a. K., Liu, Y. Q., and Qiu, X. M. (2011). Effect of trapped energetic particles on the resistive wall mode. *Phys. Rev. Lett.*, 107:015001.
- Heidbrink, W. W., Austin, M. E., Fisher, R. K., García-Muñoz, M., Matsunaga, G., McKee, G. R., Moyer, R. a., Muscatello, C. M., Okabayashi, M., Pace, D. C., Shinohara, K., Solomon, W. M., Strait, E. J., Van Zeeland, M. a., and Zhu, Y. B. (2011). Characterization of off-axis fishbones. *Plasma Phys. Control. Fusion*, 53(8):085028.
- Hirshman, S. P. and Whitson, J. C. (1983). Steepest-descent moment method for three-dimensional magnetohydrodynamic equilibria. *Phys. Fluids*, 26(12):3553–3568.
- Huang, N. E. and Wu, Z. (2008). A Review on Hilbert-Huang Transform : Method and Its Applications. *Rev. Geophys.*, 46(2008):RG2006.
- Hutchinson (1987). *Principles of plasma diagnostics*. Cambridge University Press.
- Ido, T., Shimizu, A., Nishiura, M., Nishizawa, A., Katoh, S., Tsukada, K., Yokota, M., Ogawa, H., Inoue, T., Hamada, Y., Group, L. H. D. E., and Crowley, T. P. (2006). 6 MeV heavy ion beam probe on the Large Helical Device 6 MeV heavy ion beam probe on the Large Helical Device. *Rev. Sci. Instrum.*, 77:10F523.
- Isobe, M., Darrow, D. S., Kondo, T., Sasao, M., Toi, K., Osakabe, M., Shimizu, H., Yoshimura, Y., Takahashi, C., Murakami, S., Okamura, S., and Matsuoka, K. (1999). Escaping fast ion diagnostics in compact helical system heliotron/torsatron. *Rev. Sci. Instrum.*, 70(1):827–830.
- Isobe, M., Oskabe, M., Ozaki, T., Nishiura, M., Goncharov, P., Veshchev, E., Ogawa, K., Nagaoka, K., Saito, K., Murakami, S., Saida, T., Sasao, M., Tok, K., and LHD Experimental Group (2010). FAST PARTICLE DIAGNOSTICS ON LHD. *Fusion Sci. Technol.*, 58:426.
- Jayakumar, R., Luce, T. C., Taylor, T. S., Turnbull, a. D., Wade, M. R., Austin, M. E., Casper, T. a., Makowski, M. a., Chu, M. S., Lao, L. L., Strait, E. J., and Brennan, D. P. (2002). Observation and analysis of a resistive mode with interchange parity in negative central shear plasmas in the DIII-D Tokamak. *Phys. Plasmas*, 9(12):5043.
- Kawahata, K., Nagayama, Y., Inagaki, S., and Ito, Y. (2003). Broadband electron cyclotron emission radiometry for the Large Helical Device. *Rev. Sci. Instrum.*, 74(3):1449–1452.
- Kolesnichenko, Y. I., Lutsenko, V. V., Wobig, H., and Yakovenko, V. (2002). Alfvén instabilities driven by circulating ions in optimized stellarators and their possible consequences in a Helias reactor. *Phys. Plasmas*, 9(2):517.

- Matsunaga, G., Aiba, N., Shinohara, K., Sakamoto, Y., Isayama, A., Takechi, M., Suzuki, T., Oyama, N., Asakura, N., Kamada, Y., and Ozeki, T. (2009). Observation of an Energetic-Particle-Driven Instability in the Wall-Stabilized High- β Plasmas in the JT-60U Tokamak. *Phys. Rev. Lett.*, 103:045001.
- McGuire, K., Goldston, R., Bell, M., Bitter, M., Bol, K., Brau, K., Buchenauer, D., Crowley, T., Davis, S., Dylla, F., Eubank, H., Fishman, H., Fonck, R., Grek, B., Grimm, R., Hawryluk, R., Hsuan, H., Hulse, R., Izzo, R., Kaita, R., Kaye, S., Kugel, H., Johnson, D., Manickam, J., Manos, D., Mansfield, D., Mazzucato, E., McCann, R., McCune, D., Monticello, D., Motley, R., Mueller, D., Oasa, K., Okabayashi, M., Owens, K., Park, W., Reusch, M., Sauthoff, N., Schmidt, G., Sesnic, S., Strachan, J., Surko, C., Slusher, R., Takahashi, H., Tenney, F., Thomas, P., Towner, H., Valley, J., and White, R. (1983). Study of high-beta magnetohydrodynamic modes and fast-ion losses in PDX. *Phys. Rev. Lett.*, 50(12):891–895.
- Mikkelsen, D. R., Tanaka, K., Nunami, M., Watanabe, T.-H., Sugama, H., Yoshinuma, M., Ida, K., Suzuki, Y., Goto, M., Morita, S., Wieland, B., Yamada, I., Yasuhara, R., Tokuzawa, T., Akiyama, T., and Pablant, N. a. (2014). Quasilinear carbon transport in an impurity hole plasma in LHD. *Phys. Plasmas*, 21(8):082302.
- Nabais, F., Borba, D., Mantsinen, M., Nave, M. F. F., and Sharapov, S. E. (2005). Fishbones in Joint European Torus plasmas with high ion-cyclotron- resonance-heated fast ions energy content. *Phys. Plasmas*, 12:102509.
- Nagaoka, K., Ida, K., Yoshinuma, M., Takeiri, Y., Yokoyama, M., Morita, S., Tanaka, K., Ido, T., Shimizu, a., Tamura, N., Funaba, H., Murakami, S., Goto, M., Takahashi, H., Suzuki, C., Suzuki, Y., Ikeda, K., Osakabe, M., Tsumori, K., Nakano, H., Kaneko, O., and Yamada, H. (2011). Heat and momentum transport of ion internal transport barrier plasmas on the Large Helical Device. *Nucl. Fusion*, 51:083022.
- Nakajima, N. and Okamoto, M. (1991). Rotations of Bulk Ions and Impurities in Non-Axisymmetric Toroidal Systems. *J. Phys. Soc. Japan*, 60(12):4146–4153.
- Narihara, K., Yamada, I., Hayashi, H., and Yamauchi, K. (2001). Design and performance of the Thomson scattering diagnostic on LHD. *Rev. Sci. Instrum.*, 72(1):1122–1125.
- Nunami, M., Watanabe, T.-H., Sugama, H., and Tanaka, K. (2012). Gyrokinetic turbulent transport simulation of a high ion temperature plasma in large helical device experiment. *Phys. Plasmas*, 19(4):042504.
- Okabayashi, M., Matsunaga, G., Degraessie, J. S., Heidbrink, W. W., In, Y., Liu, Y. Q., Reimerdes, H., Solomon, W. M., Strait, E. J., Takechi, M., Asakura, N., Budny, R. V., Jackson, G. L., Hanson, J. M., La Haye, R. J., Lanctot, M. J., Manickam, J., Shinohara, K., and Zhu, Y. B. (2011). Off-axis fishbone-like instability and excitation of resistive wall modes in JT-60U and DIII-D. *Phys. Plasmas*, 18(5):056112.
- Osakabe, M., Yamamoto, S., Toi, K., Takeiri, Y., Sakakibara, S., Nagaoka, K., Tanaka, K., Narihara, K., and Group, t. L. E. (2006). Experimental observations of enhanced radial transport of energetic particles with Alfvén eigenmode on the LHD. *Nucl. Fusion*, 46(10):S911–S917.

- Ritz, C., Lin, H., Rhodes, T., and Wootton, A. (1990). Evidence for Confinement Improvement by Velocity-Shear Suppression of Edge Turbulence. *Phys. Rev. Lett.*, 65(20):2543–2546.
- Sakakibara, S., Watanabe, K. Y., Suzuki, Y., Narushima, Y., Ohdachi, S., Nakajima, N., Watanabe, F., Garcia, L., Weller, A., Toi, K., Yamada, I., Tanaka, K., Tokuzawa, T., Ida, K., Yamada, H., Komori, A., and Motojima, O. (2008). MHD study of the reactor-relevant high-beta regime in the Large Helical Device. *Plasma Phys. Control. Fusion*, 50(12):124014.
- Sanuki, H., Todoroki, J., and Kamimura, T. (1990). Spatial structure of particle-orbit loss regions in $l=2$ helical systems. *Phys. Fluids B Plasma Phys.*, 2(9):2155.
- Seki, R., Watanabe, K., Funaba, H., Suzuki, Y., Matsumoto, Y., Hamamatsu, K., Sakakibara, S., and Ohdachi, S. (2013). Effect of re-entering fast ions on NBI heating power in high-beta plasmas of the Large Helical Device. *Nucl. Fusion*, 53(6):063016.
- Shaing, K.C. and Callen, J. (1983). Neoclassical flows and transport in nonaxisymmetric toroidal plasmas. *Phys. Fluids*, 26(11):3315.
- Sheffield, J. (1994). The physics of magnetic fusion reactors. *Rev. Mod. Phys.*, 66(3):1015–1103.
- Takemura, Y., Sakakibara, S., Watanabe, K., Ichiguchi, K., Ida, K., Suzuki, Y., Ohdachi, S., Narushima, Y., Yamada, I., Tanaka, K., and Yamada, H. (2013). Rotation of Interchange Instability in the Large Helical Device. *Plasma Fusion Res.*, 8:1402123–1402123.
- Tanaka, K., Michael, C., Vyacheslavov, L. N., Sanin, A. L., Kawahata, K., Akiyama, T., Tokuzawa, T., and Okajima, S. (2008). Two-dimensional phase contrast imaging for local turbulence measurements in large helical device (invited). *Rev. Sci. Instrum.*, 79(10):10E702.
- Toi, K., Ogawa, K., Isobe, M., Osakabe, M., Spong, D. a., and Todo, Y. (2011). Energetic-ion-driven global instabilities in stellarator/helical plasmas and comparison with tokamak plasmas. *Plasma Phys. Control. Fusion*, 53(2):024008.
- Toi, K., Ohdachi, S., Yamamoto, S., Nakajima, N., Sakakibara, S., Watanabe, K., Inagaki, S., Nagayama, Y., Narushima, Y., Yamada, H., Narihara, K., Morita, S., Akiyama, T., Ashikawa, N., Ding, X., Emoto, M., Funaba, H., Goto, M., Ida, K., Idei, H., Ido, T., Ikeda, K., Imagawa, S., Isobe, M., Itoh, K., Kaneko, O., Kawahata, K., Kobuchi, T., Komori, A., Kubo, S., Kumazawa, R., Li, J., Liang, Y., Masuzaki, S., Mito, T., Miyazawa, J., Morisaki, T., Murakami, S., Muto, S., Mutoh, T., Nagaoka, K., Nakamura, Y., Nakanishi, H., Nishimura, K., Nishizawa, A., Noda, N., Notake, T., Ohkubo, K., Ohtake, I., Ohyabu, N., Oka, Y., Okamura, S., Ozaki, T., Peterson, B., Sagara, A., Saida, T., Saito, K., Sakamoto, R., Sasao, M., Sato, K., Sato, M., Satow, T., Seki, T., Shimoizuma, T., Shoji, M., Sudo, S., Tanaka, M., Tamura, N., Tanaka, K., Tsumori, K., Uda, T., Watari, T., Weller, A., Xu, Y., Yamada, I., Yokoyama, M., Yoshimura, S., Yoshimura, Y., Yamazaki, K., Matsuoka, K., Motojima, O., Hamada, Y., and Fujiwara, M. (2004). MHD instabilities and their effects on plasma confinement in Large Helical Device plasmas. *Nucl. Fusion*, 44(2):217–225.

- Toi, K., Ohdachi, S., Yamamoto, S., Sakakibara, S., Narihara, K., Tanaka, K., Morita, S., Morisaki, T., Goto, M., Takagi, S., Watanabe, F., Nakajima, N., Watanabe, K., Ida, K., Ikeda, K., Inagaki, S., Kaneko, O., Kawahata, K., Komori, A., Masuzaki, S., Matsuoka, K., Miyazawa, J., Nagaoka, K., Nagayama, Y., Oka, Y., Osakabe, M., Ohyabu, N., Takeiri, Y., Tokuzawa, T., Tsumori, K., Yamada, H., Yamada, I., and Yoshinuma, K. (2005). Observation of the low to high confinement transition in the large helical device. *Phys. Plasmas*, 12(2):020701.
- Ueda, R., Watanabe, K. Y., Matsumoto, Y., Itagaki, M., Sato, M., and Oikawa, S. (2014). Characteristics of magnetic island formation due to resistive interchange instability in helical plasma. *Phys. Plasmas*, 21(5):052502.
- Watanabe, F., Toi, K., Ohdachi, S., Suzuki, C., Sakakibara, S., Watanabe, K. Y., Morita, S., Narihara, K., and Tanaka, K. (2007). Soft and Ultra-Soft X-ray Detector Array Systems for Measurement of Edge MHD Modes in the Large Helical Device. *Plasma Fusion Res.*, 2:S1066–S1066.
- Watanabe, F., Toi, K., Ohdachi, S., Takagi, S., Sakakibara, S., Watanabe, K., Morita, S., Narihara, K., Tanaka, K., and Yamazaki, K. (2006a). Radial structure of edge MHD modes in LHD plasmas with L–H transition. *Plasma Phys. Control. fusion*, 48:A201–A208.
- Watanabe, K., Nakajima, N., Okamoto, M., Yamazaki, K., Nakamura, Y., and Wakatani, M. (1995). Effect of collisionality and radial electric field on bootstrap current in the Large Helical Device. *Nucl. Fusion*, 35(3):335–345.
- Watanabe, K., Suzuki, Y., Sakakibara, S., Yamaguchi, T., Nakamura, Y., Ida, K., Nakajima, N., Yamada, H., and LHD Experimental Group (2010). Characteristics of MHD Equilibrium and related issues on LHD. *Fusion Sci. Technol.*, 58:160–175.
- Watanabe, K. Y., Masamune, S., Takemura, Y., Funaba, H., Sakakibara, S., Watanabe, F., Tanaka, K., Ohdachi, S., Toi, K., and Narushima, Y. (2011). Effect of pressure-driven MHD instabilities on confinement in reactor-relevant high-beta helical plasmas. *Phys. Plasmas*, 18(5):056119.
- Watanabe, T., Matsumoto, Y., Hishiki, M., Oikawa, S., Hojo, H., Shoji, M., Masuzaki, S., Kumazawa, R., Saito, K., Seki, T., Mutoh, T., Komori, A., and Group, L. E. (2006b). Magnetic field structure and confinement of energetic particles in the LHD. *Nucl. Fusion*, 46(2):291–305.
- Yoshinuma, M., Ida, K., Yokoyama, M., Osakabe, M., and Nagaoka, K. (2010). Charge-exchange Spectroscopy with the Pitch-controlled double-slit Fiber bundle on LHD. *Fusion Sci. Technol.*, 58:375–382.

Publications and Presentations

My publications

1. X.D. Du, S. Ohdachi, K. Toi and LHD Experiment Group,
"Development of an Array System of Soft X-ray Detectors with Large Sensitive Area on the Large Helical Device",
Plasma and Fusion Research, Vol. 7, No. 2401088, pp. 1 - 3, May, 2012
2. X.D. Du, K. Toi, M. Osakabe, S. Ohdachi, T. Ido, K. Tanaka, M. Yokoyama, M. Yoshinuma, K. Ogawa, K.Y. Watanabe, M. Isobe, K. Nagaoka, T. Ozaki, S. Sakakaibra, R. Seki, A. Shimizu, Y. Suzuki, H. Tsuchiya, and LHD experiment Group,
"Resistive Interchange Mode Destabilized by Helically Trapped Energetic Ions in a Helical Plasma",
Physical Review Letters, Vol. 114, No. 155003, pp. 1 - 5, April, 2015
3. X.D. Du, K. Toi, M. Osakabe, S. Ohdachi, T. Ido, K. Tanaka, M. Yokoyama, M. Yoshinuma, K. Ogawa, K.Y. Watanabe, M. Isobe, K. Nagaoka, T. Ozaki, S. Sakakaibra, R. Seki, A. Shimizu, Y. Suzuki, H. Tsuchiya, and LHD experiment Group,
"Resistive Interchange Mode Destabilized by Helically Trapped Energetic Ions and its Effects on Energetic Ions and Bulk Plasmas in LHD"
Proceeding of 25th IAEA Fusion Energy Conference, Russia, October, 2014
4. X.D. Du, K. Toi, M. Osakabe, S. Ohdachi, T. Ido, K. Tanaka, M. Yokoyama, M. Yoshinuma, K. Ogawa, K.Y. Watanabe, M. Isobe, K. Nagaoka, T. Ozaki, S. Sakakaibra, R. Seki, A. Shimizu, Y. Suzuki, H. Tsuchiya, and LHD experiment Group,
"Resistive Interchange Mode Destabilized by Helically Trapped Energetic Ions and its Effects on Energetic Ions and Bulk Plasmas in a Helical Plasma"
Nuclear Fusion, Vol. 56, No. 016002, pp. 1-16, 2016

Conference presentations

1. X.D. Du, K. Toi, S. Ohdachi and LHD Experiment Group,
"Frequency-Jump Phenomena in Edge MHD modes excited in LHD plasmas with Edge Transport Barrier." (poster),
8th General Scientific Assembly of the Asia Plasma and Fusion Association in 2011.
2. Xiaodi Du, S. Ohdachi, K. Toi and LHD Experiment Group,
"Development of an Array System of Ultra-Soft X-ray Detectors with Large Sensitive Area on the Large Helical Device (LHD)" (poster),
21th International Toki Conference, Toki, 2011.
3. X.D. Du, K. Toi, S. Ohdachi, M. Osakabe, K. Nagaoka, K. Ida, M. Yoshinuma, K. Ogawa, M. Isobe, S. Sakakibara, Y. Suzuki, N. Shi and LHD Experiment Group,
"The First Observation of off-axis Fishbone-like instabilities in High Ti plasma of LHD" (Oral),
68th Annual Meeting of the Physical Society of Japan, 2013.
4. Xiaodi Du, K. TOI, S. Ohdachi and LHD Experiment Group,
"First Observation of Fishbone-like Modes Driven by Helical-Ripple Trapped Fast Ions on LHD" (Oral),
13th IAEA Technical Meeting on Energetic Particles in Magnetic Confinement Systems, Beijing, 2013.
5. X.D. Du, K. Toi, M. Osakabe, S. Ohdachi, T. Ido, K. Tanaka, M. Yokoyama, M. Yoshinuma, K. Ogawa, K.Y. Watanabe, M. Isobe, K. Nagaoka, T. Ozaki, S. Sakakaibra, R. Seki, A. Shimizu, Y. Suzuki, H. Tsuchiya, and LHD experiment Group,
"Resistive Interchange Mode Destabilized by Helically Trapped Energetic Ions and its Effects on Energetic Ions and Bulk Plasmas in LHD" (poster),
25th IAEA Fusion Energy Conference, Russia, October, 2014.
6. X.D. Du, K. Toi, M. Osakabe, S. Ohdachi, T. Ido, K. Tanaka, M. Yokoyama, M. Yoshinuma, K. Ogawa, K.Y. Watanabe, M. Isobe, K. Nagaoka, T. Ozaki, S. Sakakaibra,

R. Seki, A. Shimizu, Y. Suzuki, H. Tsuchiya, and LHD experiment Group,
"Resistive Interchange Mode Destabilized by Helically Trapped Energetic Ions and its
Effects on Energetic Ions and Bulk Plasmas in LHD" (invited),
*14th IAEA Technical Meeting on Energetic Particles in Magnetic Confinement Sys-
tems, Vienna, 2015.*

Appendix A

Internal kink mode driven by Trapped Energetic Particles in tokamak

The internal kink mode driven by trapped energetic ions is firstly observed in PDX tokamak with nearly perpendicular neutral beam injection. Soon later, the theoretical analysis is well developed by L. Chen, R.B. White and M.N. Rosebluth in 1984 (Chen et al., 1984). In their theory, the bulk plasma is treated by the ideal MHD theory and the beam component is described by the gyrokinetic equation. The plasma displacement ξ_r for internal kink mode is assumed to be constant for $0 < r < r_s$ and $\xi_r = 0$ for $r > r_s$. A model distribution function $f_0 \propto E^{-3/2}$ for the slowing-down beam ions is adopted to get the analytical result. It is found that when the internal kink mode is marginally stable, the instability can be driven if the gradient of beam beta exceeds the critical value.

In LHD, the helically trapped energetic ions driven resistive interchange mode is discovered recently. Although the theoretical analysis is still under discussion, the theory is expected to be quite similar with the previously developed theory for fishbone mode. In this chapter, we firstly review the existing theory on collective instability driven by energetic particles, i.e., "Fishbone". Then the theoretical analysis is conducted for the interchange mode driven by helically trapped energetic ions in LHD. In this analysis, a quite localized even mode structure having Gaussian shape is taken into account for interchange mode based on the observed plasma displacement in real experiment (Du et al., 2015).

$$\xi_r = A_m \exp\left(-\frac{(r-r_s)^2}{\Delta^2}\right) \cos(m\theta - n\phi - \omega t), \quad (\text{A.1})$$

where A_m is the amplitude of the mode, r_s is the mode rational surface, Δ is the width of the mode, m and n is the poloidal and toroidal mode number (in present case, $m = 1/n = 1$) and

ω is the mode frequency in plasma frame. We also assume the distribution function of the beam is,

$$f_0 = c_0 \frac{\delta(\lambda - \lambda_0)}{E^{3/2}}, \quad (\text{A.2})$$

where the λ_0 is the initial pitch angle between the beam and the magnetic field line. The result clearly indicates that a certain threshold of gradient of beam beta is critical to excite the resistive interchange mode by helically trapped energetic ions.

A.1 Energy principle including hot component

The equation of motion gives,

$$\rho_m \frac{\partial \mathbf{u}}{\partial t} = -\nabla \cdot \mathbf{P} + \mathbf{j} \times \mathbf{B} \quad (\text{A.3})$$

The first-order linearized equations are,

$$-\rho_m \omega^2 \xi = -\nabla \cdot \tilde{\mathbf{P}}_h - \nabla \cdot \tilde{\mathbf{P}}_b + \mathbf{j} \times \tilde{\mathbf{B}} + \tilde{\mathbf{j}} \times \mathbf{B} \quad (\text{A.4})$$

where a normal mode $\xi(\mathbf{r}, t) = \xi(\mathbf{r}) \exp(-i\omega t)$ is considered. \tilde{P}_h and \tilde{P}_b is the first order pressure perturbation of the hot component and bulk component of plasma, respectively. The following ideal MHD relations holds:

$$\tilde{\mathbf{E}}_\perp = i\omega \xi \times \mathbf{B}_0, \quad \tilde{\mathbf{E}}_\parallel = 0, \quad \tilde{\mathbf{B}} = \nabla \times (\xi \times \mathbf{B}_0)$$

By multiplying $\frac{1}{2} \int d\mathbf{r} \xi^*$ on the eq. (A.4), we have

$$\delta I + \delta W_{MHD} + \delta W_k = 0 \quad (\text{A.5})$$

where,

$$\delta I = -\frac{\omega^2}{2} \int \rho_m |\xi|^2 d\mathbf{r} \quad (\text{A.6})$$

$$\delta W_k = \frac{1}{2} \int \xi \cdot \nabla \cdot \tilde{\mathbf{P}}_h d\mathbf{r} \quad (\text{A.7})$$

For internal kink mode the above equation can be simplified as followings (Chen et al., 1984),

$$\delta W_{MHD} + \delta I = 2\pi R \frac{B_{\theta s}^2}{2\mu_0} |\xi_s|^2 \left(\delta W^T + \gamma \tau_{A\theta} \frac{s}{2} \right) \quad (\text{A.8})$$

A.2 Kinetic integral of hot component

A.2.1 Drift-kinetic equation

We presume that the distribution function f is expressed in terms of the Cartesian phase-space variables; nevertheless, the generalization to arbitrary coordinates is straightforward. The change of distribution function along a particle trajectory is:

$$f[x(t), v(t), t] - f[x(t - \Delta t), v(t - \Delta t), t - \Delta t] \quad (\text{A.9})$$

The difference can be given in a more general way when the trajectories are express in terms of non-Cartesian coordinates, $z^i, i = 1, \dots, 6$: $f[z^i(t), t] - f[z^i(t - \Delta t), t - \Delta t]$, Therefore, we obtain the kinetic equation in in a collisionless limit as,

$$\frac{\partial f}{\partial t} + \frac{dz^i}{dt} \frac{\partial f}{\partial z^i} = 0 \quad (\text{A.10})$$

where a sum over the repeated index is implied. The z^i can be any smooth functions of x and v , as long as the transformation $(x, v) \rightarrow z^i$ is nonsingular.

A kinetic equation describing magnetized plasma motions can be simplified by suppressing details of the short scale-length of gyration, i.e., average over the gyro-scale. When the orbit of a gyrating particle is averaged in this way, what survives is so-called guiding center motion as,

$$\mathbf{v}_{gc} = v_{\parallel} \mathbf{b} + \mathbf{v}_D \quad (\text{A.11})$$

$$\mathbf{v}_D = \frac{\mathbf{E} \times \mathbf{b}_0}{B_0} + \frac{1}{\Omega} \mathbf{b} \times \left(\frac{\mu}{m} \nabla B + v_{\parallel}^2 \boldsymbol{\kappa} + v_{\parallel} \frac{\partial \mathbf{b}}{\partial t} \right) \quad (\text{A.12})$$

where, Ω is the gyro-frequency, $\mathbf{B} = B\mathbf{b}$, $\boldsymbol{\kappa} = \mathbf{b} \cdot \nabla \mathbf{b}$ is the magnetic curvature, μ is the magnetic momentum $\mu \equiv mv_{\perp}^2/2B$. Each guiding center can be specified by its position, magnetic momentum and energy, that is, the $(t, \mathbf{x}, v_x, v_y, v_z)$ can be replaced by an alternative phase space $(t, \mathbf{x}, U, \mu, \gamma)$, where U is the total guiding center energy for one particle and γ is

the phase angle of the particle velocity.

$$U = \frac{mv_{\parallel}^2}{2} + \mu B + e\phi \quad (\text{A.13})$$

Note that the gyrophase average suppresses the dependence on pitch angle of the gyromotion and the kinetic eq. (A.10) can be simplified to a form of equation for the gyrophase independent distribution function \bar{f} , i.e., drift-kinetic equation. For example, in the collisionless limit, as,

$$\frac{\partial f}{\partial t} + \mathbf{v}_{\text{gc}} \cdot \frac{\partial f}{\partial \mathbf{x}} + \frac{dU}{dt} \frac{\partial f}{\partial U} + \frac{d\mu}{dt} \frac{\partial f}{\partial \mu} = 0 \quad (\text{A.14})$$

Considering μ is conserved following the guiding center trajectory,

$$\frac{d\mu}{dt} = 0 \quad (\text{A.15})$$

Meanwhile,

$$\frac{dU}{dt} = \mathbf{v}_{\text{gc}} \cdot (e\mathbf{E} + \mathbf{F}_{\text{m}}) + e \frac{d\phi}{dt} + \mu \frac{dB}{dt} \quad (\text{A.16})$$

Here, \mathbf{F}_{m} is the mirror force as,

$$\mathbf{F}_{\text{m}} = -\nabla(\mu B) \quad (\text{A.17})$$

\mathbf{E} is the electrodynamic field as,

$$\mathbf{E} = -\nabla\phi - \frac{\partial \mathbf{A}}{\partial t} \quad (\text{A.18})$$

where, \mathbf{A} is the the vector potential, one can recover Faraday's law of induction by taking the curl of that equation,

$$\nabla \times \mathbf{E} = -\nabla \times (\nabla\phi) - \frac{\partial (\nabla \times \mathbf{A})}{\partial t} = -\frac{\partial \mathbf{B}}{\partial t} \quad (\text{A.19})$$

Substituting eq. (A.17) and eq. (A.18) into eq. (A.16),

$$\frac{dU}{dt} = \left(-e\mathbf{v}_{\text{gc}} \cdot \nabla\phi - e\mathbf{v}_{\text{gc}} \cdot \frac{\partial \mathbf{A}}{\partial t} - \mathbf{v}_{\text{gc}} \cdot \nabla(\mu B) \right) + \left(e \frac{\partial \phi}{\partial t} + e\mathbf{v}_{\text{gc}} \cdot \nabla\phi \right) + \left(\mu \frac{\partial B}{\partial t} + \mu \mathbf{v}_{\text{gc}} \cdot \nabla B \right) \quad (\text{A.20})$$

$$= e \frac{\partial \phi}{\partial t} + \mu \frac{\partial B}{\partial t} - e \mathbf{v}_{gc} \cdot \frac{\partial \mathbf{A}}{\partial t} \quad (\text{A.21})$$

The further simplification can be made for,

$$\frac{\partial B_0}{\partial t} = 0 \quad (\text{A.22})$$

because, the gyrokinetic theory concerns instability, not transport and interesting instabilities can be presumed to evolve rapidly compared with the transport time scale. Finally, the drift-kinetic equation is given as follows in collisionless limit,

$$\frac{\partial f}{\partial t} + \mathbf{v}_{gc} \cdot \frac{\partial f}{\partial \mathbf{x}} + \left(e \frac{\partial \phi}{\partial t} - e \mathbf{v}_{gc} \cdot \frac{\partial \mathbf{A}}{\partial t} \right) \frac{\partial f}{\partial U} = 0 \quad (\text{A.23})$$

A.2.2 Linearizion of drift-kinetic equaiton

The distribution function f by the gyrophase average can be separated into the equilibrium component and perturbation component as,

$$f = f_0(x, U) + f_1(t, x, U) \quad (\text{A.24})$$

where the equilibrium component f_0 is not the function of the time. The magnetic field \mathbf{B} is as,

$$\mathbf{B} = \mathbf{B}_0 + \mathbf{B}_1 \quad (\text{A.25})$$

where,

$$\mathbf{B}_1 = \nabla \times \mathbf{A}_1 = \nabla \times (A_1 \mathbf{b}_0) = \nabla A_1 \times \mathbf{b}_0 \quad (\text{A.26})$$

where B_0 is the equilibrium magnetic field, B_1 is the magnetic field perturbation, $\mathbf{A}_1 \equiv A_1 \mathbf{b}_0$ is the magnetic vector potential perturbation and \mathbf{b}_0 is the unit vector parallel to the equilibrium magnetic field. Note that the direction of the magnetic vector \mathbf{A} can be arbitrary, i.e. the same direction with magnetic field \mathbf{b}_0 , since $\mathbf{B} = \nabla \times \mathbf{A} \equiv \nabla \times (\mathbf{A} + \nabla m)$, where ∇m is an arbitrary vector. For simplicity, we neglect the background electric field veE , that is,

$$\mathbf{E} \equiv E_1 = -\nabla \phi_1 - \frac{\partial \mathbf{A}_1}{\partial t} \quad (\text{A.27})$$

where \mathbf{E}_1 is the electric field perturbation and ϕ_1 is the electrostatic potential perturbation. The \mathbf{v}_{gc} is linearized as follows,

$$\mathbf{v}_{gc} = \mathbf{v}_{gc0} + \mathbf{v}_{gc1} \quad (\text{A.28})$$

where,

$$\mathbf{v}_{gc0} = \mathbf{v}_{\parallel 0} + \mathbf{v}_{d0} = v_{\parallel} \mathbf{b}_0 + \mathbf{v}_m \quad (\text{A.29})$$

$$\mathbf{v}_{gc1} = \mathbf{v}_{\parallel 1} + \mathbf{v}_{d1} = v_{\parallel} \frac{\nabla A_1 \times \mathbf{b}_0}{B_0} - \frac{\nabla \phi_1 \times \mathbf{b}_0}{B_0} \quad (\text{A.30})$$

Here,

$$\mathbf{v}_{d1} = \frac{\mathbf{E}_1 \times \mathbf{b}_0}{B_0} = \frac{1}{B_0} \left(-\nabla \phi_1 - \frac{\partial \mathbf{A}_1}{\partial t} \right) \times \mathbf{b}_0 = -\frac{\nabla \phi_1 \times \mathbf{b}_0}{B_0} \quad (\text{A.31})$$

Note that here we only consider the perturbed drift motion comes from the $E_1 \times B_0$ drift for simplicity. This assumption is reasonable because the energy exchange between the particles and the waves is mainly due to the electric potential and is not due to the change of the magnetic field. The magnetic field only changes the orbit motion of the particle but not the total energy. That is, the drift motion \mathbf{v}_m is taken as the equilibrium term. Moreover, since the $E_0 = 0$ is assumed, the $\mathbf{v}_{E_0 \times B_0}$ is neglected. The first order of eq. (A.23) is given by,

$$\frac{\partial f_1}{\partial t} + \mathbf{v}_{gc0} \cdot \frac{\partial f_1}{\partial \mathbf{x}} + \mathbf{v}_{gc1} \cdot \frac{\partial f_0}{\partial \mathbf{x}} + \left(e \frac{\partial \phi_1}{\partial t} - e \mathbf{v}_{gc0} \cdot \frac{\partial \mathbf{A}_1}{\partial t} \right) \frac{\partial f_0}{\partial U_0} = 0 \quad (\text{A.32})$$

$$\frac{\partial f_1}{\partial t} + (v_{\parallel} \mathbf{b}_0 + \mathbf{v}_m) \cdot \nabla f_1 + \left(v_{\parallel} \frac{\nabla A_1 \times \mathbf{b}_0}{B_0} - \frac{\nabla \phi_1 \times \mathbf{b}_0}{B_0} \right) \cdot \nabla f_0 + \left(e \frac{\partial \phi_1}{\partial t} - e v_{\parallel} \cdot \frac{\partial \mathbf{A}_1}{\partial t} \right) \frac{\partial f_0}{\partial U_0} = 0 \quad (\text{A.33})$$

To get the analytical solution for the drift-kinetic equation, we assume that electromagnetic perturbations are approximated by plane waves with rotation frequency ω and perpendicular wave vector k_{\perp} , we also assume that the time and perpendicular spatial dependence of f_1 are the same as those of electromagnetic perturbations. Then, the equation evolves into,

$$-i\omega f_1 + v_{\parallel} \frac{\partial f_1}{\partial l} + i\mathbf{k} \cdot \mathbf{v}_m f_1 + \left(v_{\parallel} \frac{A_1}{B_0} i\mathbf{k} \times \mathbf{b}_0 - \frac{\phi_1}{B_0} i\mathbf{k} \times \mathbf{b}_0 \right) \cdot \nabla f_0 + (-i\omega e \phi_1 + e v_{\parallel} i\omega A_1) \frac{\partial f_0}{\partial U_0} = 0 \quad (\text{A.34})$$

Straightforward calculation shows the following equation,

$$-i(\omega - \omega_d) f_1 + v_{\parallel} \frac{\partial f_1}{\partial l} + \frac{i \mathbf{k} \times \mathbf{b}_0 \cdot \nabla f_0}{B_0} (v_{\parallel} A_1 - \phi_1) + ie\omega (v_{\parallel} A_1 - \phi_1) \frac{\partial f_0}{\partial U_0} = 0 \quad (\text{A.35})$$

$$-i(\omega - \omega_d) f_1 + v_{\parallel} \frac{\partial f_1}{\partial l} + i(v_{\parallel} A_1 - \phi_1) \left(\frac{\mathbf{k} \times \mathbf{b}_0 \cdot \nabla f_0}{B_0} + e\omega \frac{\partial f_0}{\partial U_0} \right) = 0 \quad (\text{A.36})$$

with,

$$\omega_d = \mathbf{k} \cdot \mathbf{v}_m \quad (\text{A.37})$$

For ideal MHD theory, the parallel Ohm's law $\mathbf{E} + \mathbf{v} \times \mathbf{B} = 0$, requiring $\mathbf{E}_1 \cdot \mathbf{b}_0 = 0$. This means that the perturbation of the electric field induced by the instability must be perpendicular to the magnetic field line, that is,

$$\mathbf{E}_1 \cdot \mathbf{b}_0 = -(\mathbf{b}_0 \cdot \nabla) \phi_1 - \frac{\partial A_1}{\partial t} \equiv 0 \quad (\text{A.38})$$

$$-\frac{\partial \phi_1}{\partial l} - \frac{\partial A_1}{\partial t} = 0 \quad (\text{A.39})$$

$$A_1 = \frac{1}{i\omega} \frac{\partial \phi_1}{\partial l} \quad (\text{A.40})$$

In addition, we define,

$$Q \equiv \frac{\mathbf{k} \times \mathbf{b}_0 \cdot \nabla f_0}{eB_0} + \omega \frac{\partial f_0}{\partial U_0} \quad (\text{A.41})$$

Substituting eq. (A.40) and eq. (A.41) into eq. (A.36),

$$-i(\omega - \omega_d) f_1 + v_{\parallel} \frac{\partial f_1}{\partial l} + i \left(v_{\parallel} \frac{1}{i\omega} \frac{\partial \phi_1}{\partial l} - \phi_1 \right) eQ = 0 \quad (\text{A.42})$$

$$-i(\omega - \omega_d) f_1 + v_{\parallel} \frac{\partial f_1}{\partial l} + v_{\parallel} \frac{eQ}{\omega} \frac{\partial \phi_1}{\partial l} - ieQ\phi_1 = 0 \quad (\text{A.43})$$

A.2.3 The approximate solution for the drift-kinetic equation

To solve the above equation approximately, we assume that $\partial Q / \partial l \sim 0$, based on the consideration that the equilibrium quantities have long scale lengths in the parallel direction

for the perturbations. The equation can be reformed as,

$$-i\omega \left(f_1 + \frac{eQ}{\omega} \phi_1 \right) + v_{\parallel} \frac{\partial}{\partial l} \left(f_1 + \frac{eQ}{\omega} \phi_1 \right) + i\omega_d f_1 = 0 \quad (\text{A.44})$$

By observing the eq. (A.44), the solution is naturally to have the form as,

$$f_1 = -\frac{eQ}{\omega} \phi_1 + g_1 \quad (\text{A.45})$$

Substituting the eq. (A.45) to the eq. (A.44), we have,

$$-i\omega g_1 + v_{\parallel} \frac{\partial}{\partial l} g_1 + i\omega_d \left(-\frac{eQ}{\omega} \phi_1 + g_1 \right) = 0 \quad (\text{A.46})$$

This can be rewritten as,

$$-i(\omega - \omega_d) g_1 + v_{\parallel} \frac{\partial g_1}{\partial l} - ieQ \frac{\omega_d}{\omega} \phi_1 = 0 \quad (\text{A.47})$$

Then the orbital average is considered as,

$$\langle C \rangle = \frac{1}{\tau_b} \oint C dt = \frac{1}{\tau_b} \oint \frac{C}{v_{\parallel}} dl \quad (\text{A.48})$$

For trapped particles which do the bounce motion in the very narrow region, i.e., helical ripple, the terms with v_{\parallel} are suppressed by the orbital average. Therefore, the eq. (A.47) is approximated by,

$$-i(\omega - \langle \omega_d \rangle) \langle g_1 \rangle = ieQ \frac{\langle \omega_d \rangle}{\omega} \phi_1 \quad (\text{A.49})$$

$$\langle g_1 \rangle = -\frac{eQ}{\omega - \langle \omega_d \rangle} \frac{\langle \omega_d \rangle}{\omega} \phi_1 \quad (\text{A.50})$$

Finally, we obtain f_1 as,

$$f_1 = -\frac{eQ}{\omega} \phi_1 - \frac{eQ}{\omega - \langle \omega_d \rangle} \frac{\langle \omega_d \rangle}{\omega} \phi_1 \quad (\text{A.51})$$

$$= -\frac{e\phi_1}{\omega} \left(\frac{\mathbf{k} \times \mathbf{b}_0 \cdot \nabla f_0}{eB_0} + \omega \frac{\partial f_0}{\partial U_0} \right) - \frac{eQ}{\omega - \langle \omega_d \rangle} \frac{\langle \omega_d \rangle}{\omega} \phi_1 \quad (\text{A.52})$$

$$= -\frac{1}{\omega B_0} (\mathbf{k} \times \mathbf{b}_0 \cdot \nabla f_0) \phi_1 - \frac{eQ}{\omega - \langle \omega_d \rangle} \frac{\langle \omega_d \rangle}{\omega} \phi_1 \quad (\text{A.53})$$

If we introduce the displacement vector as,

$$\xi_{\perp} = \int \mathbf{v}_{1\perp} dt \quad (\text{A.54})$$

$$= \int -\frac{\nabla \phi_1 \times \mathbf{b}_0}{B_0} dt \quad (\text{A.55})$$

$$= -\frac{i\mathbf{k} \times \mathbf{b}_0}{B_0} \int \phi_1 dt \quad (\text{A.56})$$

$$= -\frac{i\mathbf{k} \times \mathbf{b}_0}{B_0} \frac{\phi_1}{-i\omega} \quad (\text{A.57})$$

$$= \frac{\mathbf{k} \times \mathbf{b}_0}{\omega B_0} \phi_1 \quad (\text{A.58})$$

and,

$$\frac{\langle \omega_d \rangle}{\omega} \phi_1 = \frac{\phi_1}{\omega} \mathbf{k}_{\perp} \cdot \frac{1}{eB_0} \mathbf{b} \times \left(mv_{\parallel}^2 + \frac{mv_{\perp}^2}{2} \right) \boldsymbol{\kappa} \quad (\text{A.59})$$

$$= \frac{1}{e} \left(mv_{\parallel}^2 + \frac{mv_{\perp}^2}{2} \right) \frac{(\mathbf{k}_{\perp} \times \mathbf{b}_0 \cdot \boldsymbol{\kappa})}{\omega B_0} \phi_1 \quad (\text{A.60})$$

$$= \frac{1}{e} \left(mv_{\parallel}^2 + \frac{mv_{\perp}^2}{2} \right) (\xi_{\perp} \cdot \boldsymbol{\kappa}) \quad (\text{A.61})$$

$$\equiv -\frac{Jmv^2}{e} = -\frac{2JE}{e} \quad (\text{A.62})$$

where we define,

$$J \equiv -\frac{v_{\parallel}^2 + v_{\perp}^2/2}{v^2} (\boldsymbol{\kappa} \cdot \boldsymbol{\xi}) \quad (\text{A.63})$$

Therefore, eq. (A.53) is reformed as,

$$f_1 = -(\xi_{\perp} \cdot \nabla f_0) + \frac{2JQE}{\omega - \langle \omega_d \rangle} \quad (\text{A.64})$$

A.2.4 Pressure Perturbation by the trapped fast ions

Taking the second central momentum with respect to average velocity, i.e, fluid velocity \mathbf{V} gives the pressure tensor,

$$P \equiv \int m(\mathbf{v} - \mathbf{V})(\mathbf{v} - \mathbf{V}) f d^3\mathbf{v} \quad (\text{A.65})$$

where the fluid velocity V is the first velocity momentum of f as,

$$\mathbf{V} = \frac{\int \mathbf{v} f d\mathbf{v}}{\int f d\mathbf{v}} = \frac{\int \mathbf{v} f d\mathbf{v}}{n} \quad (\text{A.66})$$

Since the fluid velocity is much smaller than the particle velocity, the pressure tensor is approximated by,

$$P \equiv \int m \mathbf{v} \mathbf{v} f d^3 \mathbf{v} \quad (\text{A.67})$$

The tensor can $\mathbf{v} \mathbf{v}$ can be expanded into,

$$\begin{pmatrix} v_x v_x & v_x v_y & v_x v_z \\ v_y v_x & v_y v_y & v_y v_z \\ v_z v_x & v_z v_y & v_z v_z \end{pmatrix} \quad (\text{A.68})$$

when the magnetic field is applied in the system, the particle velocity can be rewritten as $\mathbf{v} = \mathbf{v}_{\parallel} + \mathbf{v}_{\perp}$. Without loss of generality we define,

$$\mathbf{v}_z \equiv \mathbf{v}_{\parallel} \quad (\text{A.69})$$

$$v_x = v_{\perp} \cos \gamma \quad (\text{A.70})$$

$$v_y = v_{\perp} \sin \gamma \quad (\text{A.71})$$

where γ is the gyro-phase angle of the particle, then the tensor $\mathbf{v} \mathbf{v}$ can be expressed as,

$$\begin{pmatrix} \langle v_{\perp}^2 \cos^2 \gamma \rangle & \langle v_{\perp}^2 \cos \gamma \sin \gamma \rangle & \langle v_{\perp} v_{\parallel} \cos \gamma \rangle \\ \langle v_{\perp}^2 \cos \gamma \sin \gamma \rangle & \langle v_{\perp}^2 \sin^2 \gamma \rangle & \langle v_{\perp} v_{\parallel} \sin \gamma \rangle \\ \langle v_{\perp} v_{\parallel} \cos \gamma \rangle & \langle v_{\perp} v_{\parallel} \sin \gamma \rangle & \langle v_{\parallel}^2 \rangle \end{pmatrix} = \begin{pmatrix} v_{\perp}^2/2 & 0 & 0 \\ 0 & v_{\perp}^2/2 & 0 \\ 0 & 0 & v_{\parallel}^2 \end{pmatrix} \quad (\text{A.72})$$

where,

$$\langle g \rangle = \int_0^{2\pi} g d\gamma / \int_0^{2\pi} d\gamma \quad (\text{A.73})$$

Therefore, the pressure tensor when the magnetic field line is applied appears as the familiar form as follows,

$$P = p_{\perp}(\mathbf{I} - \mathbf{b}\mathbf{b}) + p_{\parallel} \mathbf{b}\mathbf{b} \quad (\text{A.74})$$

where,

$$p_{\perp} = \int \frac{mv_{\perp}^2}{2} f d^3\mathbf{v} \quad (\text{A.75})$$

$$p_{\parallel} = \int mv_{\parallel}^2 f d^3\mathbf{v} \quad (\text{A.76})$$

It should be noted that $d^3\mathbf{v} = 2\pi v_{\perp} dv_{\perp} dv_{\parallel}$ in the simple cylinder coordinate. The pressure tensor perturbation by the perturbation of distribution function is considered to be δp_{\parallel} and δp_{\perp} , as follows,

$$\delta p_{\parallel} = \pi \int mv_{\parallel}^2 f_1 dv_{\perp}^2 dv_{\parallel} \quad (\text{A.77})$$

$$\delta p_{\perp} = \pi \int \frac{mv_{\perp}^2}{2} f_1 dv_{\perp}^2 dv_{\parallel} \quad (\text{A.78})$$

To get the simple form, hereafter we will use the set (λ, E, γ) instead of the (μ, U, γ) , which provides the orthogonal coordinates in velocity space. λ is the pitch-angle variable and defined by,

$$\lambda \equiv \frac{\mu}{E} = \frac{mv_{\perp}^2}{2B_0} / \frac{mv^2}{2} = \frac{1}{B_0} \frac{v_{\perp}^2}{v^2} \quad (\text{A.79})$$

Therefore,

$$v_{\perp}^2 = \frac{2B_0\mu}{m} = \frac{2B_0}{m} \lambda E \quad (\text{A.80})$$

$$v_{\parallel}^2 = v^2 - v_{\perp}^2 = \frac{2E}{m} (1 - \lambda B_0) \quad (\text{A.81})$$

Then transfer $(v_{\perp}^2, v_{\parallel})$ to (λ, E) ,

$$dv_{\perp}^2 dv_{\parallel} = \frac{1}{2v_{\parallel}} dv_{\perp}^2 dv_{\parallel}^2 \quad (\text{A.82})$$

$$= \frac{1}{2v_{\parallel}} \begin{vmatrix} \frac{\partial v_{\perp}^2}{\partial \lambda} & \frac{\partial v_{\perp}^2}{\partial E} \\ \frac{\partial v_{\parallel}^2}{\partial \lambda} & \frac{\partial v_{\parallel}^2}{\partial E} \end{vmatrix} d\lambda dE \quad (\text{A.83})$$

$$= \frac{1}{2v_{\parallel}} \begin{vmatrix} (2B_0/m)E & (2B_0/m)\lambda \\ -(2B_0/m)E & 2(1 - \lambda B_0)/m \end{vmatrix} d\lambda dE \quad (\text{A.84})$$

$$= \frac{1}{2v_{\parallel}} \frac{4B_0E}{m^2} (1 - \lambda B_0 + \lambda B_0) d\lambda dE \quad (\text{A.85})$$

$$= \frac{2B_0 E}{v_{\parallel} m^2} d\lambda dE \quad (\text{A.86})$$

Since,

$$v_{\parallel} = \text{sgn}(v_{\parallel}) \sqrt{\frac{2E}{m}} (1 - \lambda B_0)^{1/2} \quad (\text{A.87})$$

then,

$$2\pi v_{\perp} dv_{\perp} dv_{\parallel} = \frac{\pi}{m^2} \frac{2B_0 E}{\text{sgn}(v_{\parallel}) \sqrt{\frac{2E}{m}} (1 - \lambda B_0)^{1/2}} d\lambda dE \quad (\text{A.88})$$

$$= \text{sgn}(v_{\parallel}) \sqrt{2} \pi m^{-3/2} \frac{E^{1/2}}{(1 - \lambda B_0)^{1/2}} d(\lambda B_0) dE \quad (\text{A.89})$$

Furthermore, the δp_{\perp} and δp_{\parallel} is given by,

$$\delta p_{\parallel} = \pi \int m v_{\parallel}^2 f_1 dv_{\perp}^2 dv_{\parallel} \quad (\text{A.90})$$

$$= \pi m^{-1/2} \text{sgn}(v_{\parallel}) \int \frac{2E}{m} (1 - \lambda B_0) f_1 \sqrt{2} \frac{E^{1/2}}{(1 - \lambda B_0)^{1/2}} d(\lambda B_0) dE \quad (\text{A.91})$$

$$= 2^{3/2} \pi m^{-3/2} \text{sgn}(v_{\parallel}) \int f_1 (1 - \lambda B_0)^{1/2} E^{3/2} d(\lambda B_0) dE \quad (\text{A.92})$$

and

$$\delta p_{\perp} = \pi \int \frac{m v_{\perp}^2}{2} f_1 dv_{\perp}^2 dv_{\parallel} \quad (\text{A.93})$$

$$= \pi \int B_0 \lambda E f_1 \text{sgn}(v_{\parallel}) \sqrt{2} m^{-3/2} \frac{E^{1/2}}{(1 - \lambda B_0)^{1/2}} d(\lambda B_0) dE \quad (\text{A.94})$$

$$= \sqrt{2} \pi m^{-3/2} \text{sgn}(v_{\parallel}) \int f_1 \frac{\lambda B_0}{(1 - \lambda B_0)^{1/2}} E^{3/2} d(\lambda B_0) dE \quad (\text{A.95})$$

To unify the expression to the popular the final expression in the L. Chen's paper, we re-define $E \equiv v^2/2$ hereafter instead of $E \equiv m v^2/2$. Then we re-write the equation as,

$$\delta p_{\parallel} = 2^{3/2} \pi m \int (1 - \lambda B_0)^{1/2} d(\lambda B_0) \int_0^{E_m} f_1 E^{3/2} dE \quad (\text{A.96})$$

$$\delta p_{\perp} = 2^{3/2} \pi m \int (1 - \lambda B_0)^{1/2} d(\lambda B_0) \int_0^{E_m} f_1 \frac{\lambda B_0}{2(1 - \lambda B_0)} E^{3/2} dE \quad (\text{A.97})$$

Substituting eq. (A.64) into δp_\perp and δp_\parallel yields,

$$\begin{pmatrix} \delta p_\perp \\ \delta p_\parallel \end{pmatrix} = 2^{5/2} \pi m \int (1 - \lambda B_0)^{1/2} d(\lambda B_0) \int_0^{E_m} dE \frac{E^{5/2} Q}{\omega - \langle \omega_{dh} \rangle} \bar{J} \begin{pmatrix} \lambda B_0/2 (1 - \lambda B_0) \\ 1 \end{pmatrix} \quad (\text{A.98})$$

A.2.5 Formulation of energy perturbation by the trapped EPs

The kinetic energy induced by the trapped EPs is proportional to the perpendicular plasma displacement times the force in that directions, yielding,

$$\delta W_k(\xi_\perp^*, \xi_\perp) = \frac{1}{2} \int \xi_\perp^* \cdot (\nabla \cdot \delta \mathbf{P}) dr \quad (\text{A.99})$$

where,

$$\xi_\perp^* \cdot (\nabla \cdot \delta \mathbf{P}) = \xi_\perp^* \cdot (\nabla \cdot \delta p_\perp (\mathbf{I} - \mathbf{b}\mathbf{b})) + \xi_\perp^* \cdot \nabla \cdot \delta p_\parallel \mathbf{b}\mathbf{b} \quad (\text{A.100})$$

$$= \xi_\perp^* \cdot (\nabla \cdot (\delta p_\perp \mathbf{I})) + \xi_\perp^* \cdot (\nabla \cdot (\delta p_\parallel - \delta p_\perp) \mathbf{b}\mathbf{b}) \quad (\text{A.101})$$

$$= \xi_\perp^* \cdot (\nabla \delta p_\perp \cdot \mathbf{I} + \delta p_\perp \nabla \cdot \mathbf{I}) + \xi_\perp^* \cdot (\nabla (\delta p_\parallel - \delta p_\perp) \cdot \mathbf{b}\mathbf{b} - (\delta p_\parallel - \delta p_\perp) \nabla \cdot \mathbf{b}\mathbf{b}) \quad (\text{A.102})$$

$$= \xi_\perp^* \cdot \nabla \delta p_\perp + (\xi_\perp^* \cdot \mathbf{b}) \nabla_\parallel (\delta p_\parallel - \delta p_\perp) + (\delta p_\parallel - \delta p_\perp) (\xi_\perp^* \cdot \nabla \cdot \mathbf{b}\mathbf{b}) \quad (\text{A.103})$$

$$= \xi_\perp^* \cdot \nabla \delta p_\perp + (\delta p_\parallel - \delta p_\perp) (\xi_\perp^* \cdot ((\nabla \cdot \mathbf{b}) \mathbf{b} + \mathbf{b} \cdot \nabla \mathbf{b})) \quad (\text{A.104})$$

$$= \xi_\perp^* \cdot \nabla \delta p_\perp + (\delta p_\parallel - \delta p_\perp) (\xi_\perp^* \cdot \boldsymbol{\kappa}) \quad (\text{A.105})$$

Then we have

$$\delta W_k(\xi_\perp^*, \xi_\perp) = \frac{1}{2} \int (\xi_\perp^* \cdot \nabla \delta p_\perp + (\delta p_\parallel - \delta p_\perp) (\xi_\perp^* \cdot \boldsymbol{\kappa})) dr \quad (\text{A.106})$$

$$= \frac{1}{2} \int (\nabla \cdot (\xi_\perp^* \delta p_\perp) - \delta p_\perp (\nabla \cdot \xi_\perp^*) + (\delta p_\parallel - \delta p_\perp) (\xi_\perp^* \cdot \boldsymbol{\kappa})) dr \quad (\text{A.107})$$

$$= -\frac{1}{2} \int (\delta p_\perp (\nabla \cdot \xi_\perp^*) - (\delta p_\parallel - \delta p_\perp) (\xi_\perp^* \cdot \boldsymbol{\kappa})) dr \quad (\text{A.108})$$

Substituting eq. (A.98) into the above equation yields,

$$\delta W_k(\xi_\perp^*, \xi_\perp) \quad (\text{A.109})$$

$$= -2^{3/2} \pi m \int d\mathbf{r} d(\lambda B_0) dE \frac{E^{3/2}}{(1 - \lambda B_0)^{1/2}} \left((\nabla \cdot \xi_\perp^*) \frac{v_\perp^2}{2v^2} - (\xi_\perp^* \cdot \boldsymbol{\kappa}) \frac{v_\parallel^2 - v_\perp^2/2}{v^2} \right) f_1 \quad (\text{A.110})$$

Reminding the previous derivation for ξ_{\perp} as,

$$\xi_{\perp} = \int \mathbf{v}_{1\perp} dt \quad (\text{A.111})$$

$$= \int -\frac{\nabla\phi_1 \times \mathbf{b}_0}{B_0} dt \quad (\text{A.112})$$

$$= \frac{1}{i\omega B_0} \nabla\phi_1 \times \mathbf{b}_0 \quad (\text{A.113})$$

Then,

$$i\omega \nabla \cdot \xi_{\perp} = \nabla \cdot \left(\frac{\nabla\phi_1 \times \mathbf{b}_0}{B_0} \right) \quad (\text{A.114})$$

$$= \nabla \frac{1}{B_0} \cdot (\nabla\phi_1 \times \mathbf{b}_0) + \frac{1}{B_0} \nabla \cdot (\nabla\phi_1 \times \mathbf{b}_0) \quad (\text{A.115})$$

$$= -\frac{\nabla B_0}{B_0} \cdot \left(\frac{\nabla\phi_1 \times \mathbf{b}_0}{B_0} \right) + \frac{1}{B_0} (\mathbf{b}_0 \cdot \nabla \times \nabla\phi_1 - \nabla\phi_1 \cdot \nabla \times \mathbf{b}_0) \quad (\text{A.116})$$

$$= -\frac{\nabla B_0}{B_0} \cdot i\omega \xi_{\perp} - \frac{1}{B_0} (\nabla\phi_1 \cdot \nabla \times \mathbf{b}_0) \quad (\text{A.117})$$

$$= -i\omega (\kappa \cdot \xi_{\perp}) - \frac{\nabla\phi_1}{B_0} \cdot (\mathbf{b}_0 \times \kappa + \mathbf{b}_0 (\mathbf{b}_0 \cdot \nabla \times \mathbf{b}_0)) \quad (\text{A.118})$$

$$= -i\omega (\kappa \cdot \xi_{\perp}) - \kappa \cdot \left(\frac{\nabla\phi_1 \times \mathbf{b}_0}{B_0} \right) - \frac{1}{B_0} (\nabla\phi_1 \cdot \mathbf{b}_0) (\mathbf{b}_0 \cdot \nabla \times \mathbf{b}_0) \quad (\text{A.119})$$

$$= -2i\omega (\kappa \cdot \xi_{\perp}) - \frac{\nabla_{\parallel}\phi_1}{B_0} (\mathbf{b}_0 \cdot \nabla \times \mathbf{b}_0) \quad (\text{A.120})$$

$$= -2i\omega (\kappa \cdot \xi_{\perp}) + \mathcal{O}(\beta) \quad (\text{A.121})$$

where,

$$\frac{\nabla_{\parallel}\phi_1}{B_0} (\mathbf{b}_0 \cdot \nabla \times \mathbf{b}_0) \quad (\text{A.122})$$

$$= \frac{\nabla_{\parallel}\phi_1}{B_0} \left(\mathbf{b}_0 \cdot \nabla \times \frac{\mathbf{B}_0}{B_0} \right) \quad (\text{A.123})$$

$$= \frac{\nabla_{\parallel}\phi_1}{B_0} \left(\mathbf{b}_0 \cdot \left(\frac{1}{B_0} \nabla \times \mathbf{B}_0 - \mathbf{B}_0 \times \frac{\nabla B_0}{B_0^2} \right) \right) \quad (\text{A.124})$$

$$= \frac{\nabla_{\parallel}\phi_1}{B_0} \frac{\mu_0 J_{\parallel} \times B_0}{B_0^2} \quad (\text{A.125})$$

$$= \frac{\nabla_{\parallel}\phi_1}{B_0} \mathcal{O}(\beta) \quad (\text{A.126})$$

Finally, the δW_k can be reduced with substituting the eq. (A.64) and eq. (A.121),

$$\begin{aligned} & \frac{\delta W_k}{2\pi R} \\ &= -\frac{2^{3/2}\pi}{2\pi R} m \int d\mathbf{r} d(\lambda B_0) dE \frac{E^{3/2}}{(1-\lambda B_0)^{1/2}} \left(-2(\xi_{\perp}^* \cdot \kappa) \frac{v_{\perp}^2}{2v^2} - (\xi_{\perp}^* \cdot \kappa) \frac{v_{\parallel}^2 - v_{\perp}^2/2}{v^2} \right) f_1 \end{aligned} \quad (\text{A.127})$$

$$= -\frac{2^{3/2}\pi}{2\pi R} m \int d\mathbf{r} d(\lambda B_0) dE \frac{E^{3/2}}{(1-\lambda B_0)^{1/2}} \left(-\frac{v_{\parallel}^2 + v_{\perp}^2/2}{v^2} \right) (\xi_{\perp}^* \cdot \kappa) f_1 \quad (\text{A.128})$$

$$= -\frac{2^{3/2}\pi}{2\pi R} m \int d\mathbf{r} d(\lambda B_0) dE \frac{E^{3/2}}{(1-\lambda B_0)^{1/2}} \frac{2\bar{J}^* \bar{J} Q E}{\omega - \langle \omega_d \rangle} \quad (\text{A.129})$$

$$d\mathbf{r} = 2\pi R d\theta r dr \quad (\text{A.130})$$

Therefore,

$$\frac{\delta W_k}{2\pi R} = -2^{5/2} \pi^2 m \int r dr \int d(\lambda B_0) \int dE E^{5/2} K_b \frac{2\bar{J}^* \bar{J} Q}{\omega - \langle \omega_d \rangle} \quad (\text{A.131})$$

where

$$K_b = \oint \frac{d\theta}{2\pi} \frac{1}{(1-\lambda B_0)^{1/2}} \quad (\text{A.132})$$

Appendix B

Growth Rate of the fishbone instability in tokamak

We assume a model distribution function for slowing-down beam ions in the energy range $0 \leq E \leq E_m$ as,

$$f_0 = c_0 \frac{\delta(\lambda - \lambda_0)}{E^{3/2}} \quad (\text{B.1})$$

Then the pressure of the hot ions are as follows,

$$p_h = 2p_{\perp h} + p_{\parallel h} \quad (\text{B.2})$$

Then,

$$p_h = 2^{3/2} \pi m \int (1 - \lambda B_0)^{1/2} d(\lambda B_0) \int_0^{E_m} f_0 E^{3/2} \left(1 + \frac{2\lambda B}{2(1 - \lambda B)} \right) dE \quad (\text{B.3})$$

$$= 2^{3/2} \pi m \int d(\lambda B_0) \int_0^{E_m} f_0 \frac{E^{3/2}}{(1 - \lambda B)^{1/2}} dE \quad (\text{B.4})$$

$$= 2^{3/2} \pi m c_0 \int_0^{E_m} \frac{B}{(1 - \lambda_0 B)^{1/2}} dE \quad (\text{B.5})$$

$$= 2^{3/2} \pi m c_0 E_m B K_b \quad (\text{B.6})$$

Note that on the assumption of the f_0 , we have $K_b \equiv (1 - \lambda_0 B)^{-1/2}$ here. The density of hot ions n_h are,

$$n_h = \int_{T_c}^{E_m} 2^{3/2} \pi B \frac{E^{1/2}}{(1 - \lambda B)^{1/2}} d\lambda dE f_0 \quad (\text{B.7})$$

$$= 2^{3/2} \pi B K_b c_0 \int_{T_c}^{E_m} E^{-1} dE \quad (\text{B.8})$$

$$= \frac{p_h}{m E_m} \frac{\ln(E_m/T_c)}{E_m} \quad (\text{B.9})$$

Considering the trapped particles, $v_\perp \gg v_\parallel$

$$J \equiv -\frac{1}{2} (\kappa \cdot \xi) \approx -\frac{1}{2} \kappa_r \xi_r \approx -\frac{1}{2} \frac{\cos \theta \xi_r}{R} \quad (\text{B.10})$$

where we only consider antisymmetric circular tokamak $B_0 = \bar{B}_0 (1 - \frac{r}{R} \cos \theta)$. Note that κ should be averaged following the trapped region. Then the eq. (A.131) can be expanded into,

$$\frac{\delta W_k}{2\pi R} = -2^{5/2} \pi^2 m \int_0^{r_s} r dr \int_0^{E_m} dE E^{5/2} K_b \frac{1}{4} \frac{\cos^2 \theta \xi_r^2}{R^2} \frac{2Q}{\omega - \langle \omega_d \rangle} \quad (\text{B.11})$$

$$= -2^{3/2} \pi^2 m \frac{\xi_r^2}{R^2} \int_0^{r_s} r dr \int_0^{E_m} dE E^{5/2} K_b \cos^2 \theta \frac{Q}{\omega - \langle \omega_d \rangle} \quad (\text{B.12})$$

$$= -2^{3/2} \pi^2 m \frac{\xi_r^2}{R^2} \int_0^{r_s} r dr \int_0^{E_m} dE E^{5/2} \frac{K_2^2}{K_b} \frac{Q}{\omega - \langle \omega_d \rangle} \quad (\text{B.13})$$

where

$$K_2 = \oint \frac{d\theta}{2\pi} \frac{\cos \theta}{(1 - \lambda B)^{1/2}} \quad (\text{B.14})$$

$$\frac{K_2^2}{K_b} \equiv \oint \frac{d\theta}{2\pi} \frac{\cos^2 \theta}{(1 - \lambda B)^{1/2}} \quad (\text{B.15})$$

Remind that according to the definition of Q from the eq. (A.41),

$$Q \equiv \frac{\mathbf{k} \times \mathbf{b}_0 \cdot \nabla f_0}{e B_0} + \omega \frac{\partial f_0}{\partial E} \quad (\text{B.16})$$

$$\approx -\frac{1}{e B} \frac{m}{r} \frac{\partial f_0}{\partial r} + \omega \frac{\partial f_0}{\partial E} \quad (\text{B.17})$$

$$\approx -\frac{1}{e B} \frac{m}{r} \frac{\partial f_0}{\partial r} + \omega \frac{\partial f_0}{\partial E} \quad (\text{B.18})$$

In present case, substitute poloidal mode number $m = 1$ and f_0 into Q and yields,

$$Q = -\frac{1}{e B r} \frac{\partial c_0}{\partial r} E^{-3/2} - (3/2) \omega c_0 E^{-5/2} \quad (\text{B.19})$$

$$= -\frac{1}{eBr} \frac{1}{2^{3/2} \pi B m K_b E_m} \frac{\partial p_h}{\partial r} E^{-3/2} - (3/2) \frac{\omega}{2^{3/2} \pi B m K_b E_m} p_h E^{-5/2} \quad (\text{B.20})$$

Then the $\delta W_k/2\pi R$ can be rewritten as,

$$\frac{\delta W_k}{2\pi R} = -2^{3/2} \pi^2 m \frac{\xi_r^2}{R^2} \int_0^{r_s} r dr \int_0^{E_m} dE E^{5/2} \frac{K_2^2}{K_b} \frac{1}{\omega - \langle \omega_d \rangle} \left(-\frac{1}{eBr} \frac{1}{2^{3/2} \pi B m K_b E_m} \frac{\partial p_h}{\partial r} E^{-3/2} - (3/2) \frac{\omega}{2^{3/2} \pi B m K_b E_m} p_h E^{-5/2} \right) \quad (\text{B.21})$$

$$= \frac{-\pi}{B E_m} \frac{\xi_r^2}{R^2} \left(\frac{K_2}{K_b} \right)^2 \int_0^{r_s} r dr \int_0^{E_m} dE \frac{1}{\omega - c_1 E} \left(-\frac{1}{eBr} \frac{\partial p_h}{\partial r} E - \frac{3}{2} \omega p_h \right) \quad (\text{B.22})$$

$$= \frac{-\pi}{B E_m} \frac{\xi_r^2}{R^2} \left(\frac{K_2}{K_b} \right)^2 \int_0^{r_s} r dr \left(-\frac{1}{eBr} \frac{\partial p_h}{\partial r} \int_0^{E_m} \frac{E dE}{\omega - c_1 E} - \frac{3}{2} \omega p_h \int_0^{E_m} \frac{dE}{\omega - c_1 E} \right) \quad (\text{B.23})$$

$$= \frac{-\pi}{B E_m} \frac{\xi_r^2}{R^2} \left(\frac{K_2}{K_b} \right)^2 \int_0^{r_s} r dr \left(\frac{p'_h}{eBr c_1} \int_0^{E_m} \left(1 - \frac{\omega}{\omega - c_1 E} \right) dE - \frac{3}{2} \omega p_h \int_0^{E_m} \frac{dE}{\omega - c_1 E} \right) \quad (\text{B.24})$$

$$= \frac{-\pi}{B E_m} \frac{\xi_r^2}{R^2} \left(\frac{K_2}{K_b} \right)^2 \int_0^{r_s} r dr \left(\frac{p'_h}{eBr c_1} \left(E_m + \frac{\omega}{c_1} \ln \left(1 - \frac{c_1 E_m}{\omega} \right) \right) + \frac{3}{2} \frac{\omega p_h}{c_1} \ln \left(1 - \frac{c_1 E_m}{\omega} \right) \right) \quad (\text{B.25})$$

$$= \frac{-\pi}{B} \frac{\xi_r^2}{R^2} \left(\frac{K_2}{K_b} \right)^2 \frac{r_s^2}{2} \left(\frac{p'_h}{eBr c_1} \left(1 + \frac{\omega}{\omega_{dm}} \ln \left(1 - \frac{\omega_{dm}}{\omega} \right) \right) + \frac{3}{2} p_h \frac{\omega}{\omega_{dm}} \ln \left(1 - \frac{\omega_{dm}}{\omega} \right) \right) \quad (\text{B.26})$$

The toroidal precession velocity and frequency are as follows,

$$\omega_\phi = \frac{E}{eBr}, c_1 = \frac{1}{eBr} \quad (\text{B.27})$$

The kinetic integral is

$$\frac{\delta W_k}{2\pi R} = \frac{-\pi}{B} \frac{\xi_r^2}{R^2} \left(\frac{K_2}{K_b} \right)^2 \frac{r_s^2}{2} \left(p'_h R \left(1 + \frac{\omega}{\omega_{dm}} \ln \left(1 - \frac{\omega_{dm}}{\omega} \right) \right) + \frac{3}{2} p_h \frac{\omega}{\omega_{dm}} \ln \left(1 - \frac{\omega_{dm}}{\omega} \right) \right) \quad (\text{B.28})$$

$$\approx \frac{-\pi}{B} \frac{\xi_r^2}{R^2} \left(\frac{K_2}{K_b} \right)^2 \frac{r_s^2}{2} \frac{B^2}{2\mu_0} \beta'_h R \left(1 + \frac{\omega}{\omega_{dm}} \ln \left(1 - \frac{\omega_{dm}}{\omega} \right) \right) \quad (\text{B.29})$$

$$\approx \frac{B_{\theta s}^2}{2\mu_0} \xi_r^2 \frac{\pi}{2} \left(\frac{K_2}{K_b} \right)^2 \frac{-1}{B} \beta'_h R \left(1 + \frac{\omega}{\omega_{dm}} \ln \left(1 - \frac{\omega_{dm}}{\omega} \right) \right) \quad (\text{B.30})$$

Therefore dispersion relation is given as follows,

$$\frac{-i\omega}{\omega_A} + \delta\hat{W}^T + \delta\hat{W}_K = 0 \quad (\text{B.31})$$

$$-i\Omega \frac{\omega_{dm}}{\omega_A} + \delta\hat{W}^T + \pi \left(\frac{K_2}{K_b} \right)^2 (-\beta'_h) R \left(1 + \Omega \ln \left(1 - \frac{1}{\Omega} \right) \right) = 0 \quad (\text{B.32})$$

where

$$\Omega \equiv \frac{\omega}{\omega_{dm}} \quad (\text{B.33})$$

Consider the MHD instability is marginally stable, $\delta\hat{W}^T = 0$. Then we have,

$$-i\Omega\alpha_h + 1 + \Omega \ln \left(1 - \frac{1}{\Omega} \right) = 0 \quad (\text{B.34})$$

where we define,

$$\alpha_h \equiv \frac{\omega_{dm}}{\omega_A} \left(\pi \left(\frac{K_2}{K_b} \right)^2 (-\beta'_h) R \right)^{-1} \quad (\text{B.35})$$

We expand $\Omega = \Omega_r + i\Omega_i$, yielding,

$$-i(\Omega_r + i\Omega_i)\alpha_h + (\Omega_r + i\Omega_i) \ln \left(1 - \frac{1}{\Omega_r + i\Omega_i} \right) + 1 = 0 \quad (\text{B.36})$$

For instability, $\Omega_i > 0$ and considering the linear growth phase, we have $|\Omega_i| \ll |\Omega_r|$ and $1 - \frac{1}{\Omega} < 0$

$$\ln \left(1 - \frac{1}{\Omega_r + i\Omega_i} \right) = \ln \left(\frac{1}{\Omega_r} - 1 \right) + i \left(\pi + \frac{\Omega_i/\Omega_r^2}{1 - \frac{1}{\Omega_r}} \right) = \ln \left(\frac{1}{\Omega_r} - 1 \right) + i \left(\pi + \frac{\Omega_i}{\Omega_r^2 - \Omega_r} \right) \quad (\text{B.37})$$

Note that for a complex number z , the natural logarithm satisfies,

$$\ln z = \ln \left(r e^{i(\theta + 2n\pi)} \right) = \ln r + i(\theta + 2n\pi) \quad (\text{B.38})$$

Substituting the equation yields,

$$-i(\Omega_r + i\Omega_i)\alpha_h + (\Omega_r + i\Omega_i)\left(\ln\left(\frac{1}{\Omega_r} - 1\right) + i\left(\pi + \frac{\Omega_i}{\Omega_r^2 - \Omega_r}\right)\right) = 0 \quad (\text{B.39})$$

$$-i\Omega_r\alpha_h + i\Omega_r\left(\pi + \frac{\Omega_i}{\Omega_r^2 - \Omega_r}\right) + i\Omega_i\ln\left(\frac{1}{\Omega_r} - 1\right) = 0 \quad (\text{B.40})$$

$$\Omega_i\alpha_h + \Omega_r\ln\left(\frac{1}{\Omega_r} - 1\right) - \Omega_i\left(\pi + \frac{\Omega_i}{\Omega_r^2 - \Omega_r}\right) + 1 = 0 \quad (\text{B.41})$$

Thus,

$$\Omega_i = \frac{\pi - \alpha_h}{-\ln\left(\frac{1}{\Omega_r} - 1\right)}\Omega_r \quad (\text{B.42})$$

and

$$\Omega_r = \frac{1 - \Omega_i(\pi - \alpha_h)}{-\ln\left(\frac{1}{\Omega_r} - 1\right)} \quad (\text{B.43})$$

The necessary condition is $\Omega_i > 0$, therefore the following condition must be satisfied,

$$\alpha_h < \pi \quad (\text{B.44})$$

In other words, to destabilize the mode, there is a threshold for β'_h , that is,

$$-\frac{\partial\beta_h}{\partial r} > \frac{\omega_{dm}}{\omega_A} \frac{1}{R\pi^2} \frac{K_b^2}{K_2^2} \quad (\text{B.45})$$

Appendix C

Growth rate of EIC in Large Helical Device

The helical magnetic fields produced by the helical windings are given by a solutions of $\nabla^2 \Phi = 0$, which is obtained from $\vec{B}_h = \nabla \Phi$ and $\nabla \cdot \vec{B}_h = 0$. The dominant component in LHD case is helical component, having pitch number $l = 2, N = 10$. The solution is as follows for the Laplace equation is,

$$\Phi = \Phi_{l,N} I_l \left(\frac{Nr}{R_0} \right) \sin(l\theta + N\phi) \quad (\text{C.1})$$

Where I_l is the modified Bessel function. Then the helical magnetic field can be written as,

$$\mathbf{B}_h = B_r \hat{r} + B_\theta \hat{\theta} + B_\phi \hat{\phi} \quad (\text{C.2})$$

where,

$$B_r = N \Phi_{l,N} I_l' \sin(l\theta + N\phi) \quad (\text{C.3})$$

$$B_\theta = l \Phi_{l,N} I_l \cos(l\theta + N\phi) \quad (\text{C.4})$$

$$B_\phi = N \Phi_{l,N} I_l \cos(l\theta + N\phi) \quad (\text{C.5})$$

Therefore the total magnetic field strength is,

$$B \approx B_0 (1 - \varepsilon_t \cos \theta + \varepsilon_h \cos(l\theta + N\phi)) \quad (\text{C.6})$$

with

$$\varepsilon_t \equiv \frac{r}{R} \quad (\text{C.7})$$

$$\varepsilon_h \equiv \frac{N\Phi_{l,N}I_l}{B_0} \quad (\text{C.8})$$

The curvature term is

$$\kappa \approx \frac{\nabla_{\perp} B}{B} + \frac{\mathbf{J} \times \mathbf{B}}{B^2/\mu_0} \approx \frac{\nabla_{\perp} B}{B} + \mathcal{O}(\beta) \quad (\text{C.9})$$

For simplicity, we crudely treat B only in B_{ϕ} as assumption, then κ can be written as,

$$\kappa \sim (-\varepsilon'_t \cos \theta + \varepsilon'_h \cos(l\theta + N\phi)) \hat{r} + (-\varepsilon_t \sin \theta + l\varepsilon_h \sin(l\theta + N\phi)) \hat{\theta} \quad (\text{C.10})$$

$$\sim \left(-\frac{\cos \theta}{R} + \varepsilon'_h \cos(l\theta + N\phi) \right) \hat{r} + (-\varepsilon_t \sin \theta + l\varepsilon_h \sin(l\theta + N\phi)) \hat{\theta} \quad (\text{C.11})$$

Again, for trapped energetic ions, we consider $v^2 \approx v_{\perp}^2 \gg v_{\parallel}^2$. Then,

$$J \equiv -\frac{1}{2} (\xi_{\mathbf{r}} \cdot \kappa_{\mathbf{r}}) = -\frac{1}{2} \left(-\frac{\cos \theta}{R} + \varepsilon'_h \cos(l\theta + N\phi) \right) \xi_r \quad (\text{C.12})$$

The first term on the right hand side of the equation recovers the tokamak situation. Thus, we focus on the second term of the equation. For the EIC mode, we consider a very localized mode, having similar eigenfunction with resistive interchange mode, i.e., Gaussian function,

$$\xi_r = A_m \exp \left(-\frac{(r-r_s)^2}{\Delta^2} \right) \cos(m\theta - n\phi - \omega t) \quad (\text{C.13})$$

Therefore,

$$\mathbf{J} \equiv -\frac{1}{2} \varepsilon'_h A_m \exp \left(-\frac{(r-r_s)^2}{\Delta^2} \right) \frac{\cos(l\theta + N\phi + m\theta - n\phi - \omega t) + \cos(l\theta + N\phi - m\theta + n\phi + \omega t)}{2} \quad (\text{C.14})$$

and

$$J^* J = \frac{1}{4} \varepsilon_h'^2 A_m^2 \left(\exp \left(-\frac{(r-r_s)^2}{\Delta^2} \right) \right)^2 \left(\frac{\cos \Theta_1 + \cos \Theta_2}{2} \right)^2 \quad (\text{C.15})$$

Note that, if we integrate on time, the Θ_1 or Θ_2 must be null, i.e., $\Theta_1 = 0$ or $\Theta_2 = 0$. Then the equation can be simplified to,

$$\bar{J}^* \bar{J} = \frac{1}{4} \epsilon_h'^2 A_m^2 e^{-\frac{2(r-r_s)^2}{\Delta^2}} \left(\frac{1 + \cos \Theta}{2} \right)^2 \quad (\text{C.16})$$

The resonance condition can be given as,

$$l\theta + N\phi \pm (m\theta - n\phi - \omega t) = 0 \quad (\text{C.17})$$

From eq. (A.131), We have

$$\frac{\delta W_k}{2\pi R} = -2^{5/2} \pi^2 m \int r dr \int d(\lambda B_0) \int dE E^{5/2} K_b \frac{2\bar{J}^* \bar{J} Q}{\omega - \langle \omega_d \rangle} \quad (\text{C.18})$$

$$= -2^{5/2} \pi^2 m \int_0^{r_s} r dr \int_0^{E_m} dE E^{5/2} K_b \left(\frac{1}{4} \epsilon_h'^2 A_m^2 e^{-\frac{2(r-r_s)^2}{\Delta^2}} \left(\frac{1 + \cos \Theta}{2} \right)^2 \right) \frac{2Q}{\omega - \langle \omega_d \rangle} \quad (\text{C.19})$$

$$= -2^{3/2} \pi^2 m \int_0^{r_s} A_m^2 \epsilon_h'^2 e^{-\frac{2(r-r_s)^2}{\Delta^2}} r dr \int_0^{E_m} dE E^{5/2} \frac{K_2^2}{K_b^2} \frac{Q}{\omega - \langle \omega_d \rangle} \quad (\text{C.20})$$

where,

$$K_b = \oint \frac{d\Theta}{2\pi} \frac{1}{(1 - \lambda B)^{1/2}} \quad (\text{C.21})$$

$$K_2 = \oint \frac{d\Theta}{2\pi} \frac{1 + \cos \Theta}{2(1 - \lambda B)^{1/2}} \quad (\text{C.22})$$

$$\Theta \equiv l\theta + N\phi \pm (m\theta - n\phi - \omega t) \quad (\text{C.23})$$

Here, because according to LHD experiment, the instability in LHD is very localized mode, $\epsilon_h' \equiv \epsilon_h'|_{r=r_s}$, we can re-write the equation as,

$$\frac{\delta W_k}{2\pi R} = -2^{3/2} \pi^2 m \int_0^{r_s} A_m^2 \epsilon_h'^2 e^{-\frac{2(r-r_s)^2}{\Delta^2}} r dr \int_0^{E_m} dE E^{5/2} \frac{K_2^2}{K_b^2} \frac{Q}{\omega - \langle \omega_d \rangle} \quad (\text{C.24})$$

$$= -2^{3/2} \pi^2 m \frac{K_2^2}{K_b^2} H \int_0^{E_m} dE E^{5/2} \frac{Q}{\omega - \langle \omega_d \rangle} \quad (\text{C.25})$$

Here we define

$$H \equiv A_m^2 \epsilon_h'^2 \int_0^\infty e^{-\frac{2(r-r_s)^2}{\Delta^2}} r dr \quad (\text{C.26})$$

By using the previous derivation for Q , we rewrite the $\delta W_k/2\pi R$ as,

$$\frac{\delta W_k}{2\pi R} = \frac{-\pi}{B} \left(\frac{K_2}{K_b} \right)^2 H \left(\frac{p'_h}{eBrc_1} \left(1 + \frac{\omega}{\omega_{dm}} \ln \left(1 - \frac{\omega_{dm}}{\omega} \right) \right) + \frac{3}{2} p_h \frac{\omega}{\omega_{dm}} \ln \left(1 - \frac{\omega_{dm}}{\omega} \right) \right) \quad (C.27)$$

$$\approx -\frac{\pi}{2\mu_0erc_1} \left(\frac{K_2}{K_b} \right)^2 H\beta'_h \left(1 + \frac{\omega}{\omega_{dm}} \ln \left(1 - \frac{\omega_{dm}}{\omega} \right) \right) \quad (C.28)$$

$$(C.29)$$

where,

$$\langle \omega_d \rangle = c_1 E \quad (C.30)$$

The dispersion relation is given as discuss above and $\delta W_{MHD} \sim 0$,

$$-\frac{\omega^2}{2} \int \rho_m |\xi_r|^2 d\mathbf{r} + \delta W_k = 0 \quad (C.31)$$

and again, considering the interchange mode is very localized mode with $m = 1/n = 1$,

$$\int_0^\infty \rho_m |\xi_r|^2 d\mathbf{r} \quad (C.32)$$

$$= \rho_m \int_0^\infty \int_0^{2\pi} \left(A_m e^{-\frac{2(r-r_s)^2}{\Delta^2}} \cos(m\theta - n\phi - \omega t) \right)^2 2\pi R d\theta r dr \quad (C.33)$$

$$= 2\pi R \rho_m \int_0^\infty \left(A_m e^{-\frac{(r-r_s)^2}{\Delta^2}} \right)^2 r dr \int_0^{2\pi} \cos^2(m\theta - n\phi - \omega t) d\theta \quad (C.34)$$

$$= 2\pi R \rho_m \pi \left(A_m^2 \int_0^\infty e^{-\frac{2(r-r_s)^2}{\Delta^2}} r dr \right) \quad (C.35)$$

$$= 2\pi R \rho_m \pi \frac{H}{\epsilon_h'^2} \quad (C.36)$$

Substituting equations yields,

$$-\frac{\omega^2}{2} \rho_m \pi \frac{H}{\epsilon_h'^2} - \frac{\pi}{2\mu_0erc_1} \left(\frac{K_2}{K_b} \right)^2 H\beta'_h \left(1 + \frac{\omega}{\omega_{dm}} \ln \left(1 - \frac{\omega_{dm}}{\omega} \right) \right) = 0 \quad (C.37)$$

Re-written as,

$$\omega_{dm}^2 \left(\frac{\epsilon_h'^2}{\rho_m \mu_0erc_1} \left(\frac{K_2}{K_b} \right)^2 \beta'_h \right)^{-1} \left(\frac{\omega}{\omega_{dm}} \right)^2 + \frac{\omega}{\omega_{dm}} \ln \left(1 - \frac{\omega_{dm}}{\omega} \right) + 1 = 0 \quad (C.38)$$

We re-write the equation as,

$$-\alpha_h \Omega^2 + \Omega \ln \left(1 - \frac{1}{\Omega} \right) + 1 = 0 \quad (\text{C.39})$$

where

$$\alpha_h \equiv \omega_{dm}^2 \left(\frac{\varepsilon_h'^2}{\rho_m \mu_0 \text{erc}_1} \left(\frac{K_2}{K_b} \right)^2 (-\beta_h') \right)^{-1} \quad (\text{C.40})$$

and

$$0 < \Omega \equiv \frac{\omega}{\omega_{dm}} < 1 \quad (\text{C.41})$$

Similar with the previous derivation, we have,

$$-\alpha_h (\Omega_r + i\Omega_i)^2 + (\Omega_r + i\Omega_i) \left(\ln \left(\frac{1}{\Omega_r} - 1 \right) + i \left(\pi + \frac{\Omega_i}{\Omega_r^2 - \Omega_r} \right) \right) + 1 = 0 \quad (\text{C.42})$$

with $|\Omega_i| \ll |\Omega_r|$, we have,

$$-\alpha_h \Omega_r^2 + \Omega_r \ln \left(\frac{1}{\Omega_r} - 1 \right) - \Omega_i \left(\pi + \frac{\Omega_i}{\Omega_r^2 - \Omega_r} \right) + 1 = 0 \quad (\text{C.43})$$

$$-\alpha_h 2i\Omega_r \Omega_i + i\pi\Omega_r + i\Omega_i \ln \left(\frac{1}{\Omega_r} - 1 \right) = 0 \quad (\text{C.44})$$

Finally, we have,

$$\Omega_i = \frac{1}{\pi} \left(-\alpha_h \Omega_r^2 + \Omega_r \ln \left(\frac{1}{\Omega_r} - 1 \right) \right) \quad (\text{C.45})$$

and

$$\Omega_i = \frac{\pi \Omega_r}{2\alpha_h \Omega_r - \ln \left(\frac{1}{\Omega_r} - 1 \right)} \quad (\text{C.46})$$

The $\Omega_i > 0$ means the mode grows and therefore the threshold can be written as,

$$\frac{\ln \left(\frac{1}{\Omega_r} - 1 \right)}{2\Omega_r} < \alpha_h < -\frac{\ln \left(\frac{1}{\Omega_r} - 1 \right)}{\Omega_r} \quad (\text{C.47})$$

This indicates

$$0 < \frac{1}{\Omega_r} - 1 < 1 \quad (\text{C.48})$$

$$0.5\omega_{dm} < \omega < \omega_{dm} \quad (\text{C.49})$$

This indicates the threshold for the mode is,

$$-\frac{\partial \beta_h}{\partial r} > \omega_{dm}^2 \left(\frac{\varepsilon_h'^2}{\rho_m \mu_0 \text{erc}_1} \left(\frac{K_2}{K_b} \right)^2 \right)^{-1} \left(-\frac{\ln \left(\frac{1}{\Omega_r} - 1 \right)}{\Omega_r} \right)^{-1} \quad (\text{C.50})$$